COLLEGE OF ENGINEERING

VIRGINIA POLYTECHNIC INSTITUTE AND STATE UNIVERSITY

BLACKSBURG, VIRGINIA

(1)

July 1976 VPI-Aero-050

MEAN FLOW AND TURBULENCE MEASUREMENTS IN THE WAKE OF SLENDER PROPELLER-DRIVEN BODIES INCLUDING EFFECTS OF PITCH ANGLE

By

J. A. Schetz, E. B. Daffan, A. K. Jakubowski,
S. Cannon, R. Cox and D. Dubberley

Aerospace and Ocean Engineering Department

SECURITY CLASSIFICATION OF THIS PAGE (When Data Entered)

REPORT DOCUMENTATION PAGE

READ INSTRUCTIONS BEFORE COMPLETING FORM

1. REPORT NUMBER

2. GOVT ACCESSION NO.

3. RECIPIENT'S CATALOG NUMBER

4. TITLE (and Subtitle)

Mean Flow and Turbulence Measurements in the Wake of Slender Propeller-Driven Bodies Including Effects of Pitch Angle.

5. TYPE OF REPORT & PERIOD COVERED

Scientific Report.

6. PERFORMING ORG. REPORT NUMBER

VPI-Aero-050

7. AUTHOR(s)

J. A. Schetz, E. B. Daffan, A. K. Jakubowski, S. Cannon R. Cox and D. Dubberley

8. CONTRACT OR GRANT NUMBER(s)

N00014-75-C-0763 new
ARPA Order-1910

9. PERFORMING ORGANIZATION NAME AND ADDRESS

Aerospace and Ocean Engineering Department,
Virginia Polytechnic Institute and State Univ.
Blacksburg, Virginia

10. PROGRAM ELEMENT, PROJECT, TASK AREA & WORK UNIT NUMBERS

NR-062-481
ARPA Order No. 1910

11. CONTROLLING OFFICE NAME AND ADDRESS

Advanced Research Project Agency
Arlington, Virginia

12. REPORT DATE

June 1976

13. NUMBER OF PAGES

106 p.

14. MONITORING AGENCY NAME & ADDRESS (if different from Controlling Office)

Office of Naval Research
Arlington, Virginia 22217

15. SECURITY CLASS. (of this report)

Unclassified

15a. DECLASSIFICATION DOWNGRADING SCHEDULE

16. DISTRIBUTION STATEMENT (of this Report)

Approved for public release; distribution unlimited

17. DISTRIBUTION STATEMENT (of the abstract entered in Block 20, if different from Report)

18. SUPPLEMENTARY NOTES

19. KEY WORDS (Continue on reverse side if necessary and identify by block number)

Turbulent wakes
Propeller-driven bodies

20. ABSTRACT (Continue on reverse side if necessary and identify by block number)

Studies of the turbulent wake behind a slender, propeller-driven body were conducted in a low speed wind tunnel at nominal conditions of Re_D = 440,000 (4.4 = 10^5). Two models, both with the same nose and middle-body, were tested. Wake surveys at Z/D = 2, 10, and 40 were made with a single propeller model at pitch angles of 0 and -2° and with a model with dual, side-by side propellers at zero pitch angle. The variations of mean axial (cont'd.)

DD FORM 1 JAN 73 1473 EDITION OF 1 NOV 65 IS OBSOLETE

406 922

SECURITY CLASSIFICATION OF THIS PAGE (When Data Entered)

20. (Cont'd.)

velocity, velocity vector orientation, static pressure and axial turbulence intensity were documented. Force and moment data for both models at pitch angles from -6^0 to $+6^0$ were obtained. Profiles of the boundary layer on the body ahead of the propeller were also measured. The data obtained, taken as a whole, provide a detailed picture of the development of these complicated flowfields.

TABLE OF CONTENTS

NOMENCLATURE

ALPHA	geometric pitch angle of model
$b_{1/2}$	width from wake center to wake edge
C_D	drag coefficient in wind axes
C_L	lift coefficient in wind axes
C_{MB} or C_M	pitch coefficient about c.g.
C_{LB}	rolling moment coefficient
D	maximum diameter of model
E	D.C. voltage
e	RMS voltage
FP	flow pitch angle
FY	flow yaw angle
K_β	probe coefficient for flow yaw
K_α	probe coefficient for flow pitch
K_i	hole coefficient
P_B	barometric pressure
P_i	probe hole pressure
P_{st}	static pressure
$P_{st\infty}$	freestream static pressure
P_o	total pressure
q, Q	dynamic pressure
Q_E	dynamic pressure at edge of wake
R	model maximum radius
R_e	Reynolds number
Re_D	Reynolds number based on model diameter
S	cross sectional area used in coefficients = $\pi D^2/4$

U_E	axial velocity at edge of wake or boundary layer
U_z	axial velocity
$\sqrt{\overline{u'^2}}$	mean axial velocity fluctuations
V_{Total}	total velocity
$\overline{V}'$	total velocity fluctuations
X, Y, Z	coordinate directions (see Figure 17a)
X', Y'	coordinates for boundary layer surveys
ρ	density
α_e	effective model pitch angle
δ	boundary layer thickness
Θ	peripheral angle around the body from the sail

I. INTRODUCTION

Most of the past work on axisymmetric wake flows has dealt with simple shapes such as circular disks, ellipsoids, spheroids and some slender bodies. The vast majority of these studies moreover has dealt with unpropelled configurations.

The work on propelled bodies has been primarily restricted to jets injected from circular disks such as the works by Ridjanovic[1] and Haudascher[2]. Only in the last four years has the wake of propeller-driven bodies been considered. Gran[3] in 1972 and 1973 studied the wake of a propeller-driven Rankine Ovoid at Reynolds numbers based on diameter of $\simeq 6 \times 10^4$. More extensive work on propeller-driven slender bodies was published in 1974 by Swanson[4], et. al., and Chieng[5], et. al., at Re_D of $\simeq 6.18 \times 10^5$. From these studies it was found that dramatic changes occur in the wakes of non-propelled slender bodies and self-propelled bodies of the same configuration. Table I gives a survey of past wake studies on axisymmetric bodies.

In this report several previously unstudied effects on the turbulent wake of propeller-driven bodies are examined. The first is the effect of body pitch angle on the wake properties. The second is the addition of an appendage such as a "sail" to an axisymmetric body. The third is the

TABLE I

Summary of Subsonic, Axisymmetric Turbulent Wake Experiments

Author	Year	Ref. No.	Momentumless	Mean Flow	Turbulent Properties	Configuration
Hall and Hislop	1938	11		x		1 x 2 Cylinder
Cooper and Lutzky	1955	12		x	x	Thin Disks
Ilizarova and Pochkina	1962	13		x		6.67 x 1 Body of Revolution
Ridjanovic	1963	1	x	x	x	Circular Disk
Carmody	1964	14		x	x	Circular Disk
Wang	1965	15	x	x	x	Circular Disk
Naudascher	1965	2	x	x	x	Circular Disk
Ginevskii, Pochkina, and Ukhanova	1966	16	x	x	x	Circular Disk
Buchinskaya and Pochkina	1966	17		x		6 x 1 Ellip-soid
Chevray	1968	18		x	x	6 x 1 Spher-oid

TABLE I (Continued)

Summary of Subsonic, Axisymmetric Turbulent Wake Experiments

Author	Year	Ref. No.	Momentumless	Mean Flow	Turbulent Properites	Configuration
Bukreev, Kostomakha, and Lytkin	1972	19		x	x	Slender Body (8:1 Prolongation)
Hokenson and Schetz	1973	20		x	x	Sphere
Bukreev, Kostomakha, and Lytkin	1974	21		x	x	Sphere and Slender Body
Gran	1974	3	x	x	x	Rankine Ovoid
Swanson, Chieng et al	1974	4,5	x	x	x	Slender Bodies
Schetz et al	1976	Present	x	x	x	Slender Body

effect of replacing a single propeller by an equivalent set of side-by-side counter rotating propellers. Two supporting studies were also conducted. One dealt with measurements of the aero-hydrodynamic forces and movements on propeller-driven slender bodies. The second involved boundary layer measurements on the body itself.

For this work, a realistic body shape was chosen. A model fineness ratio of 12:1 was used because of its similarity to most modern submarines, and the appendage was scaled to simulate a submarine sail. To study the effect of pitch angle on the wake properties the tests were conducted at model pitch angles of 0^{o} and -2^{o}. The dual-propeller model had the same fore- and middle-body shape and the same appendage.

The primary testing was conducted in the VPI six-foot, subsonic wind tunnel at $Re_D \simeq 4.4 \times 10^5$. This wind tunnel has proven in the past to be an excellent facility for detailed flowfield and turbulence measurements because of its low free-stream turbulence level and its uniform pressure field. Measurements of total pressure, static pressure, flow angularity and axial turbulence intensity were made at discrete points across the wake at three downstream stations; 2, 10, and 40 model diameters and on the body at several stations. These measurements then yielded all velocity components and axial turbulence intensity through the wake.

The measurements were taken using a yawhead pressure probe, a pitot-static probe, a straight hot-wire sensor and a boundary layer pitot rake.

This report is arranged into several major sections. First, the apparatus, models and experimental methods are described in detail. The results are presented in separate sections, starting with the force and moment data. The next subsections in the Results section deal with the body boundary layer measurements, the single propeller model wake results and finally the double-propeller model wake results.

The results are presented mainly in graphical form, but the data for the main test program with the single propeller model is also tabulated. Comparisons with previous work on propeller-driven bodies are given whenever available.

II. EXPERIMENTAL APPARATUS AND INSTRUMENTATION

Facility

All tests were conducted in the VPI&SU 6' x 6' subsonic stability tunnel at a baseline condition of a dynamic pressure of 5.0 inches of water (approximately 157 ft./sec.) yielding a Re_D based on diameter 4.4×10^5. The facility is a continuous, closed jet, single return wind tunnel. Its test section is 28 ft. long allowing wake measurements at 40 model diameters with the model located at the far upstream end of the test section. The air stream has a low turbulence factor of 1.08. To control the tunnel velocity, a Barocel Electric Manometer is used to read dynamic pressure from a pitot-static tube mounted on the test section wall out of the wake of the model. Free-stream temperature is monitored by a temperature probe on the test section wall and recorded on a Digitemp temperature gauge. Static free-stream pressure is measured by a Validyne digital barometer Model DB99.

Models

The model considered in this investigation has an overall length of 72 inches and a maximum diameter of 6 inches, giving a fineness ratio of 12:1. The model was strut mounted from the ceiling of the wind tunnel just forward of the test section (Fig. 1). The forebody is parabolic and machined from laminated layers of plexiglas. The centerbody is an aluminum cylindrical tube with a simulated sail, and the tail bodies are also plexiglas. For the overall dimensions of the body, see Fig. 2.

Both tail bodies were ogives. The first body considered had a single shaft which extended out the stern. The second body had twin shafts which flared out at a 7^{o} angle through the stern. Both models used 2.75 h.p., DC motors to drive the propeller shafts. The single shaft model was direct drive, while the dual shaft model used a belt driven 1:1.5 step-up from the motor to the counterrotating shafts (Fig. 3a). This was necessary to achieve the higher rpm's needed for this model in the self-propelled mode.

The single shaft model used a 6" diameter, 3 bladed model airplane propeller, while the dual shaft model used two 4.375" diameter, 3 bladed propellers which were cut down versions (RH and LH) of the single propellers. All propellers were heated at the root and twisted to a higher pitch to operate more efficiently at the high air speeds used. The effective pitch of the larger propellers as modified was 2.46 (Ref. (4)). The smaller propellers were twisted to the same angle.

Force and Moment Instrumentation

The forces and moments were measured by a six component strain gage balance made by Modern Machine Tool Company internally mounted at the c. g. of the models. The arrangement is shown in Fig. 4. Note that the mounting strut is a thin (0.5 in.) blade that clears the "sail" on the model. Forces on the sail, but not on the strut, are measured along with those on the main body. Output from the balance was read on a Doric digital voltmeter. Other support equipment included a Beckman Counter Model 2D-3 which gave continuous readings from a magnetic pickup attached near the propeller shafts to determine the rpm of the propellers

for the self-propelled tests. To power the d.c. motors in both models, a Sorenson 150 volt, 15 amp power supply was used. Pressure readings to determine tunnel speed were made with a Validyne digital barometer Model DB99.

Wake Pressure Probes

The mean flow measurements were made using a three-dimensional Yawhead probe constructed by United Sensor. The probe was used in the wake region when substantial flow angularity occurred (Fig. 5). In the far wake, the flow angularity was sufficiently small to use a standard straight pitot-static tube.

The output from the pressure probes was measured on a Barocel Electronic Manometer and displayed on a Doric Digital Voltmeter. Graphical displays were provided by a HP 7100B Strip Chart Recorder and a Model 20-3 X-Y Recorder. To read all five pressure ports from the yawhead probe on the electronic manometer, a Scanivalve Model W0601/IP-RT fluid switch wafer with solenoid drive was used.

Hot Wire Instrumentation

The axial turbulence data was obtained using a straight hot wire (TSI Model 1210). This sensor uses a platinum plated tungsten wire .00015 inches in diameter. The probe was operated at an overheat ratio of 1.8 using a constant temperature anemometer module (TSI Model 1050) and a Power Supply and Monitor (TSI Model 1051-6). Readings were taken from a DISA 55D35 RMS Meter.

Traverse Mount

Both pressure and hot wire probes were moved through the wake using the traverse shown in Fig. 6. This mount had a vertical movement of 4 ft. and a horizontal range of 11.0 in. It was therefore necessary in the far wake studies to move the mount to obtain a wider horizontal range. Both vertical and horizontal movement was accomplished with variable speed motors which were controlled outside the test section. The probe position was monitored using a series of potentiometers.

Boundary Layer Rake

The body boundary layer measurements were made with a rake of pitot tubes as shown in Fig. 7. Closer spacing of the tubes nearest the wall was employed to produce better resolution of the turbulent boundary layer profiles anticipated.

Since the rake was built to allow mounting by straps around the body at virtually any axial station and at variable peripheral locations, a pitot-static probe was attached to the outside of the rake. This was to permit static pressure determination wherever the rake was located. This caused concern as to possible interference effects. Previous work in this area by Krause, Ref. (22), indicates that the change in static pressure reading obtained from a pitot-static tube due to an adjacently positioned tube, can be held to a minimum if the spacing is approximately 5 diameters. In cases where large gradients necessitate placing total-pressure tubes closer than 5 diameters to static-pressure tubes, the proximity effects can be minimized by proper orientation of the leading edge of adjacent tubes in relation to the static orifices. A logical extension of these

results was felt to be that adjacent total-pressure tubes, sans static ports, should also be aligned at their leading edge. Still, the proximity effects do increase with closer spacing and thus a minimum tube spacing of 2.5 diameters was specified for the purposes of this investigation.

The literature indicates, also, that the ratio of the distance between the pitot-static tube leading edge and the static ports to the distance between those ports and the support structure is critical[23]. Depending upon whether the design is "standard" or according to Prandtl, the recommended ratio is either 1:2 or 1:3. In the standard design the tube is bent 90^{o} in a curved fashion, 16 diameters behind the static ports, whereas in the Prandtl design this bend is squared off 8-10 diameters behind the ports.

Due to the nature of the rake design, a support strut extended from the base up past the highest total-pressure tube. By affixing a 1/16th inch diameter pitot-static tube to the top of this, a Prandtl configuration was, in effect, achieved with the strut serving the function of a squared off tube bend. Therefore, the pitot-static tube was positioned such that its static orifices lay 10 diameters forward of the strut. Unfortunately, we were then faced with the fact that the tip ends of the underlying total-pressure tubes were not in line with the pitot-static tubes static orifices, as per Krauses' recommendation (Ref. (22)) and thus a test of this new configuration was performed in the VPI open-throat, return-type wind tunnel with a three foot diameter test section.

A four-foot length of 2-1/4 inches diameter plastic pipe was rigidly suspended by wire in the test section and fitted with a smooth nose-cone.

The rake was attached to this at various downstream positions and connected to all the same electronic equipment as was used during test runs on the submarine model in the VPI Stability wind tunnel. The model was tested at several velocities up to 3.5 inches of water, and static pressure data were taken at selected points on the model with the rake. At these same points, static pressure data were obtained using a solitary pitot-static tube suspended to the same spatial location as the rake, pitot-static tube previously was. From these data, plots of error in static reading as a function of both velocity, boundary layer height, and X^1/D, the nondimensionalized variable denoting distance back from the leading edge, were made. It can be seen in Figure 8 that the data for 2.5 and 3.0 inches of water overlay each other quite well and indicate that the error ranges from near 5%, when the boundary layer is very small, to about 2%. The assumption was made that the curve, δ versus % error, did not vary with velocity. This correction was applied to the submarine model measurements.

III. EXPERIMENTAL METHODS

Force and Moment Tests and Self-Propelled Status

With the model mounted in the tunnel, potentiometers were used to zero the output from the balance due to the weight of the model.

The free-stream velocity was increased to 5.0 inches of water while the axial force was monitored. The propeller rpm was then increased until the axial force reading was zero. This was done for several angles of attack between -6° and +6°. At each angle the propeller RPM needed to zero the axial force was recorded.

To expedite data reduction, the calibration curves for the six component balance were programmed in a data reduction routine for use on the VPI IBM/370 computer. The program converted the strain gage output in millivolts into body forces and moments in standard English units. These forces were then non-dimensionalized into the standard body force and moment coefficients using the free-stream static pressure and temperature. The program also performs the axes transformation to obtain C_L and C_D in the wind axes. The results were then machine plotted using an interactive data reduction and plotting routine.

Mean Flow in the Wake

The mean flow velocities as well as flow angularity were determined using a five-port yawhead probe in regions of large flow angle. In the far wake, a conventional pitot-static tube was used and data reduction was by standard methods. The yawhead probe was calibrated over a range of flow pitch and flow yaw angles between -30° and +30°.

It was decided that an adequate description of the wake could be achieved with three transverse cuts. These cuts are seen in Fig. 9. These

three traverses were made at downstream stations of Z/D = 2, 10, and 40 with the model at $\alpha_e = 0°$ and $\alpha_e = -2°$ for the single propeller model and at only $\alpha_e = 0$ for the dual propeller model. Measurements were taken at 0.5 inch intervals across the wake.

To obtain the mean velocity components from the pressure measurements the following relation for total pressure was used:

$$P_o = P_s + \frac{1}{2}\rho V^2 + \frac{1}{2}\rho \overline{V}'^2$$

where V is the mean total velocity and $\overline{V}'$ is the sum of the mean fluctuations. Since $V^2 >> \overline{V}'^2$, the $\frac{1}{2}\rho\overline{V}'^2$ was neglected. The yaw-head probe gave direct readings of $P_1 - P_{st\infty}$, where P_1 is the mean total pressure and $P_{st\infty}$ is the free stream static pressure.

Therefore since

$$P_1 = P_{st} + \frac{1}{2}\rho V^2$$

the mean total velocity can be calculated from

$$V_{total} = \sqrt{\frac{2[(P_1 - P_{st\infty}) - (P_{st} - P_{st\infty})]}{\rho}}$$

then the mean axial velocity can be obtained by

$$U_z = V\cos(FP)\cos(FY)$$

where FP is the flow pitch angle and FY is the flow yaw angle. Similarly the other velocity components are given by

$$U_x = V\cos(FP)\sin(FY)$$

$$U_y = V\sin(FP)$$

To obtain the local static pressure from the yawhead probe a method described by Winternitz (Ref. 6) was used. Since this method is only good for substantial flow angularity in one direction, calibration curves were obtained for both flow pitch and yaw. The flow yaw angle FY is found from the calibration probe constant

$$K_\beta = \frac{P_3 - P_2}{P_1 - P_4}$$

for each station. Defining the hole constant as

$$K_i(\beta) = \frac{P_i - P_{st}}{q}$$

where P_i is the hole pressure and q is the dynamic pressure. Winternitz showed that

$$q = \frac{(P_1 - P_{st\infty}) - (P_2 - P_{st\infty})}{K_1 - K_2}$$

or

$$(P_{st} - P_{st\infty}) = (P_2 - P_{st\infty}) - qK_2.$$

Therefore

$$(P_{st} - P_{st\infty}) = \frac{K_1(P_2 - P_{st\infty}) - K_2(P_1 - P_{st\infty})}{K_1 - K_2}$$

Similarly for the pitched case where the yaw angles are small

$$K_\alpha = \frac{P_4 - P_5}{P_1 - P_2}$$

and,

$$(P_{st} - P_{st\infty}) = \frac{K_1(P_5 - P_{st\infty}) - K_5(P_1 - P_{st\infty})}{K_1 - K_5} \quad .$$

From these relations the local static pressure could be determined when there was substantial pitch angles with small yaw angles or for large yaw angles with small variations in pitch.

Turbulence Measurements

The axial turbulence intensity was measured at the same points as the mean flow measurements using a straight hot-wire. The constant

temperature method was used as discussed in Ref. 8. The hot wires were calibrated by measuring their total voltage at different dynamic pressures between 0 and 8.0 inches of water. This calibration was done at three free-stream temperatures, 72^{o}, 84^{o}, and 92^{o} F to see how the calibrations were affected by temperature. By measuring the total voltage E and the RMS voltage $\overline{e}'^{2}$ the axial turbulence could be obtained from the relation

$$\frac{\overline{u}'^{2}}{U} = \frac{2E\ \overline{e}'^{2}}{n(E^{2} - E_{o}^{2})}^{*}$$

where n = .45 for Re < 44 based on the diameter of the hot wire, and E_o is the total voltage reading of zero velocity. Also by using the calibration curves the mean axial velocity could be found and compared with the mean velocity obtained from the pressure probe.

Boundary Layer Measurements

Measurements were made at X'/D = 1, 6, 8, 10 an d 11.17* and at peripheral locations in the line with the sail (θ = 0), opposite the sail ($\theta = 180^{o}$) and halfway around the body ($\theta = 90^{o}$). The data were reduced using the Bernoulli equation, the local pitot pressure and the static pressure determined using the pitot-static probe at the top of the rake.

* X'/D for the body boundary layer measurements are measured from the body nose. Wake measurements use X/D measured from the stern.

IV. RESULTS

Force and Moment Data

These tests were conducted with the models in two locations in the tunnel test section. Tests were run with the models in the very front of the test section to determine the self-propelled conditions for the wake tests. Tests were also run with the models in the middle of the test section, where the flow is more uniform, in order to develop basic force and moment data for this body shape. The latter data are presented in this section.

The single shaft model without a propeller was strut mounted from the ceiling of the tunnel at zero geometric pitch angle. To align the model with the free-stream velocity vector, a run was made, the tunnel was stopped, adjustments were made, and tests were rerun until no side force was measured. After proper alignment was achieved, the six force and moment readings were recorded from the voltmeter. Next, the angle of the pitch was changed, and the six readings were recorded again. This procedure was repeated until measurements had been taken for pitch angles between -6^{o} and 6^{o}.

The next step was to attach the propeller and repeat the measurements for the self-propelled case. To do this, the wind tunnel was run at test speed while the axial force reading was monitored. Then, by slowly increasing the voltage to the DC motor in the model, the rpm of the propeller was increased until the axial force reading was zero. Once the axial force reading was zeroed, the other five readings were taken, and this procedure was repeated for all pitch angles.

To study the effect of twin propellers on the force and moments, the single shaft stern section was replaced by the twin shaft tail section. The tunnel was again run at q = 5.0 in. H_2O (157 ft./sec.), and the side force was monitored with no props to check for proper alignment. Once proper alignment was established, the force and moment readings were recorded for the same range of pitch angles. The props were then attached to the shafts and the same procedure was followed as before for the self-propelled configuration.

All forces and moments were put in coefficient form and plotted versus the angle of pitch. For each model, the self-propelled and non-propelled cases were plotted together for comparison. There were no significant side forces or yawing moments measured with proper alignment of the models. The results are presented in Fig. 10-16.

Consider first the results for the single propeller model. In Fig. 10, the drag coefficient is shown versus pitch angle for both the unpropelled (no propeller) and self-propelled cases. A true self-propelled condition was achieved by simply zeroing the axial force during the test for $-4^o < \alpha < 4^o$. This procedure produced small errors $\left(C_D \approx \frac{(C_D)\text{unpropelled}}{10}\right)$ for larger pitch angles. The drag of the unpropelled body increased rather sharply for positive pitch angles.

The lift coefficient data are given in Fig. 11 where it can be seen that the addition of running propellers increases the lift curve slope. The change is more pronounced at positive pitch angles. The increase in lift curve slope is due to at least two effects. The first is the component of thrust normal to the wind vector which gives an increase in C_L

proportional to the sine of the pitch angle. The second effect is a normal body force on the propeller when the body is pitched produced by turning of the fluid passing through it.

Pitching moment results are presented in Fig. 12. A small decrease in the slope of the curve is produced by the propeller. Since the thrust is always along the body axis, only the effects of fluid turning by the propeller when the body is pitched are felt here.

Figs. 13, 14, and 15 contain the results obtained for the dual propeller model. The drag coefficient results in Fig. 13 are qualitatively similar to those for the single propeller case. The no-propeller drag is somewhat higher,presumably due to the presence of the exposed shafts.

The effect of propulsion on the variation of the lift coefficient with pitch angle (Fig. 14) is perhaps less but similar in character to that on the single propeller model. On the other hand, the spread for the propelled and unpropelled arrangements for pitching moment in this case is larger than that for the single-propeller model.

Lastly, we show rolling moment results for both models in Fig. 16 in the self-propelled mode. The unbalanced torque of the single propeller model can be clearly seen, while the counter-rotating, dual propellers show the expected zero net torque.

Single Propeller Model Wake Surveys

Since the sail of the model as well as the effect of pitch angle was to induce asymmetrics in the wake, it was necessary to probe the entire wake structure. For this reason all of the profiles presented extend from one edge of the wake to the other or, in the case of the

vertical traverse, from the edge of the wake into the wake region of the sail. The mean axial velocity, static pressure, flow angularity and axial turbulence intensity are plotted for both $\alpha_e = 0^o$ and -2^o at stations Z/D = 2, 10, and 40. The coordinate systems and sign conventions used are shown in Fig. 17.

First,consider the results for the model at $\alpha_e = 0^o$. In the near wake (Z/D = 2) there is a momentum defect at the center of the wake and then a momentum excess region in the outer portion of the wake (Figs. 18 and 19). The static pressure decreases in the wake of the propeller as in the case of a swirling vortex. The propeller swirl is indicated by examining the flow angularity. For the horizontal profiles (Fig. 18), large variations in flow pitch are measured with very small changes in the flow yaw, but in the vertical profiles (Fig. 19) the substantial flow angularity is in the yaw direction.

At Z/D = 10 the momentum excess and defect regions have decreased and spread out. The static pressure variation has also decreased and the swirl has decreased to the point that the flow angularity is only half the value measured at Z/D = 2 (Fig. 20).

By Z/D = 40 there is only a small momentum excess in the wake and its character is very similar to the far wake of a zero-momentum jet (Refs. 1 and 2). The static pressure is uniform across the wake and the swirl has completely diminished as seen by the small flow angularity (Figs. 21 and 22).

The axial turbulence intensity is characterized by a highly fluctuating nature in the near-wake (Z/D = 2). At this station,the

velocity fluctuations are up to 10% of the free-stream velocity in the center of the wake (Fig. 23). At Z/D = 10 the turbulence intensity has decreased to about 6% of the free-stream velocity and does not vary significantly across the wake (Fig. 24). The maximum value has fallen to about 2% by X/D = 40 (Fig. 25).

The effect of the sail on the mean flow and turbulence quantities is seen in the vertical profiles at each station. The sail produces a larger momentum deficit in the upper portion of the vertical profile which indicates the increased drag on the body due to the sail (Figs. 26 and 27). The flow angularity is also reduced in the region behind the sail. This reduction is as much as 6.5^{o} at Z/D = 2, (Fig. 19), and 3^{o} at Z/D = 10. Also the static pressure is increased substantially by the presence of the sail. This increase is up to 50% in the upper portion of the vertical profile as compared to the lower portion (Fig. 19). The effect on axial turbulence intensity was to increase the level of turbulence in the vertical profile behind the sail (Figs. 28 and 29).

The mean-flow results for the pitched condition (Figs. 30-33) show increased asymmetrics in the vertical profiles. The flow angularity is decreased in the upper region of the vertical profile by 9^{o} at the Z/D = 2 station (Fig. 31) and by 6^{o} at the Z/D = 10 station (Fig. 33). The static pressure is again higher above the wake center for the pitched configuration. The maximum turbulence intensity is increased by 15% at the Z/D = 2 station (Fig. 28) and by 5% at the Z/D = 10 station (Figs. 34 and 35). At 40 diameters, the turbulence intensity and mean flow profiles are about the same for both the pitched and unpitched configurations (Fig. 36 and 37). The comparison of maximum turbulence intensity with our previous

work shows an increased turbulence level due to the higher propeller rpm needed to balance the extra drag of the sail (Fig. 38) compared to the work in Refs. (4) and (5).

From the results presented, several conclusions about the effects of appendages and non-zero pitch angles on the wake structure of a propeller driven body can be asserted.

First, an appendage such as a submarine sail reduces the propeller swirl in the region subjected to the wake of the sail. This decrease in swirl causes an increase in static pressure as would be seen in a vortex of decreasing strength. The axial turbulence intensity is increased by the value of the sail induced turbulence at each station. This suggests that the turbulence in the wake of an appendage might be superimposed on the turbulence profile of the main body.

Second, the pitched condition further reduces the swirl and increases the static pressure in the region behind the sail. These effects are primarily confined to the vertical plane and little change in the horizontal profiles is seen. The maximum turbulence intensity in the wake up to Z/D = 10 is increased for the pitch condition. However, by 40 diameters the turbulence levels are equivalent for both the pitched and unpitched conditions.

Third, the effect of the sail on the drag coefficient is to increase it from $C_D = 0.09^*$ as calculated for the body without sail by Swanson, et al (Ref. (4)) to $C_D = 0.30^*$ with the sail. This large increase in C_D indicates the need for streamlining of such appendages on slender axisymmetric bodies.

* Both these values correspond to the model in the far upstream part of the test section where some effects of the contraction section persist.

Dual Propeller Model Wake Surveys

It should be said clearly at the outset that this test series was continuously plagued by mechanical problems directly traceable to the 7° total-angle flare between the two counter-rotating shafts (see Fig. 3). The flexible, constant rotational speed couplings were subject to unpredictable failure with a service life of anywhere between roughly fifteen minutes and two hours. We have made repeated inquiries to all possible suppliers and have been assured that the items we are using are the best available for the job. A coupling failure was also, unfortunately, often accompanied by damage to one or both of the propellers.

A second problem encountered in performing these tests was the amazing sensitivity of the near-wake profiles to small variations in the propellers and/or the model. Even with great care exercised in making the model and sets of RH/LH propellers as symmetrical as possible, considerable side-to-side asymmetries were often encountered. It became necessary to run systematic near-wake profiles using various combinations of propellers until reasonable symmetry was achieved. This symmetry problem was actually so severe that it has prompted us to wonder what the state of affairs is behind real submarines with side-by-side propellers. The symmetry problem also interacted in an unfavorable way with the coupling failure problem mentioned in the first paragraph. As we proceeded through the test program, sets of propellers were destroyed and had to be replaced. The new sets were not precise matches in terms of near-wake profiles to the originals. Thus, the test results to be presented below were made with three different sets of propellers that were matched in terms of gross parameters such as thrust but not in small scale detail.

Mean flow results are shown in Figs. 39 - 43. The horizontal cut through the near-wake (Z/D = 2) shown in Fig. 39 shows the type of symmetry that we judged as acceptable. Only with prior viewing of some of the unsymmetrical profiles that we obtained with propeller sets that looked acceptable to the naked eye can one objectively judge the results in Fig. 39. Notice that, as before, the propellers act mainly to produce flow angle in only one direction.

A vertical cut down behind the sail and over the tip of the stern is shown in Fig. 40. Here, the interaction between the tips of the two propellers produces a complicated flow angle pattern.

A vertical cut down over one of the two propeller hubs is shown in Fig. 41. Reasonable vertical symmetry of profile is achieved here.

The mean flow results for Z/D = 10 and 40 were obtained with a Pitot-Static probe, so that much more detailed coverage of the flow in a transverse plane was possible. Those results are shown in Figures 42 and 43 as profiles of $U-U_e$ overlaid with a silhouette of the model in the background. These plots permit a comprehensive picture of the development of the total flow field. By Z/D = 10, the maximum velocity variation has fallen to approximately 13% of the freestream speed from its value of approximately 25% at Z/D = 2. By Z/D = 40, the maximum is further reduced to 6%. The corresponding values for the single propeller model at $\alpha_e = 0$ were 28% at Z/D = 2, 12% at Z/D = 10, and 7% at Z/D = 40 indicating about the same level and rate of decrease for the two models.

Our difficulties with propeller failures and symmetry with this dual propeller model forced only a limited effort with the hot-wire for this case. A horizontal and an abbreviated vertical traverse for axial turbulence intensity was obtained at Z/D = 2. The results are shown in Fig. 44.

The observed maximum value of 12% is somewhat higher than the maximum for the single propeller model with $\alpha_e = 0.$ at the same station. The highest value was observed where the tips of the two side-by-side propeller circles overlap. Another peak is observed at the outer edge of the propeller circle (X/R = 1.375).

Body Boundary Layer Measurements

The primary purpose of this task was to aid in interpreting the near-wake surveys. Thus, these data were taken with the body mounted in its forward location where the flow is still adjusting slightly from the tunnel contraction section. The data should then be viewed as corresponding to the uniform flow over a body which is slightly distorted from that actually tested. Nonetheless, several interesting semi-quantitative and qualitative observations regarding the boundary layer development as a subject in itself can be made on the basis of the data obtained.

Before a discussion of the data, a description of the reference coordinate system is necessary for better identification of the subsequent graphs. The origin is located at the nose of the submarine model with the X'-axis as the axis of symmetry of the submarine (minus the sail). The two coordinates X'/D and θ, locate the rake with respect to the submarine. The peripheral angle, θ, is measured from a value of zero in the vertical plane through the sail and the body axis. Clockwise looking upstream is positive. The vertical coordinate, Y'/D, is measured from the local body surface.

Figures 45 through 47 are non-dimensionalized velocity profiles at specified X'/D locations, with three values of θ at each. Figures 45 and 46 for X'/D values of 6 and 8, respectively, show the effect of the sail (θ = 0°) as evidenced by the velocity profile characteristics at 0, 90, and 180 degrees. Also, note how closely the velocity profiles for 90 and 180 degrees agree, which both indicates that the flow disturbed by the sail is very localized in a narrow wake behind the sail and substantiates the assumption that the submarine model is oriented parallel to the flow. Figure 47 for X'/D equal to 10 shows similar results except that the profile on the

side of the body has started to depart more from that on the bottom opposite the sail.

The rake was modified to reduce its dimension in the streamwise direction to a minimum in order to make observations as close to the propeller as possible. This resulted in runs at X'/D = 11.17 which is only about 2 inches ahead of the 6 inch diameter propeller. Some results are shown in Figure 48 where the top to bottom asymmetry produced by the wake of the sail is still clearly evident.

Figures 49 and 50 show the overall effects of the sail on the boundary layer. Figure 49 contains all the plots for θ equal to 0 degrees which, except for the profile at X'/D equal to 1, illustrate the effects of the sail.

It was felt that the flow far downstream of the sail might separate were it not for possible flow entrainment induced by the propeller. Any analysis which does not include this influence on the flow is thus incomplete. Figures 51 and 52 are velocity profiles at X'/D equal to 10 and 11.17, respectively, with and without the propeller. The velocity is left dimensional in order to display any velocity increase from flow entrainment, if it exists. At X'/D = 10 the flow is identical in both cases with and without the propeller, indicating no flow change due to entrainment, but it is apparent that the propeller is starting to affect the flow at 11.17 diameters. The effect is more pronounced nearest the body where the velocity difference is about 5 ft./sec., an increase of 9.0%, whereas in the freestream the increase is about 2 ft./sec., a 1.7% increase in velocity.

V. DISCUSSION

A comprehensive, experimental program of study considering the flow-field around and behind a slender, stern-propeller-driven body in a wind tunnel at nominal $Re_D = 4.4 \times 10^5$ has been conducted. The work was divided into four tasks. The first task dealt with the influence of pitch angle variations and a sail-like appendage on the wake behind a single propeller model. The second task dealt with the wake behind a dual (side-by-side) propeller model at zero pitch angle. The third task concerned measurements of the boundary layer over the body itself and the influence of a propeller on the body layer near the stern. The fourth task involved measurements of force and moment coefficients for both models over a range of pitch angle from -6^o to $+6^o$. The major results and conclusions for each task were described in each separate section.

The results suggest some useful areas for further study. First, the influence of variations in propeller parameters such as the number of blades and solidity should be determined. It will also be interesting to study the effects of roughness for boundary layer tripping on the blades. Second, since the sail clearly has a large influence on the flow, a parametric investigation of the effects of this and other appendages should be worthwhile. Third, further studies of the body boundary layer especially nearer to the propeller are sure to be enlightening. Last, the whole matter of making good turbulence measurements (including shear) in the high gradient region behind a propeller must be thoroughly considered.

REFERENCES

1. Ridjanovic, M., "Wake With Zero Change of Momentum Flux," Ph. D. Dissertation, 1963, University of Iowa, Iowa City, Iowa.

2. Naudascher, E., "Flow in the Wake of a Self-Propelled Body and Related Sources of Turbulence," Journal of Fluid Mechanics, Vol. 22, 1965, pp. 625-656.

3. Gran, R. L., "An Experiment on the Wake of a Slender Propeller-Driven Body," TRW Report 20086-6006-RU-80.

4. Swanson, R. C., Jr., Schetz, J. A., Jakubowksi, A. K., "Turbulent Wake Behind Slender Bodies Including Self-Propelled Configurations," VPI-AERO-024, 1974. (Available thru D.D.C.)

5. Chieng, C. C., Jakubowski, A. K., Schetz, J. A., "Investigation of the Turbulent Properties of the Wake Behind Self-Propelled Axisymmetric Bodies," VPI-AERO-025, 1974. (Available thru D.D.C.)

6. Winternitz, F. A. L., "Probe Measurements in Three-Dimensional Flow," Aircraft Engineering, August 1956, p. 273.

7. Mason, W. H. and Marchman, J. E., III, "Fairfield Structure of an Aircraft Trailing Vortex, Including Effects of Mass Injection," NASA CR-62078, 1972.

8. Hinze, J. O., Turbulence -- An Introduction to Its Mechanism and Theory, McGraw-Hill, New York, 1959.

9. Birkhoff, G. and Zarantonello, E. H., Jets, Wakes, and Cavities, Academic Press, New York, 1957.

10. Houghton, E. L. and Brock, A. E., Aerodynamics for Engineering Students, St. Martin's Press, New York, 1970.

11. Hall, A. A. and Hislop, G. S., "Velocity and Temperature Distributions in the Wake Behind a Heated Body of Revolution," Proc. Comb. Phil. Soc. 34, 1938.

12. Cooper, R. D. and Lutzky, M., "Exploratory Investigation of the Turbulent Wakes Behind Bluff Bodies," DTMB R4D Rept. No. 953, October 1955.

13. Ilizorova, L. I. and Pochkina, K. A., "Experimental Study of a Wake Behind a Body of Revolution," Prom. Aerodynamika, No. 23, 1962.

14. Carmody, Thomas, "Establishment of the Wake Behind a Disk," Journal of Basic Engineering-Transactions of the ASME, December 1964.

15. Wang, H., "Flow Behind a Point Source of Turbulence," Ph. D. Dissertation, 1963, University of Iowa, Iowa City, Iowa.

16. Ginevskii, A. S., Pochkina, K. A., and Ukhanova, L. N., "Propagation of Turbulent Jet Flow with Zero Excess Momentum," Fluid Dynamics Academy of Sciences USSR, Vol. 1, No. 6, November-December 1966, Faraday Press, Inc.

17. Buckinskaya, E. K. and Pochkina, K. A., "Investigation of Vortex Wake Behind a Body of Revolution," Prom. Aerodynamika No. 23, 1962.

18. Chevray, R., "The Turbulent Wake of a Body of Revolution," Journal of Basic Engineering-Transactions of the ASME, Series D, 1968.

19. Bukreev, V. I., Kostomakka, V. A., and Lytkin, Yu, "Axisymmetric Turbulent Wake Behind a Streamlined Body," Siberskae, Otdeline An SSSR, Institut Gidrodinamiki, Dinamika Splashhoi Sredy, No. 10, 1972.

20. Hokenson, G. J. and Schetz, J. A., "Free Turbulent Mixing in Axial Pressure Gradients," Journal of Applied Mechanics, June 1973.

21. Bukreev, V. I., Kostomakha, V. A., and Lytkin, Yu, M., "Turbulent Energy Balance in Axisymmetric Wakes Behind Differently Shaped Bodies," Prikladnaya Mikhanika i Teknicheskaya Fizeka, No. 1, 1974.

22. Krause, Lloyd, N.: "Effects of Pressure-Rake Design Parameters on Static-Pressure Measurement for Rakes Used in Subsonic Free Jets," NACA Technical Note 2520, 1951.

23. Holman, J. D.: Heat Transfer, McGraw-Hill, New York, 1972, p. 132.

24. Pope, Alan; Harper, John J.: Low-Speed Wind Tunnel Testing, Wiley and Sons, New York, 1966, pp. 91-94.

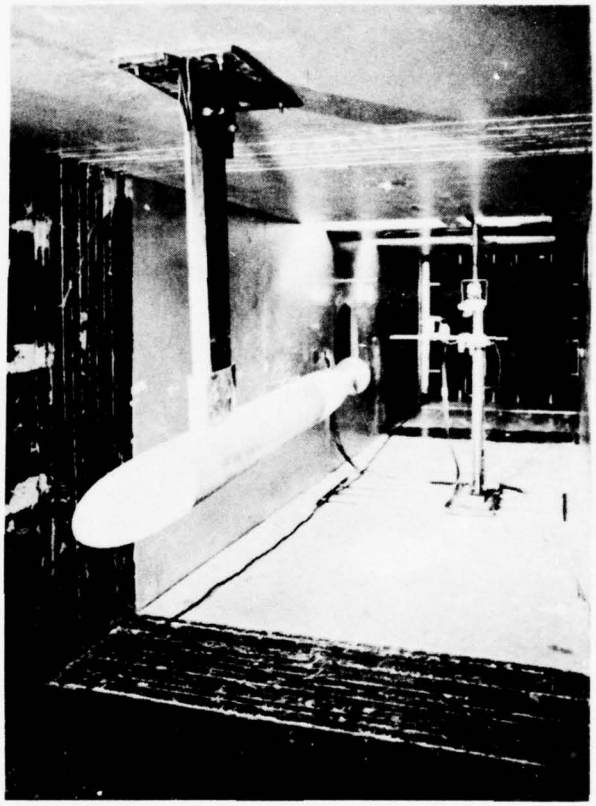

Fig. 1 PICTURE OF MODEL AND TRAVERSE

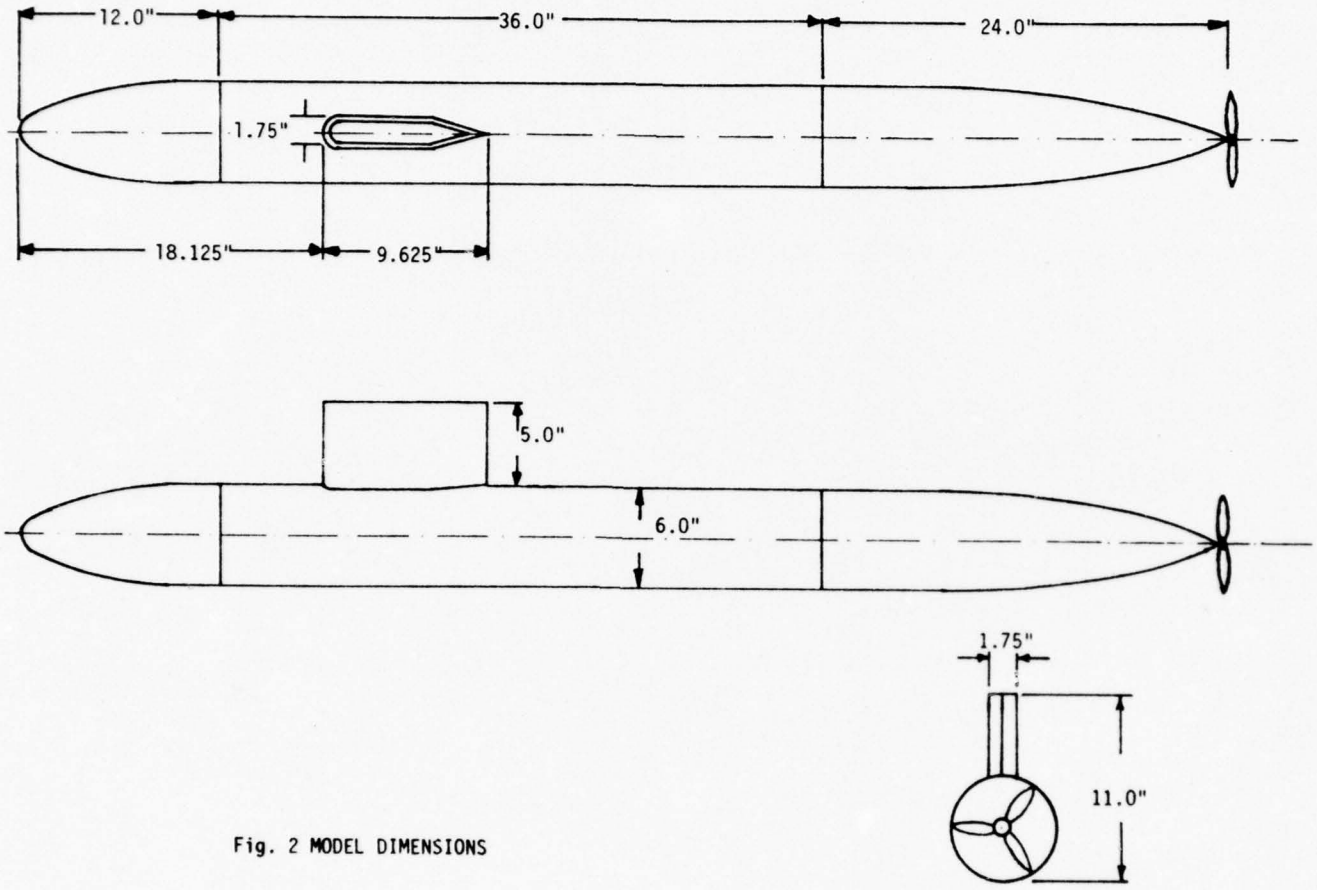

Fig. 2 MODEL DIMENSIONS

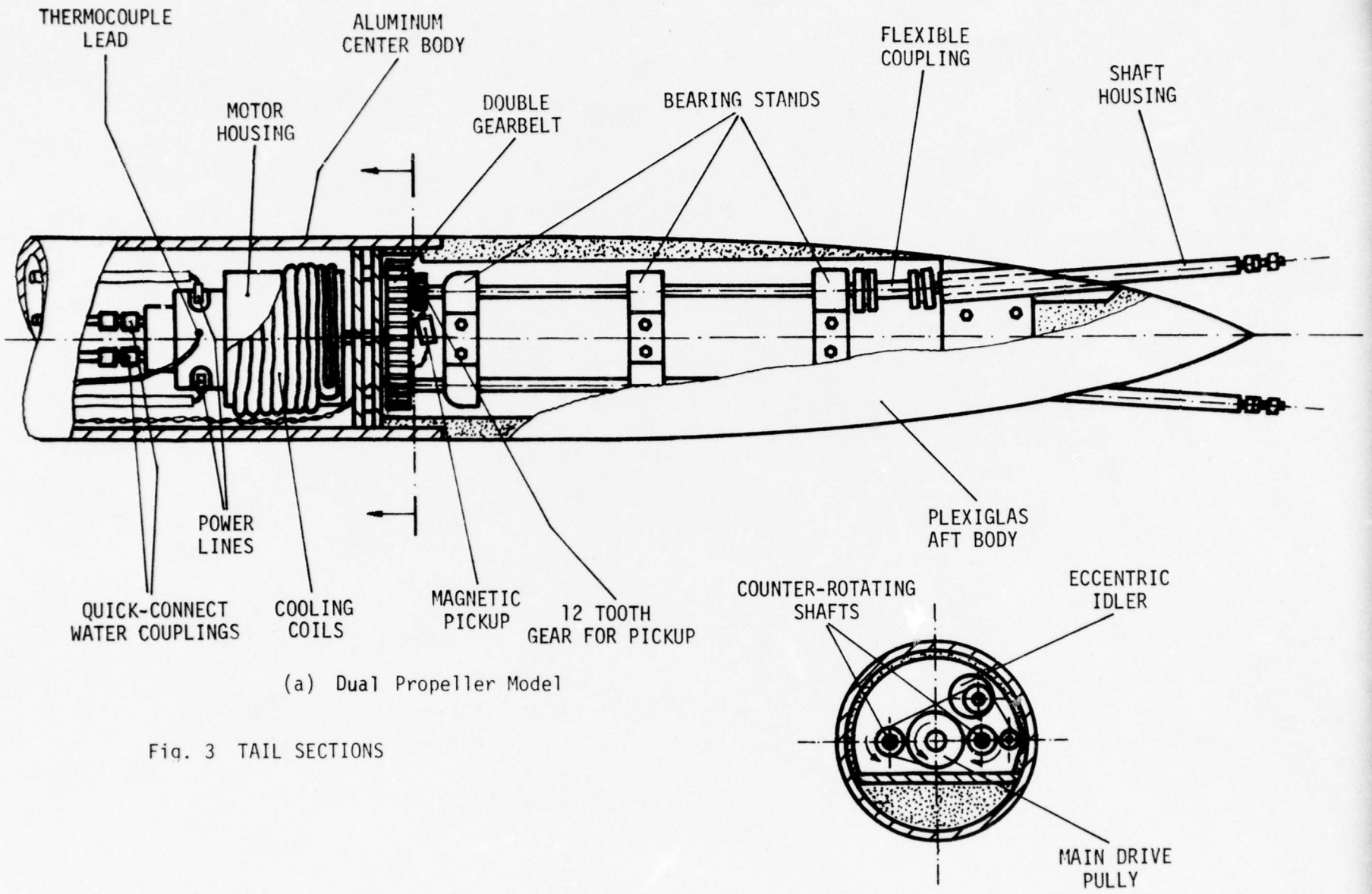

(a) Dual Propeller Model

Fig. 3 TAIL SECTIONS

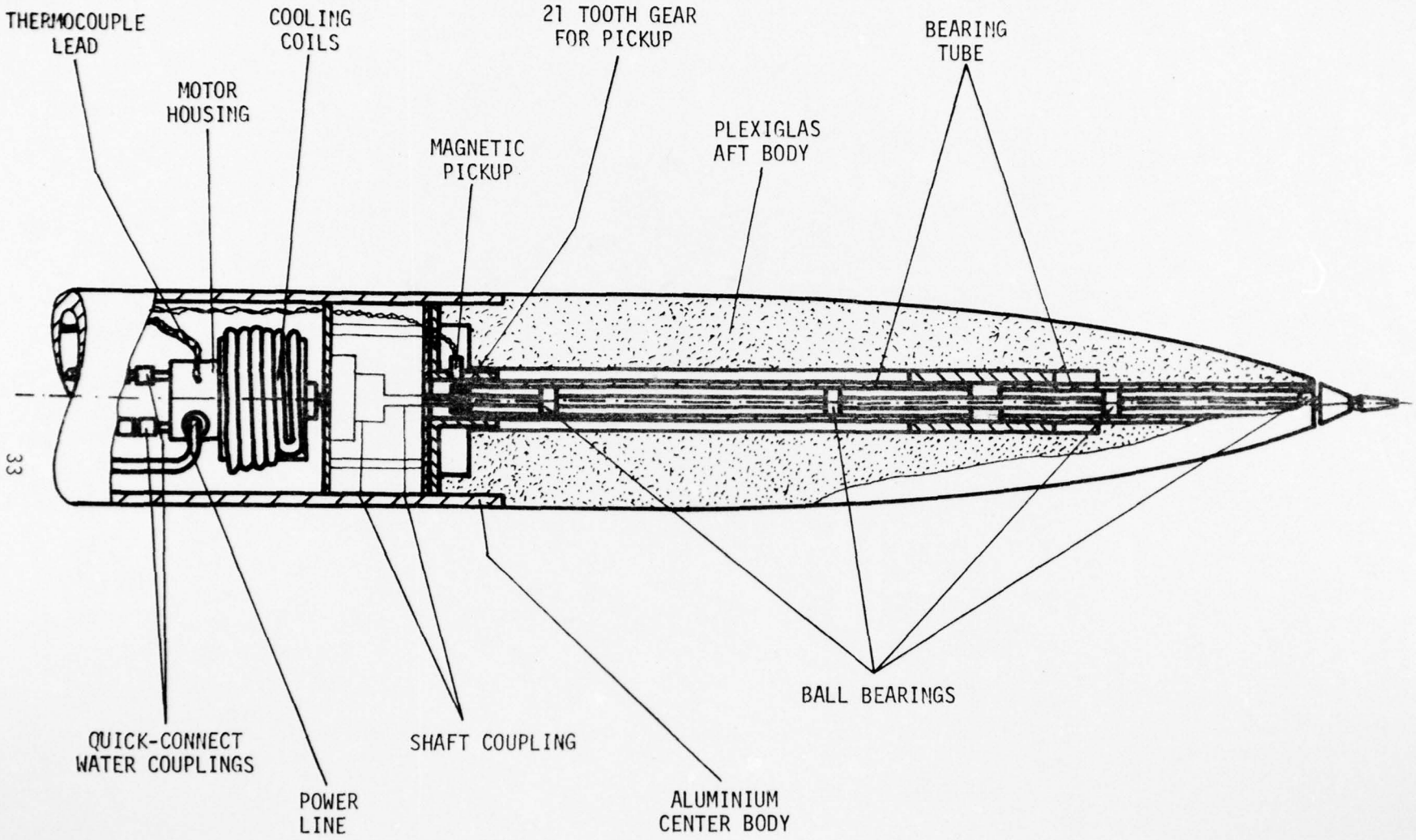

Fig. 3(b) SINGLE PROPELLER MODEL

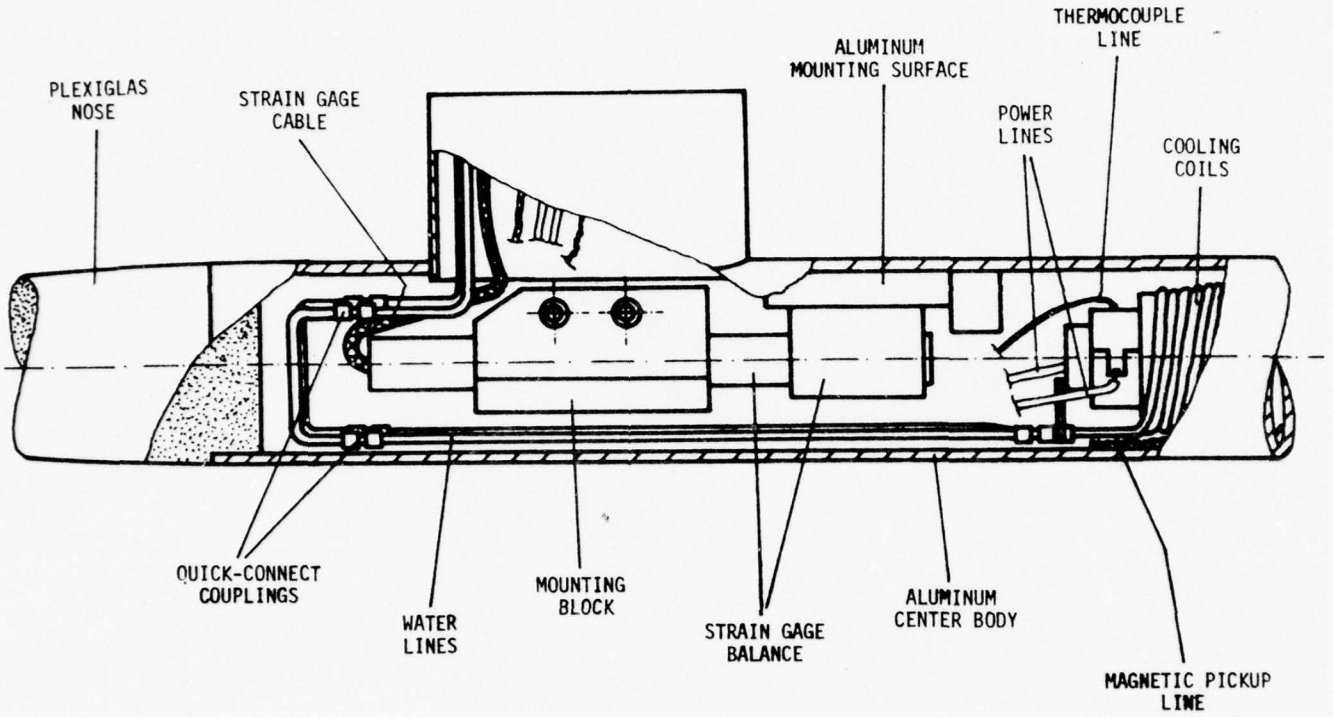

Fig. 4 CUTAWAY OF CYLINDRICAL CENTER BODY SHOWING STRAIN GAGE BALANCE

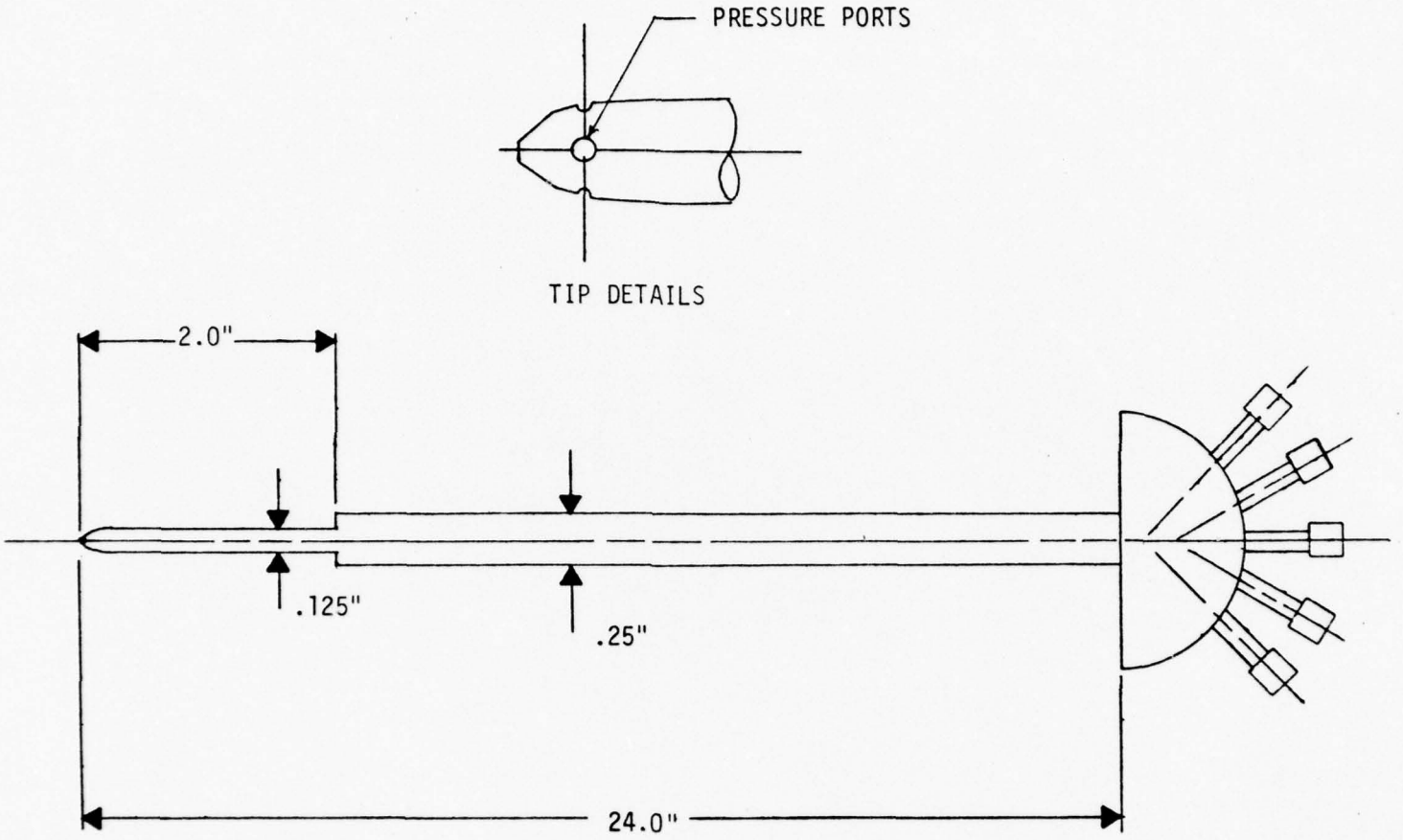

Fig. 5 YAWHEAD PROBE

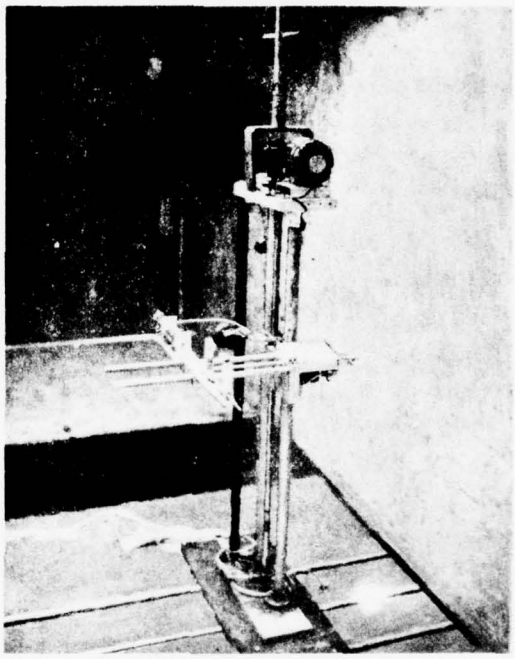

FIG. 6 AUTOMATIC TRAVERSE

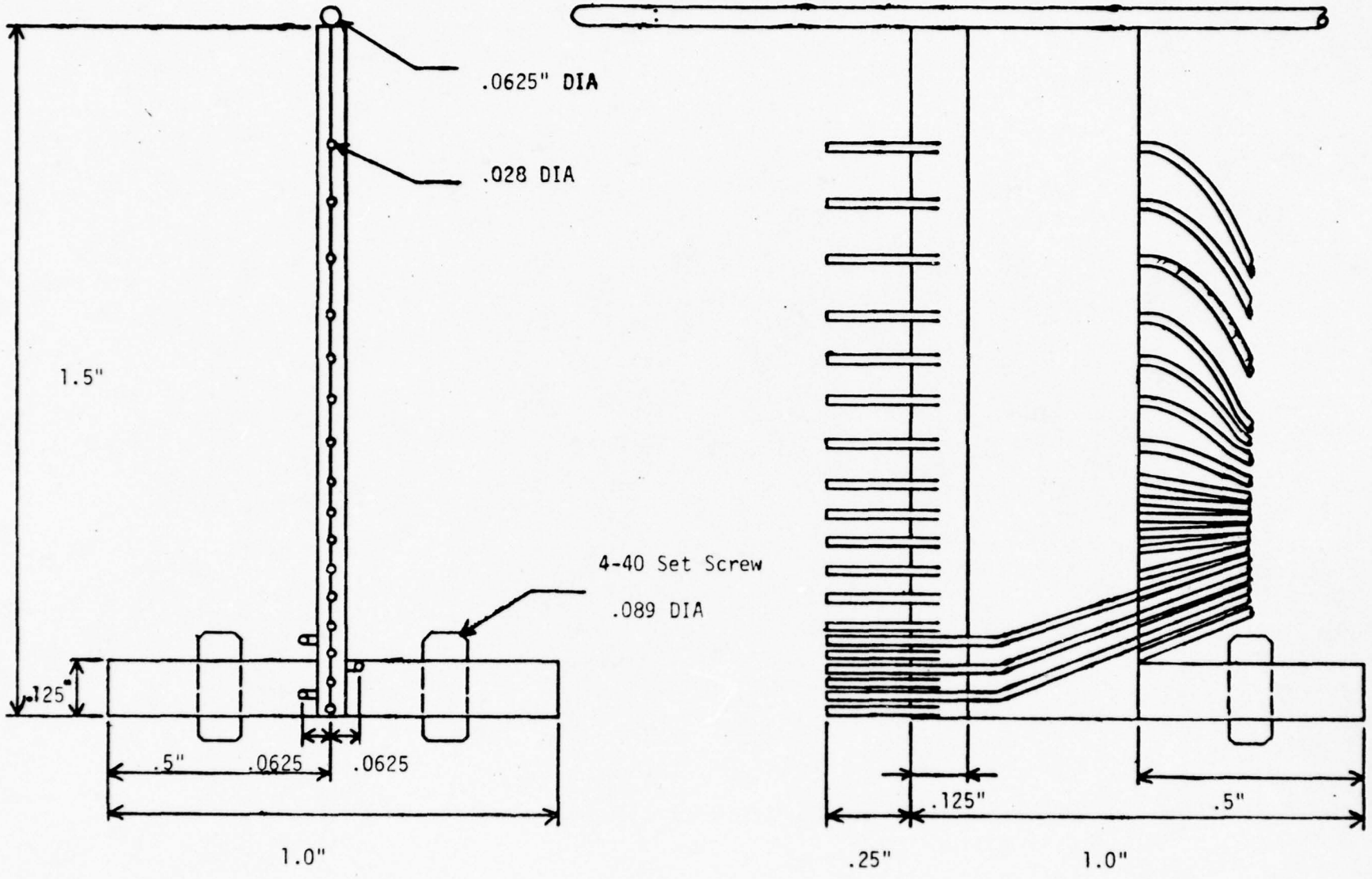

Figure 7: Schematic of the Boundary Layer Rake

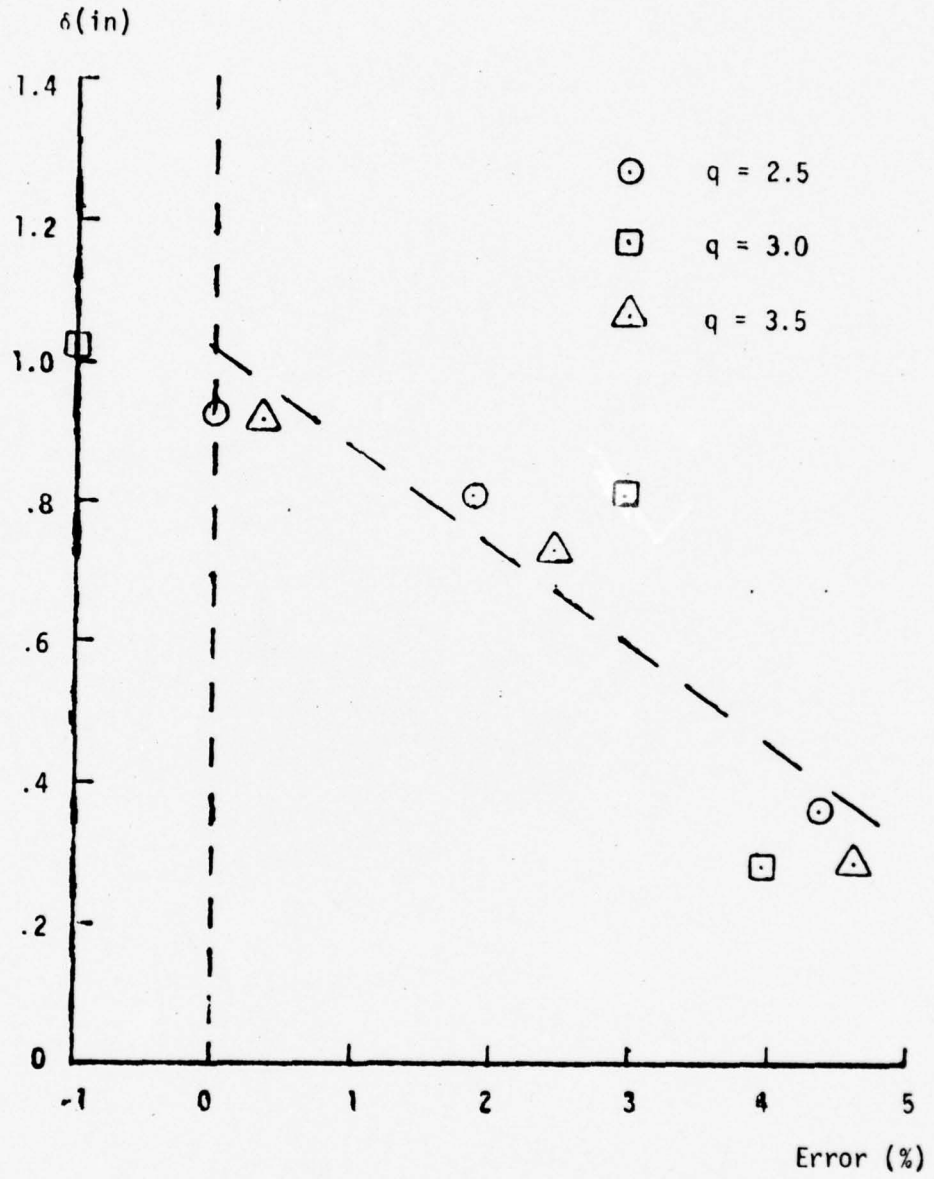

Figure 8 : Percent Error Between Single Pitot-Static Tube and Boundary Layer Rake Pitot-Static Tube

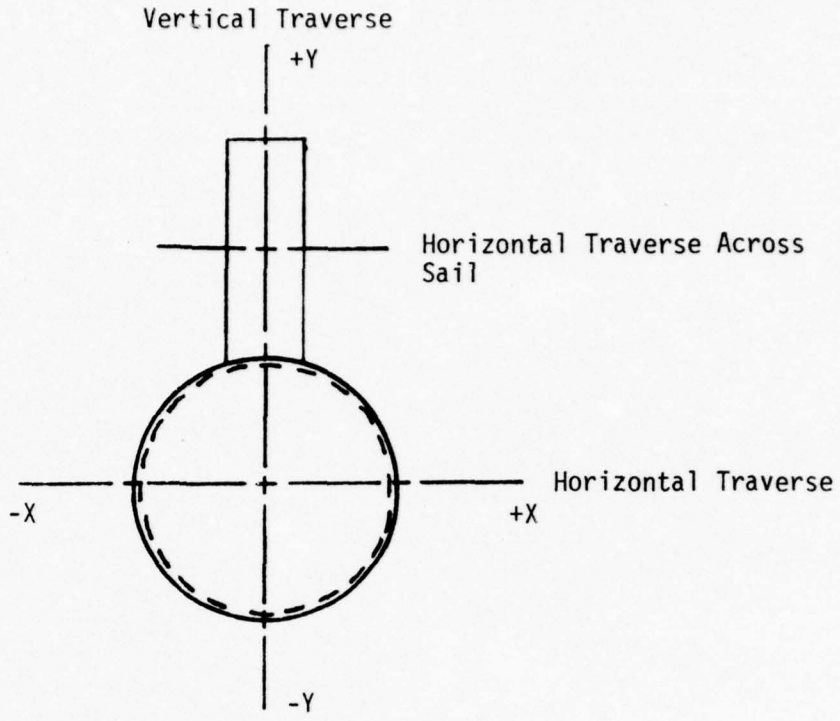

a) Single Propeller Model

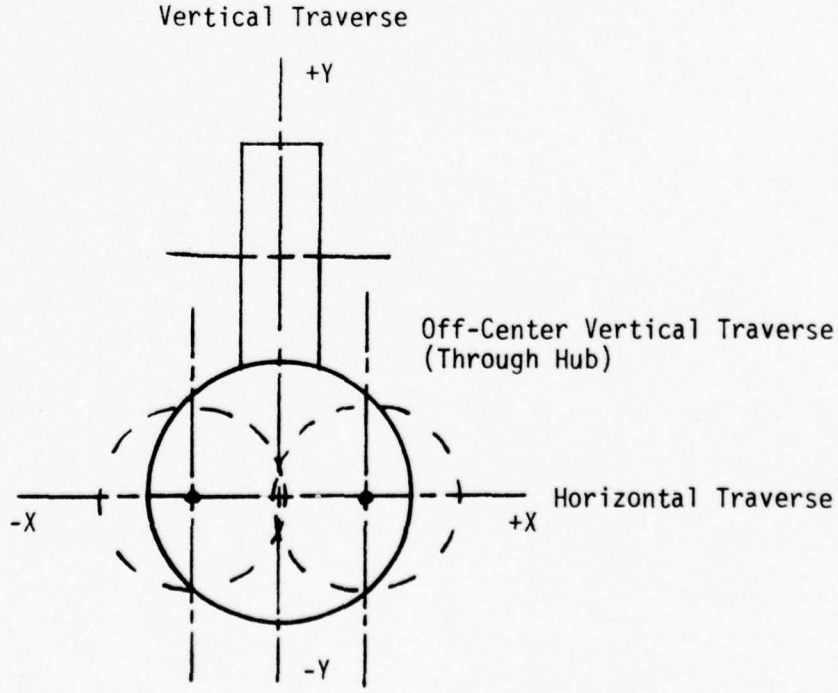

b) Dual Propeller Model

FIG. 9 WAKE TRAVERSE PATHS (Looking Upstream)

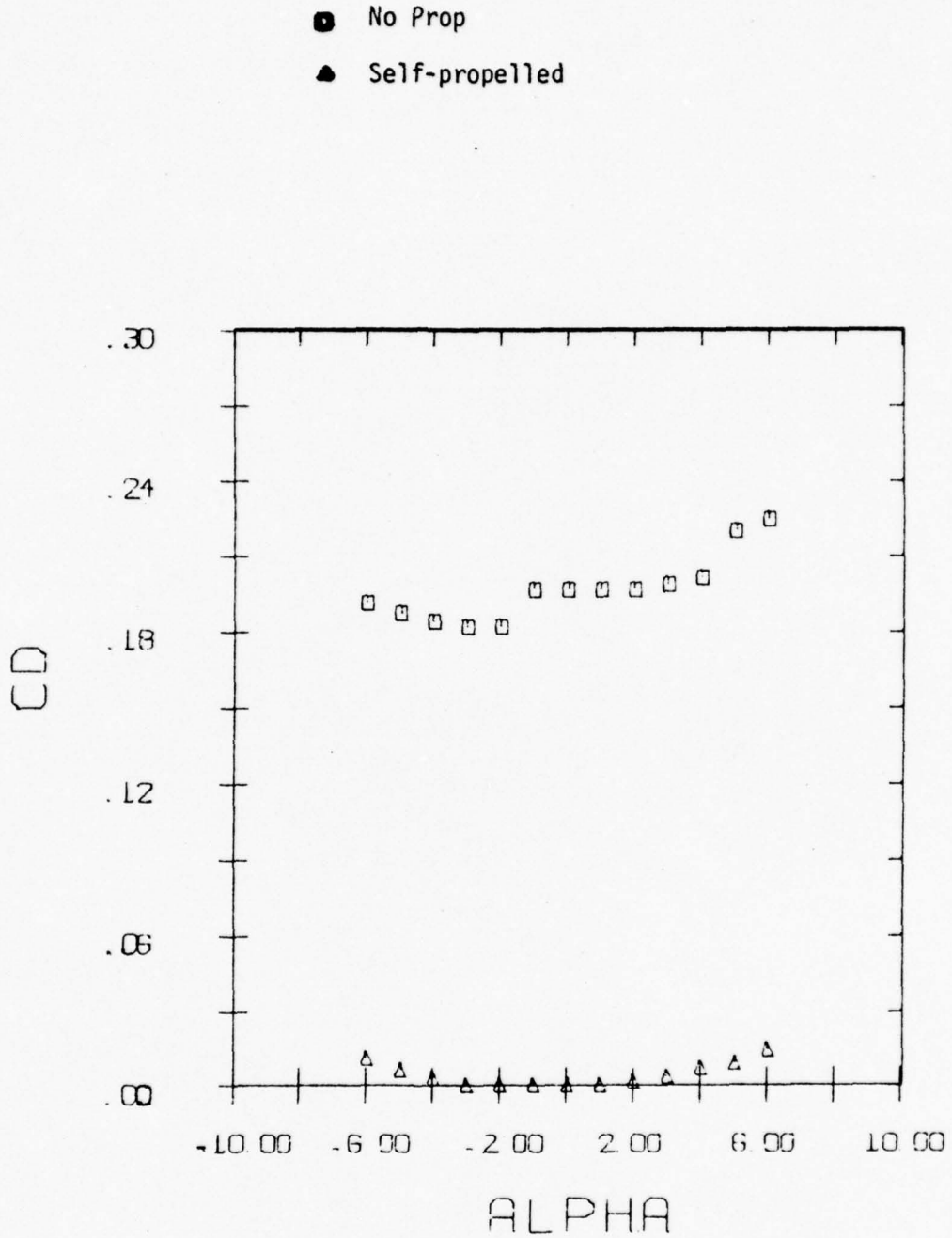

Fig. 10 Drag Coefficient vs. Pitch Angle For Single Propeller Model

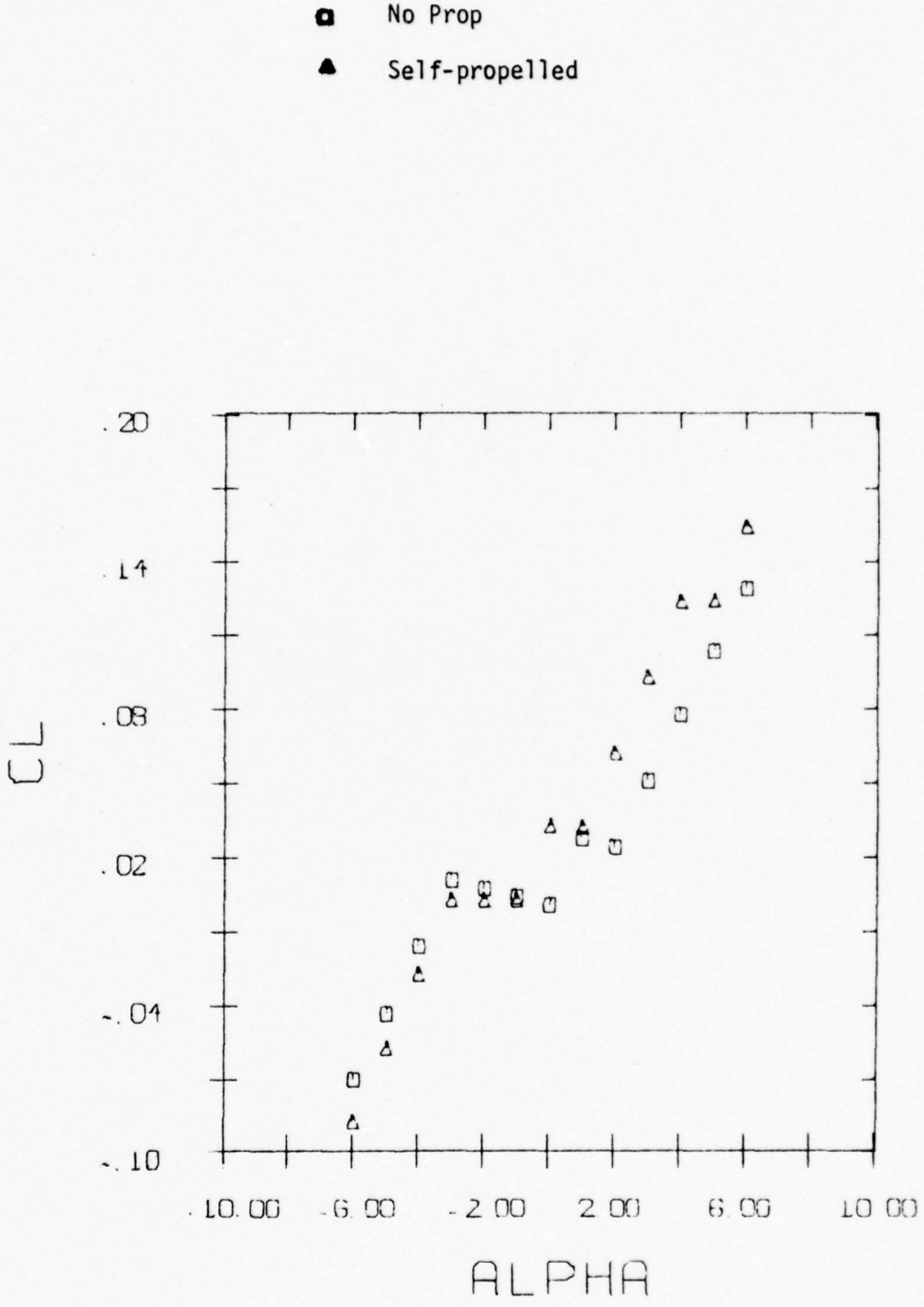

Fig. 11 Lift Coefficient vs. Pitch Angle
For Single Propeller Model

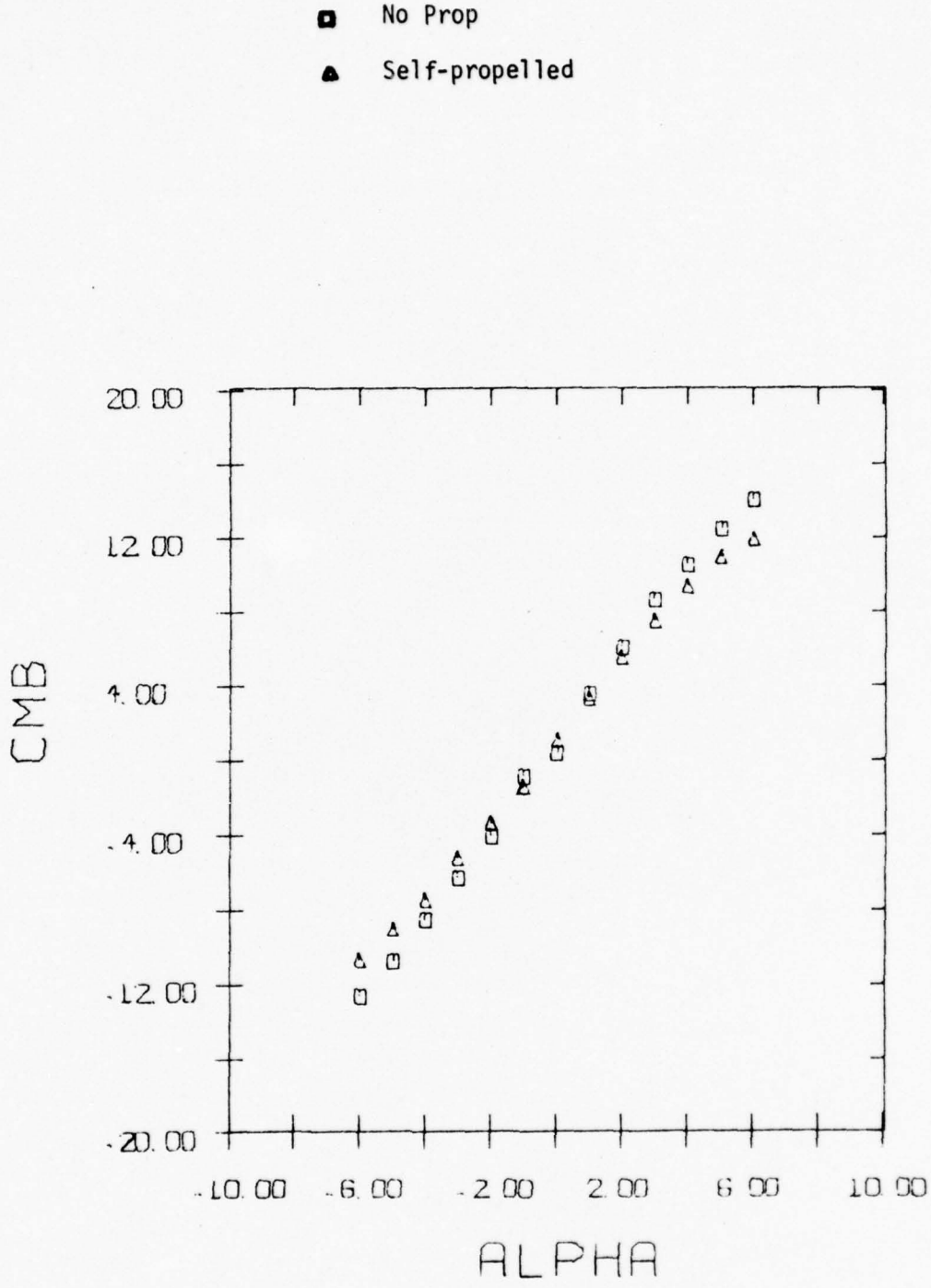

Fig. 12 Pitching Moment vs. Pitch Angle for Single Propeller Model

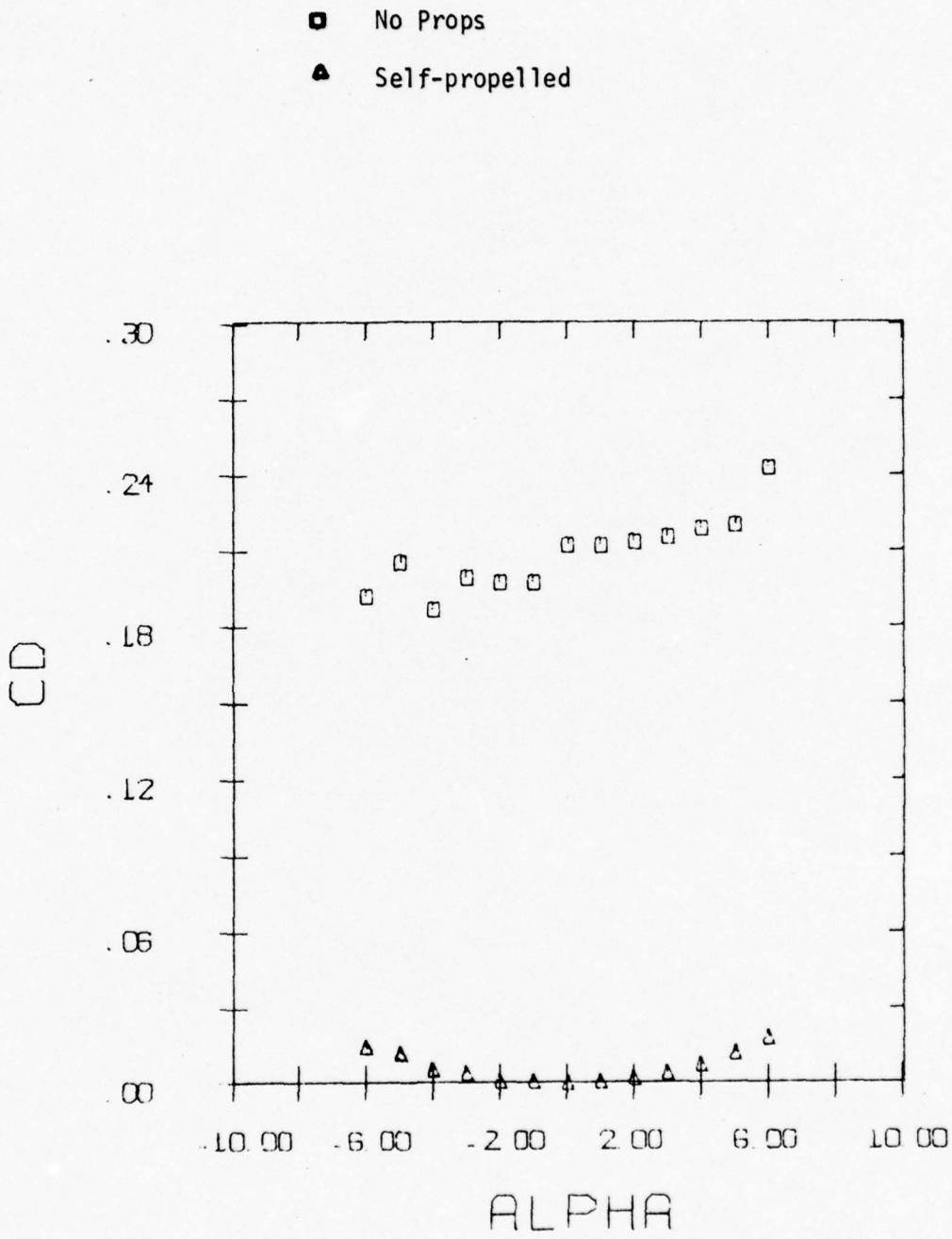

Fig. 13 Drag Coefficient vs. Pitch Angle
For Dual Propeller Model

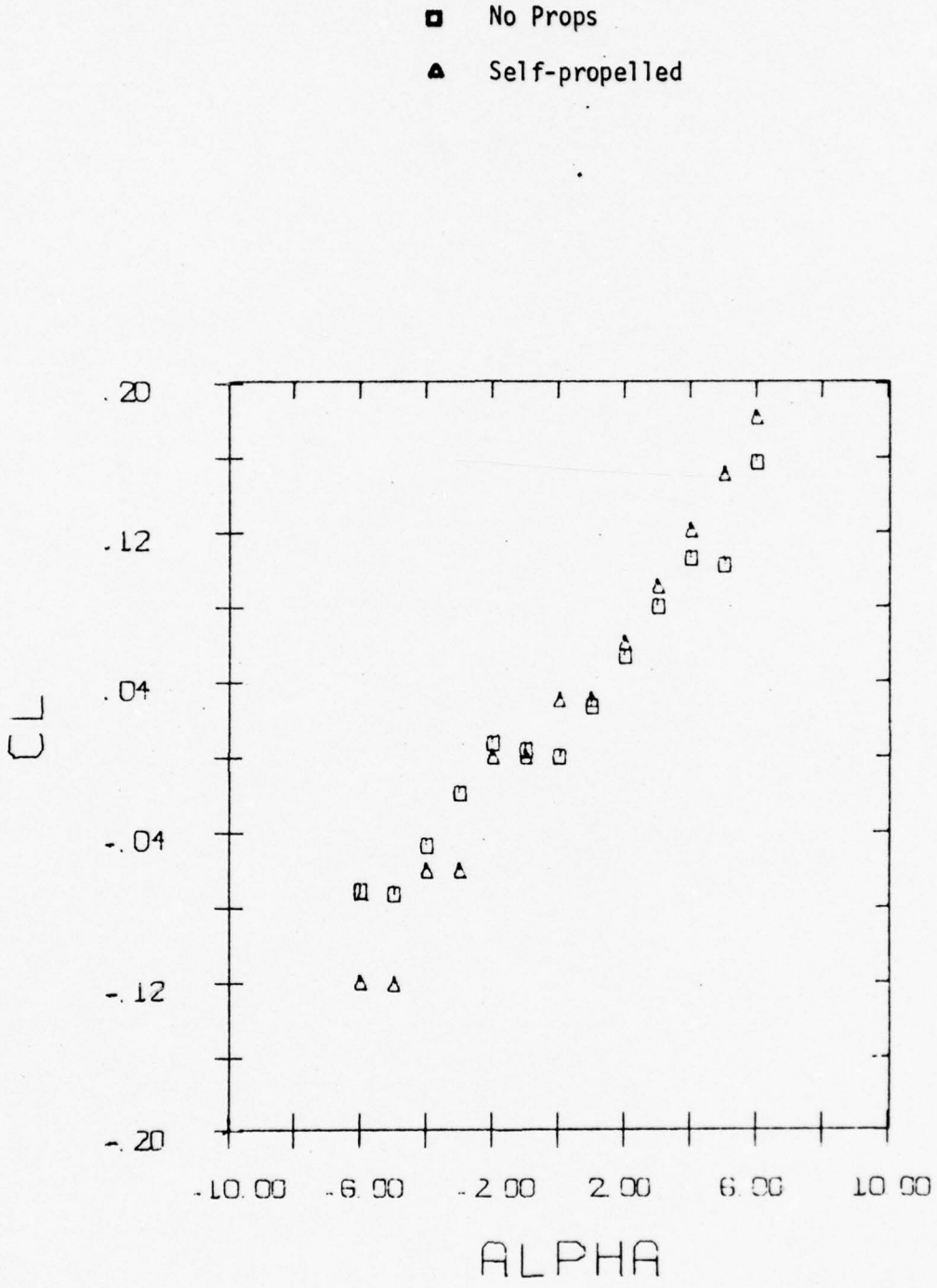

Fig. 14 Lift Coefficient vs. Pitch Angle for Dual Propeller Model

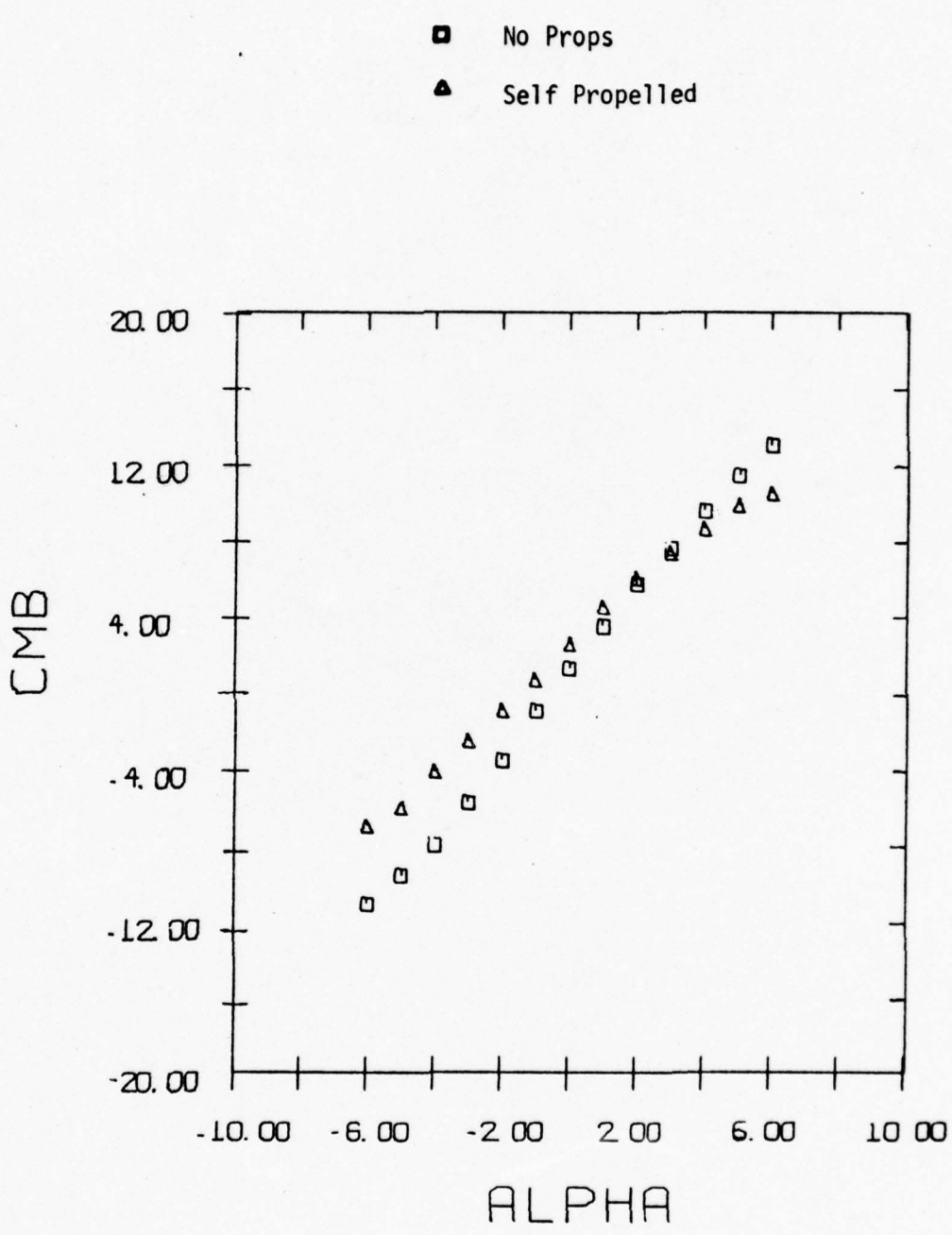

Fig. 15 Pitching Moment vs. Pitch Angle for the Dual Propeller Model

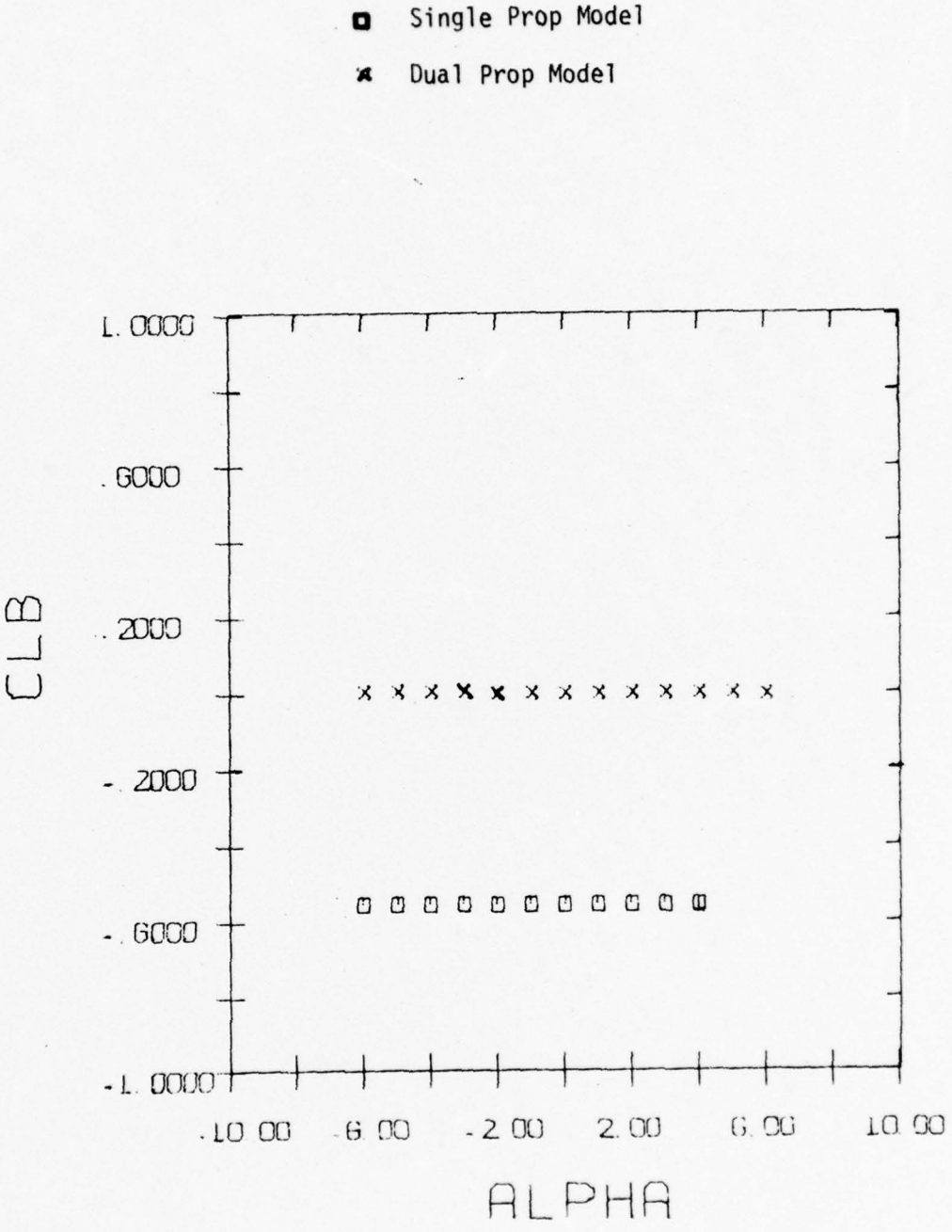

Fig. 16 Rolling Moment vs. Pitch Angle for Both Models in a Self Propelled Condition

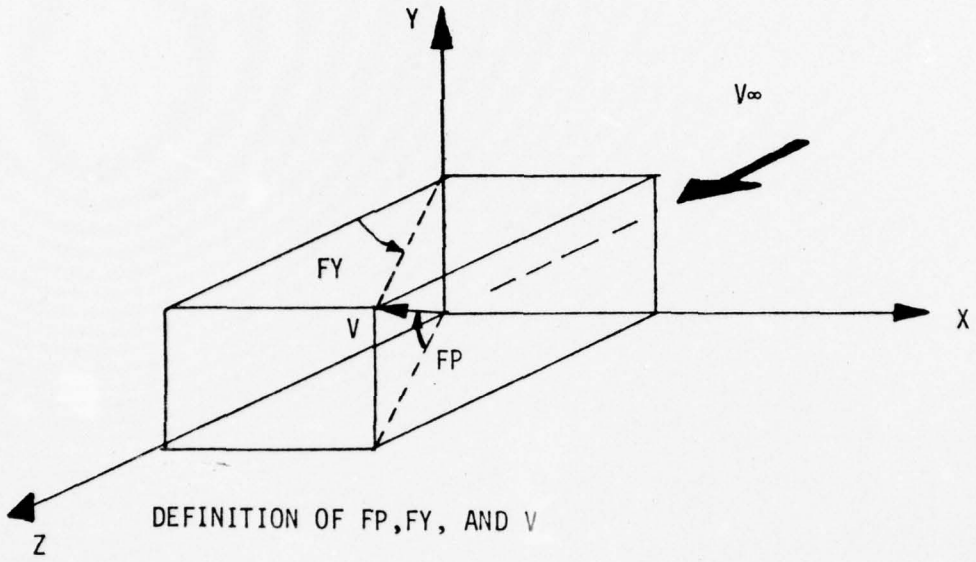

DEFINITION OF FP, FY, AND V

Fig. 17a COORDINATE SYSTEMS

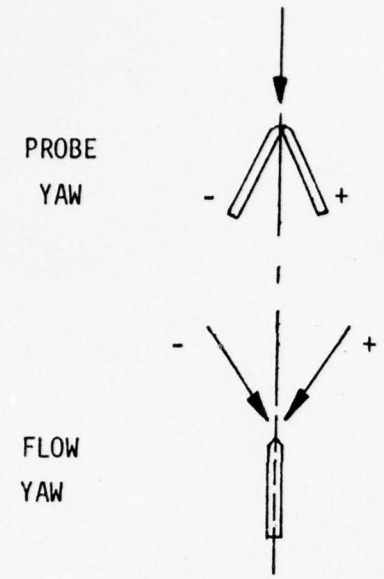

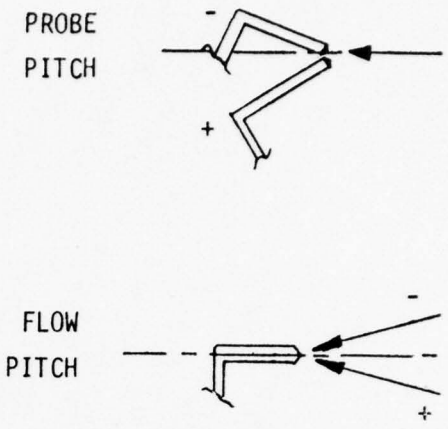

YAW ANGLE = PROBE YAW-FLOW YAW

PITCH ANGLE = PROBE PITCH-FLOW PITCH

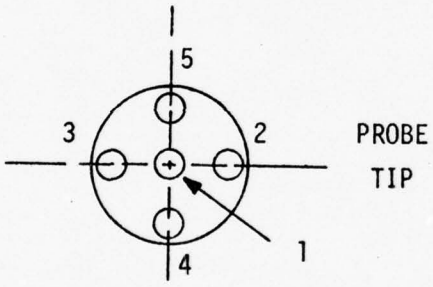

LOOKING DOWNSTREAM

Fig. 17b SIGN CONVENTIONS

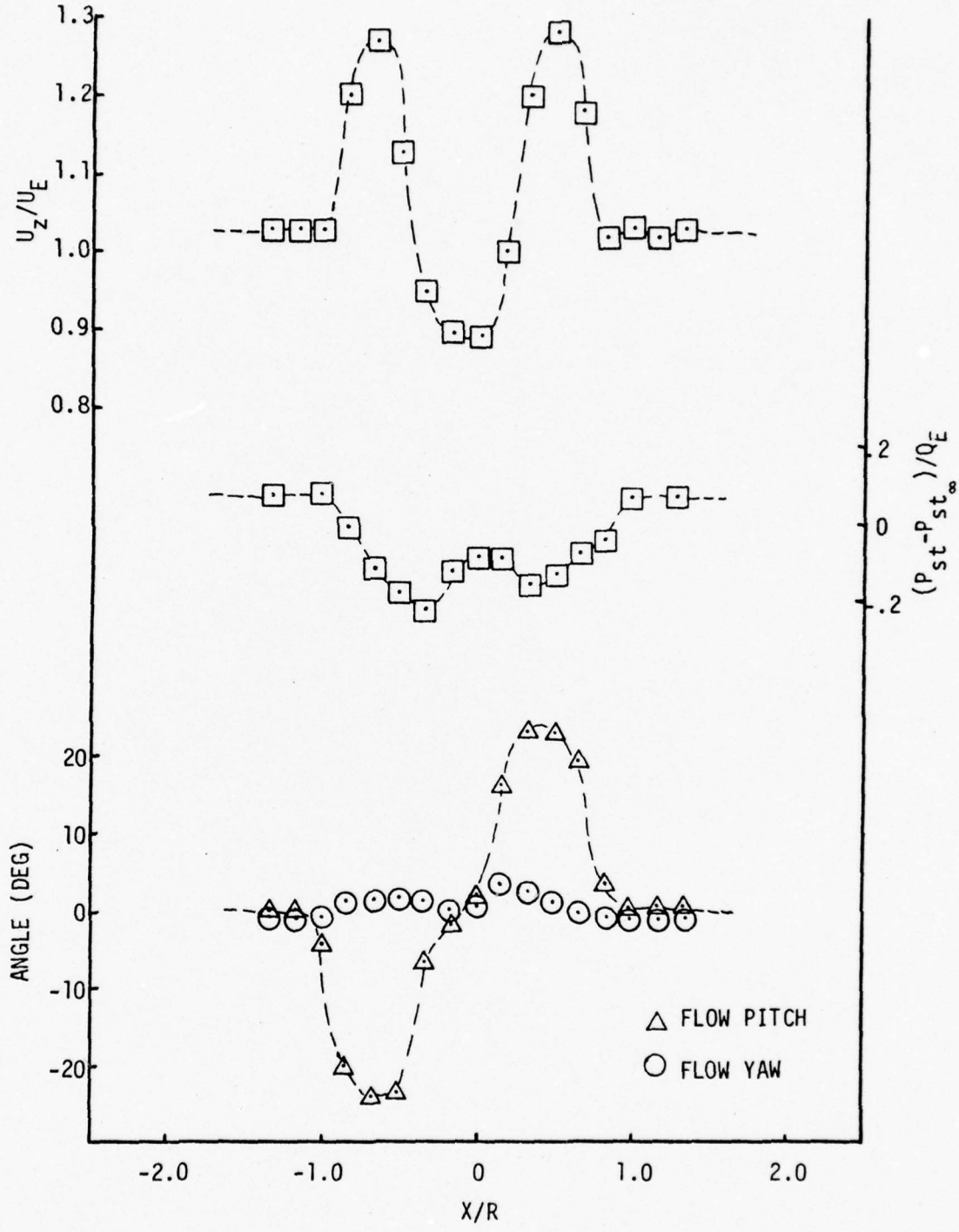

Fig. 18 MEAN AXIAL VELOCITY , FLOW ANGULARITY, AND STATIC PRESSURE HORIZONTAL PROFILE AT Z/D=2, Y/R=0, α_e=0°

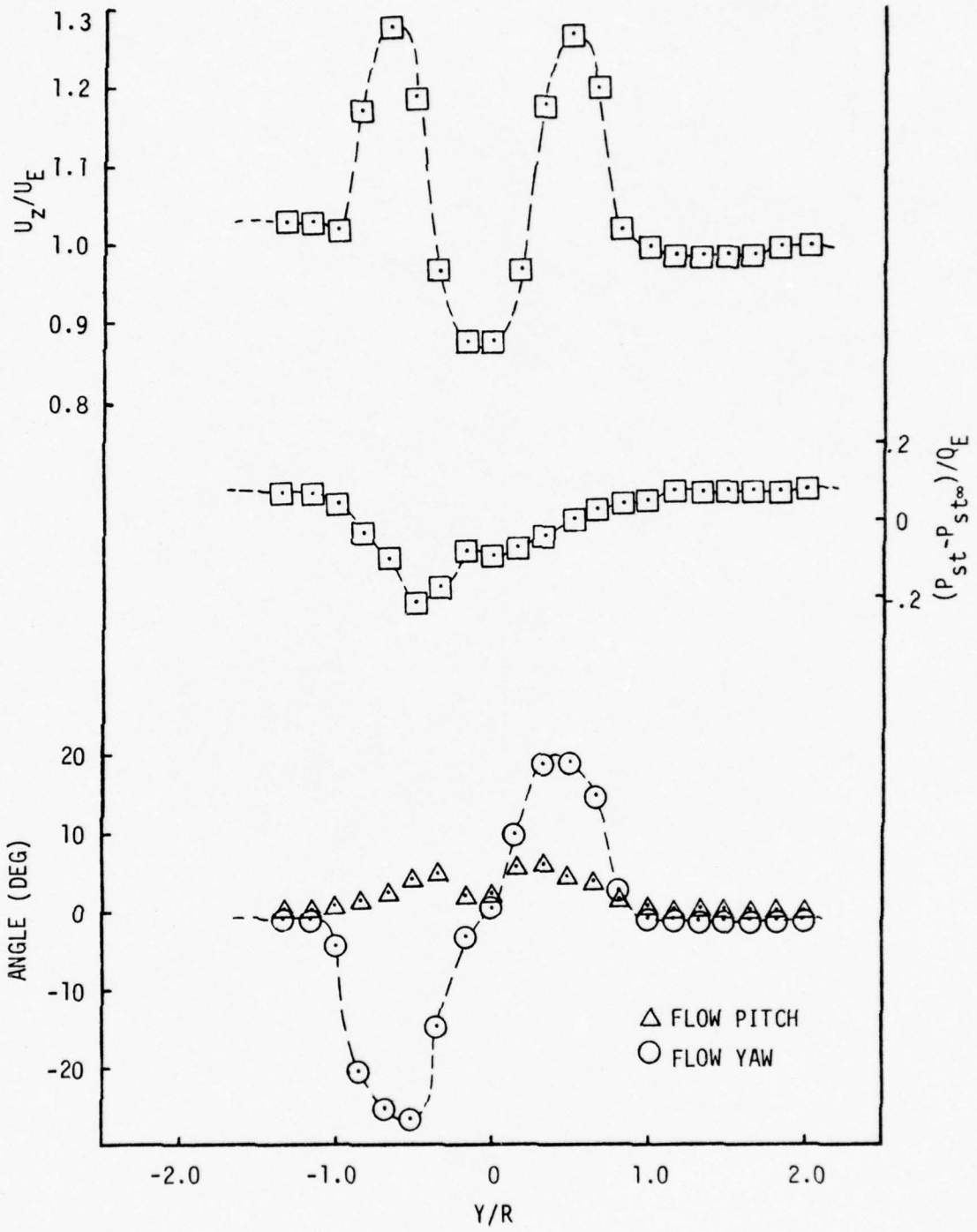

Fig. 19 MEAN AXIAL VELOCITY, FLOW ANGULARITY, AND STATIC PRESSURE VERTICAL PROFILE AT Z/D=2, X/R=0, α_e=0°

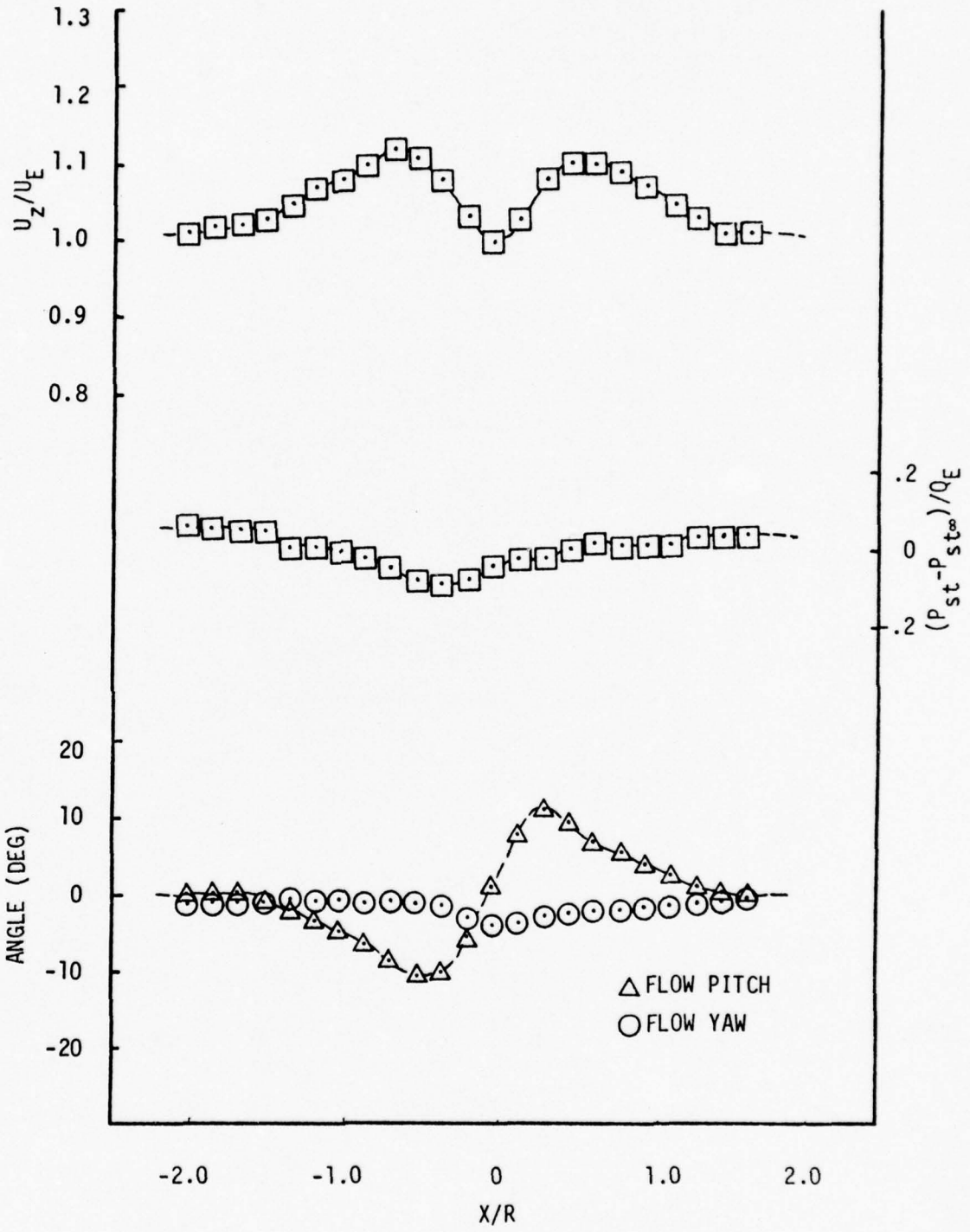

Fig. 20 MEAN AXIAL VELOCITY, FLOW ANGULARITY, AND STATIC PRESSURE HORIZONTAL PROFILE AT Z/D=10, Y/R=0, $\alpha_e=0^\circ$

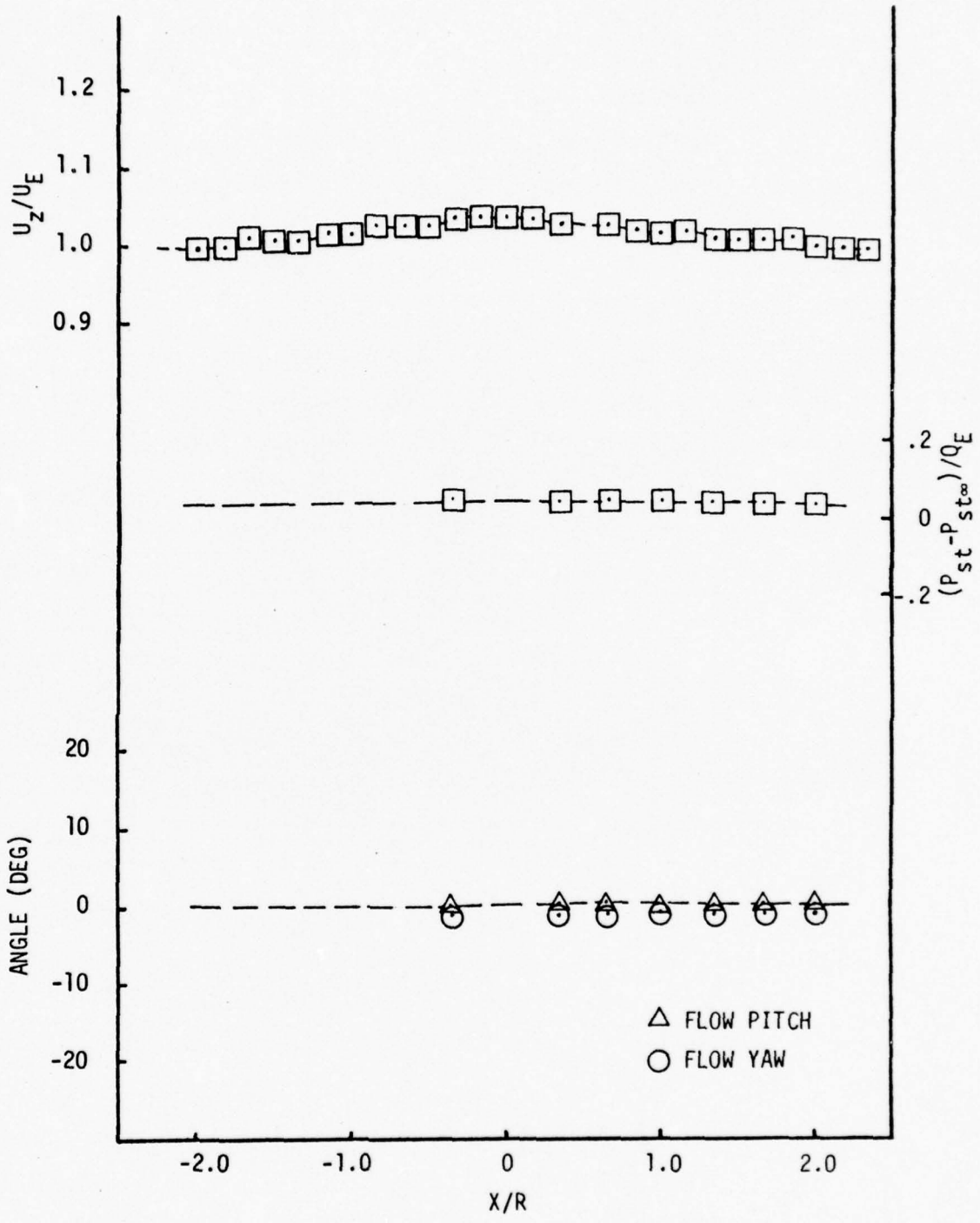

Fig. 21 MEAN AXIAL VELOCITY, FLOW ANGULARITY, AND STATIC PRESSURE HORIZONTAL PROFILE AT Z/D=40, Y/R=0, $\alpha_e=0^\circ$

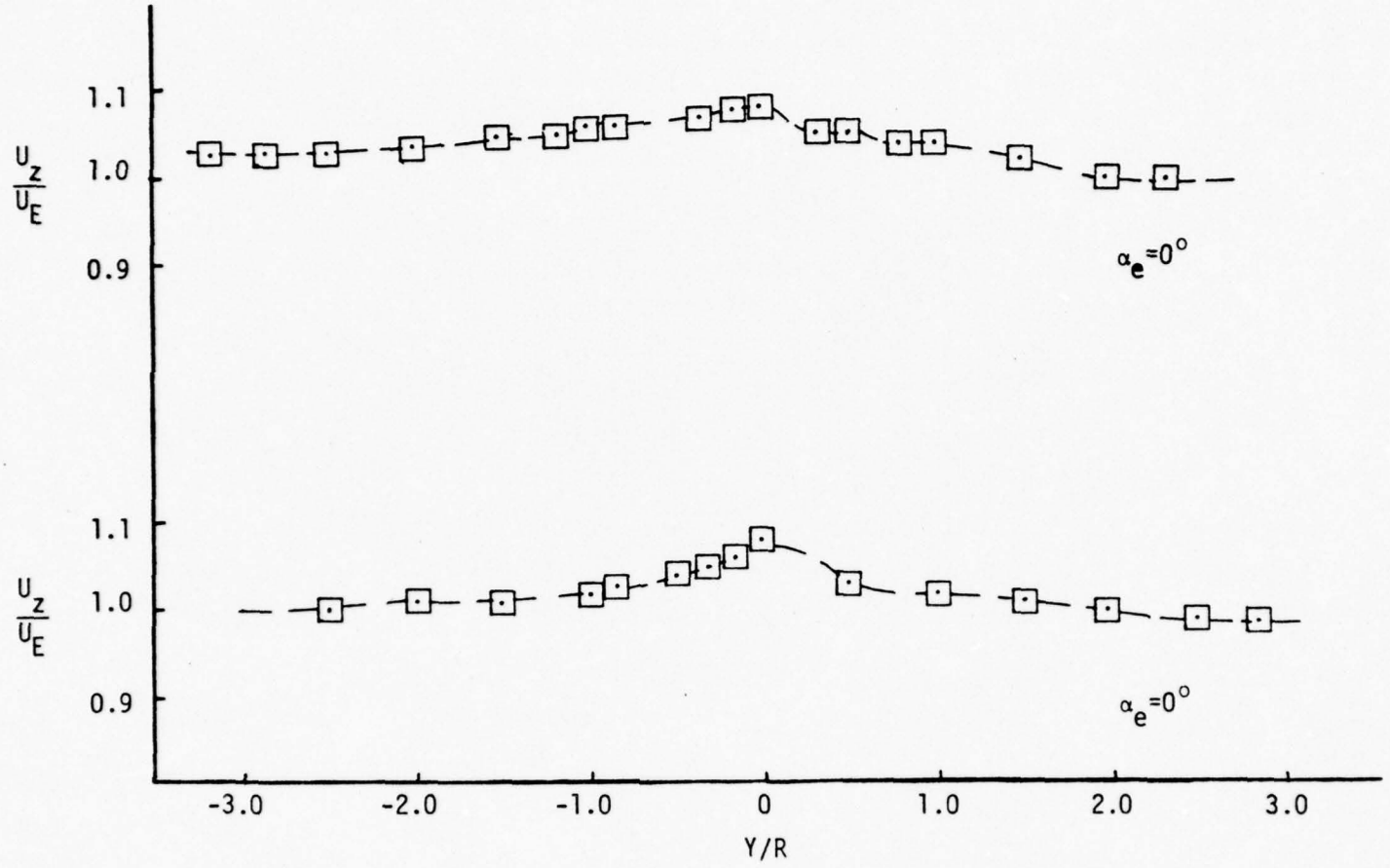

Fig. 22 MEAN AXIAL VELOCITY, VERTICAL PROFILES AT Z/D=40, X/R=0

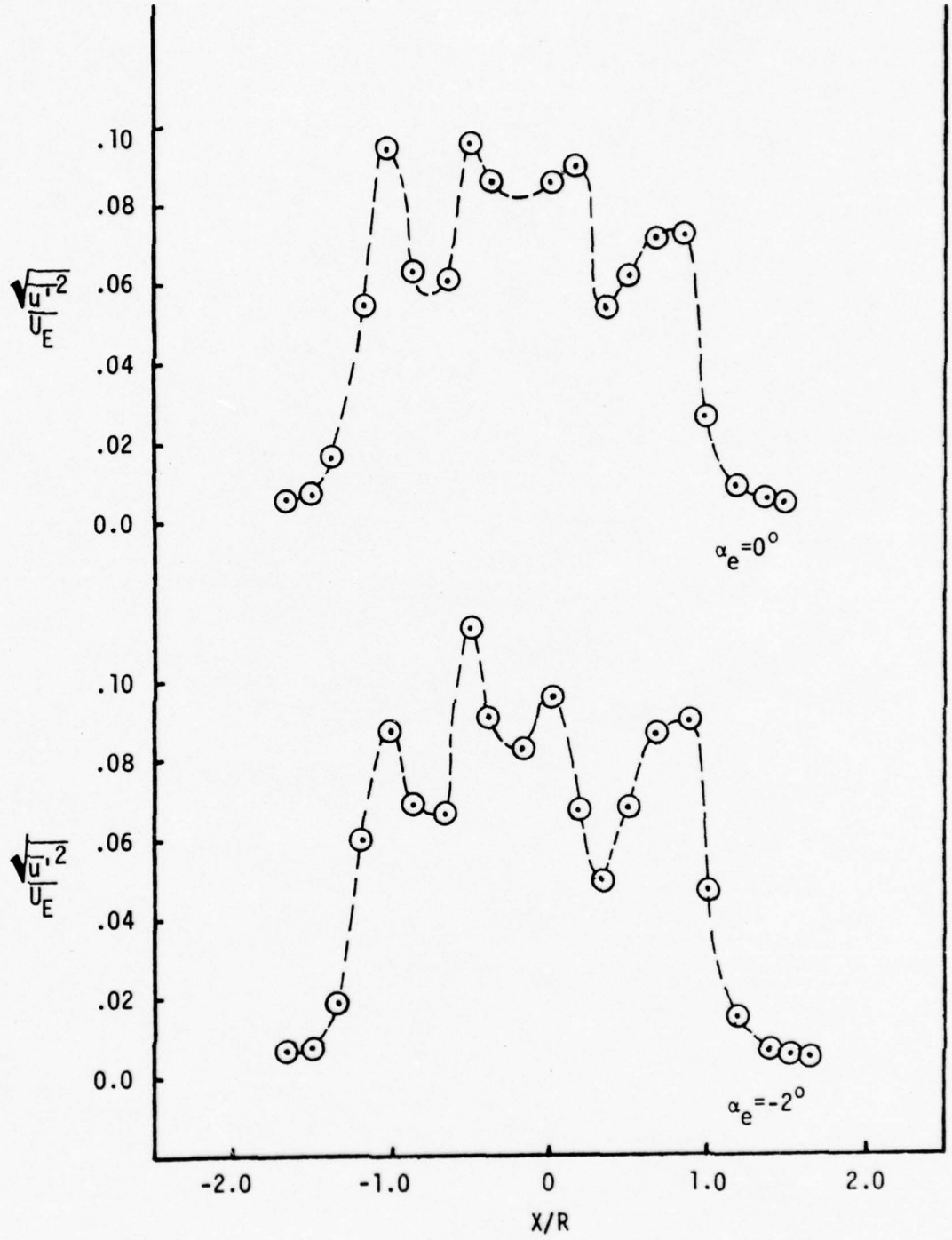

Fig. 23 AXIAL TURBULENCE INTENSITY HORIZONTAL PROFILE AT Z/D=2, Y/R=0

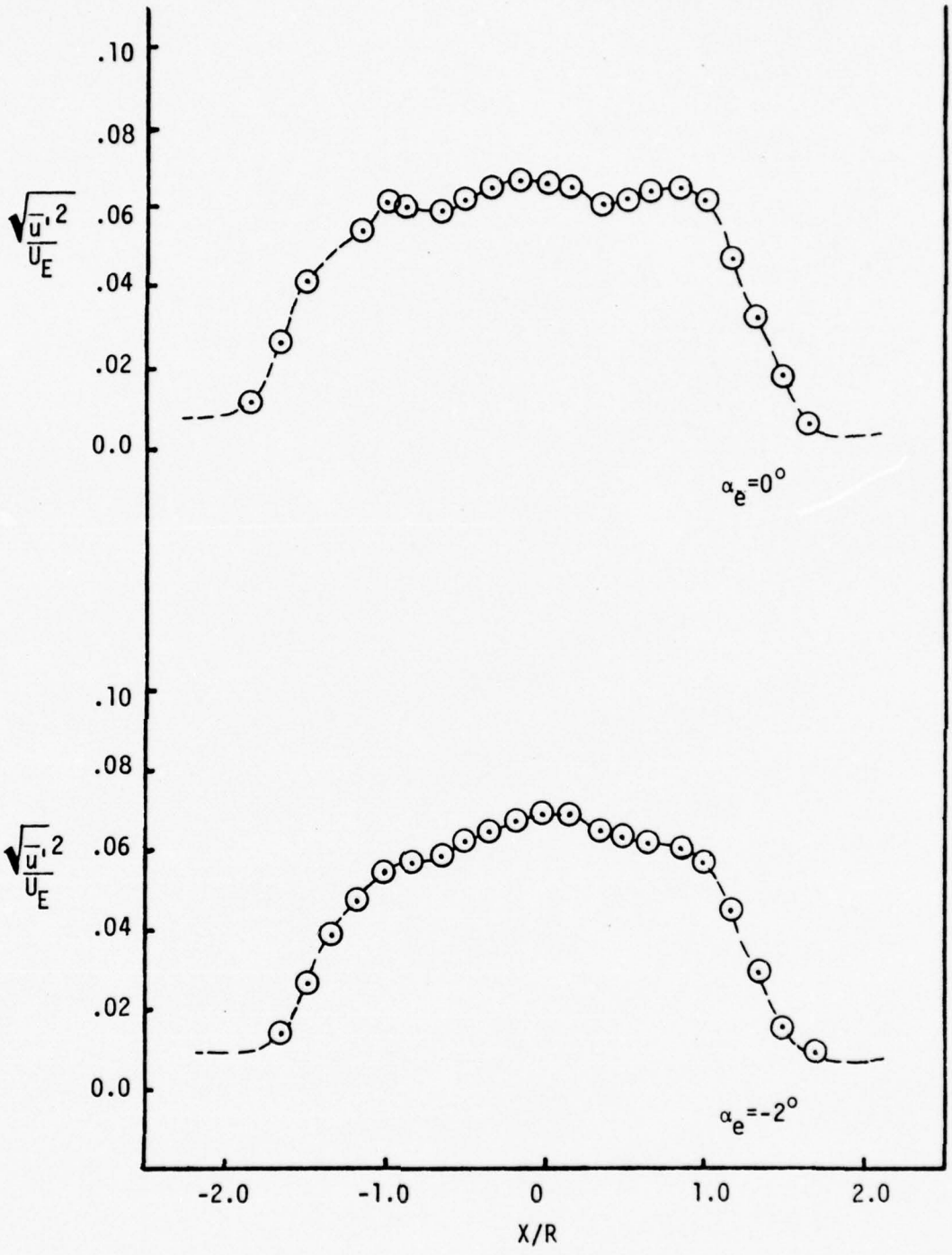

Fig. 24 AXIAL TURBULENCE INTENSITY HORIZONTAL PROFILE AT Z/D=10, Y/R=0

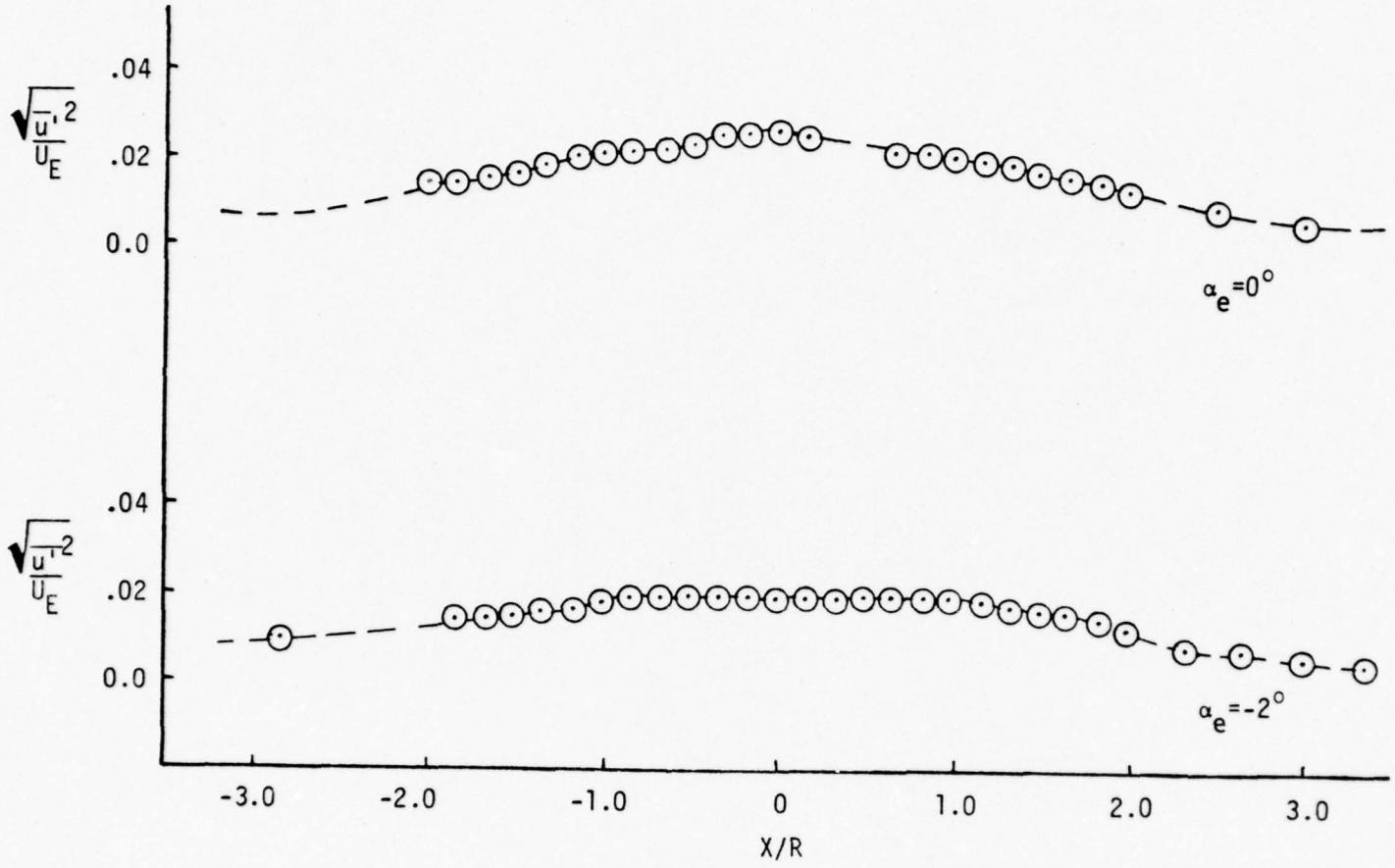

Fig. 25 AXIAL TURBULENCE INTENSITY HORIZONTAL PROFILE AT Z/D=40, Y/R=0

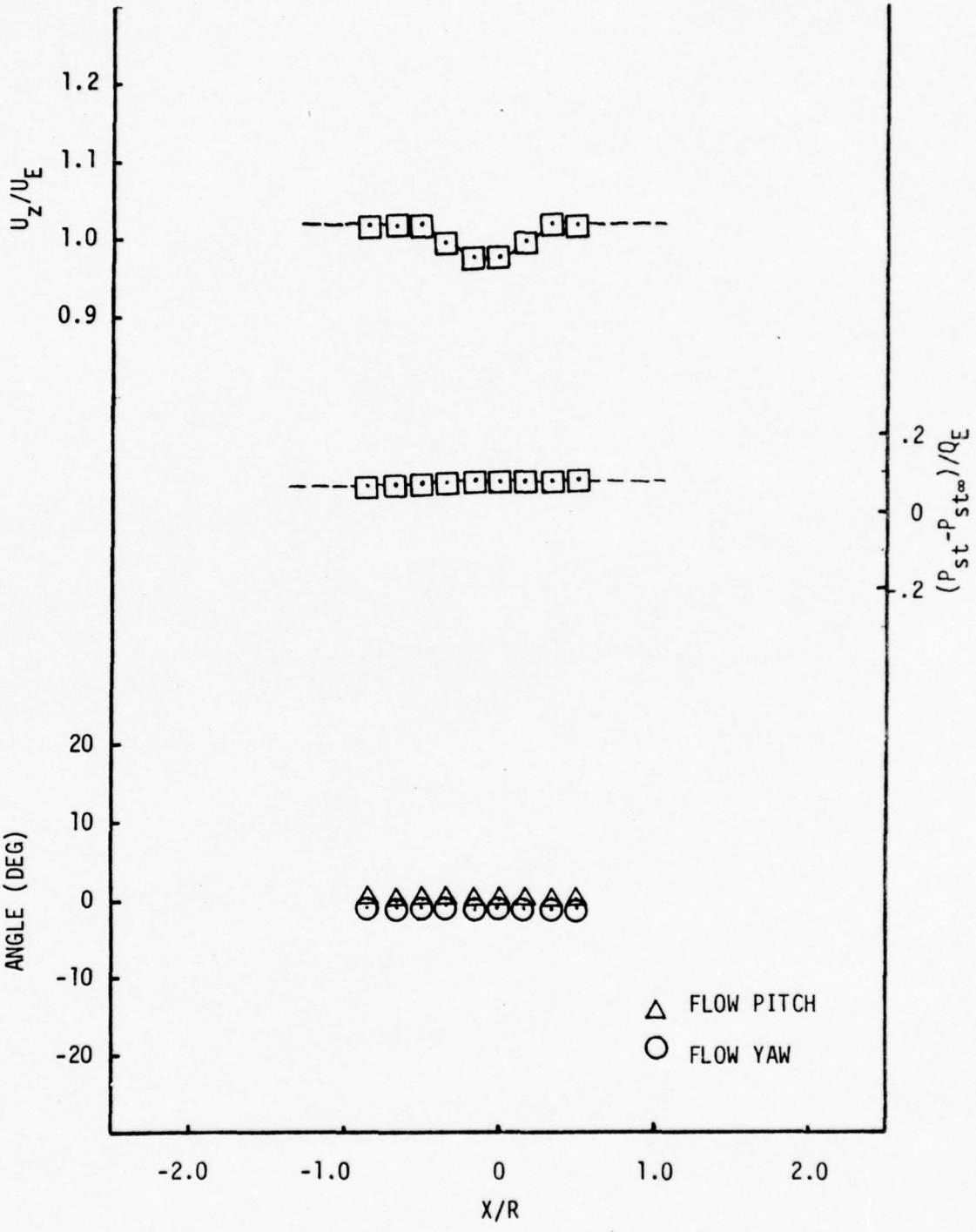

Fig. 26 MEAN AXIAL VELOCITY, FLOW ANGULARITY, AND STATIC PRESSURE ACROSS THE SAIL WAKE AT Z/D=2, Y/R=1.67, α_e=0°

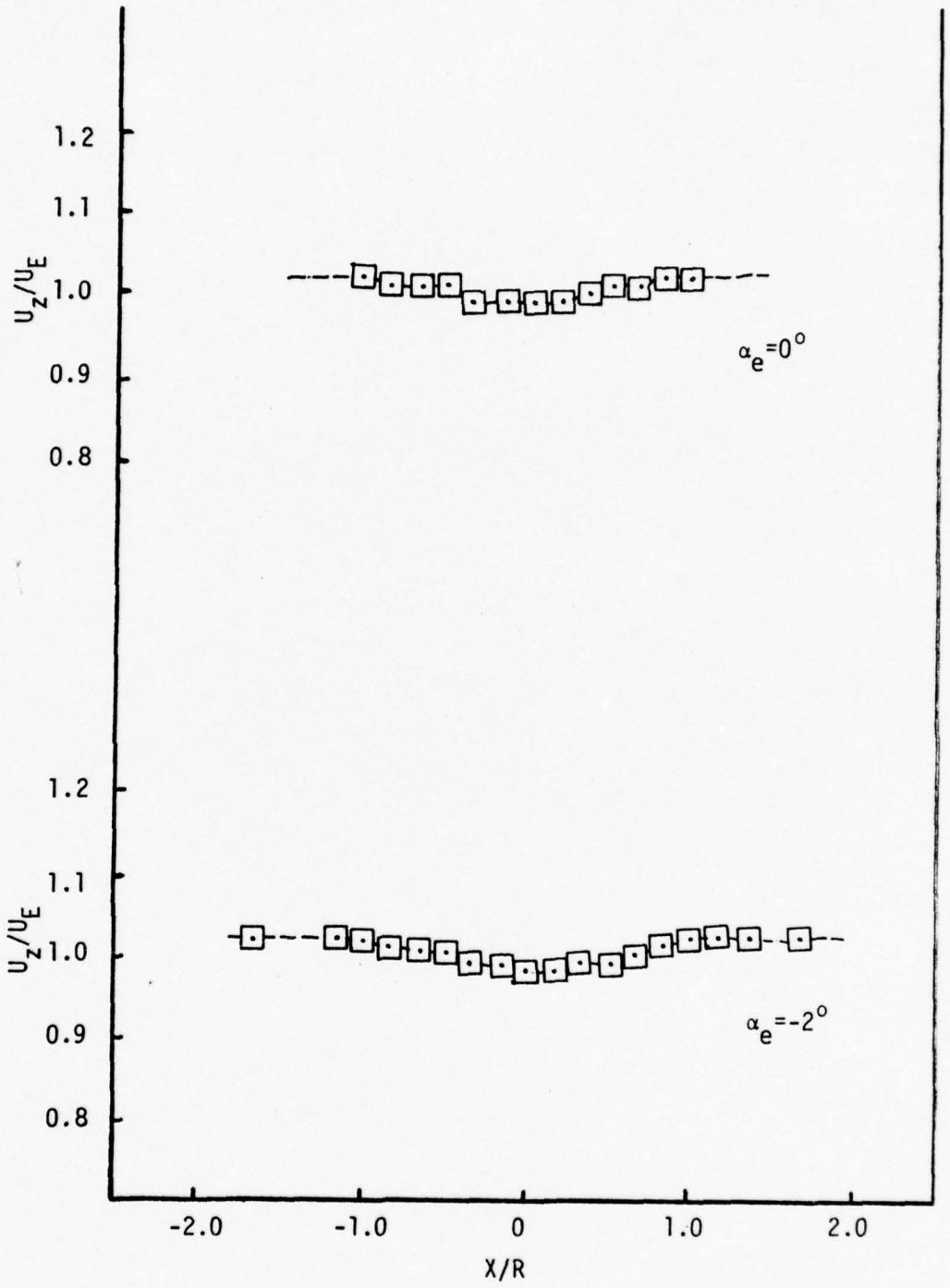

Fig. 27 MEAN AXIAL VELOCITY ACROSS THE SAIL WAKE AT Z/D=10, Y/R=1.67

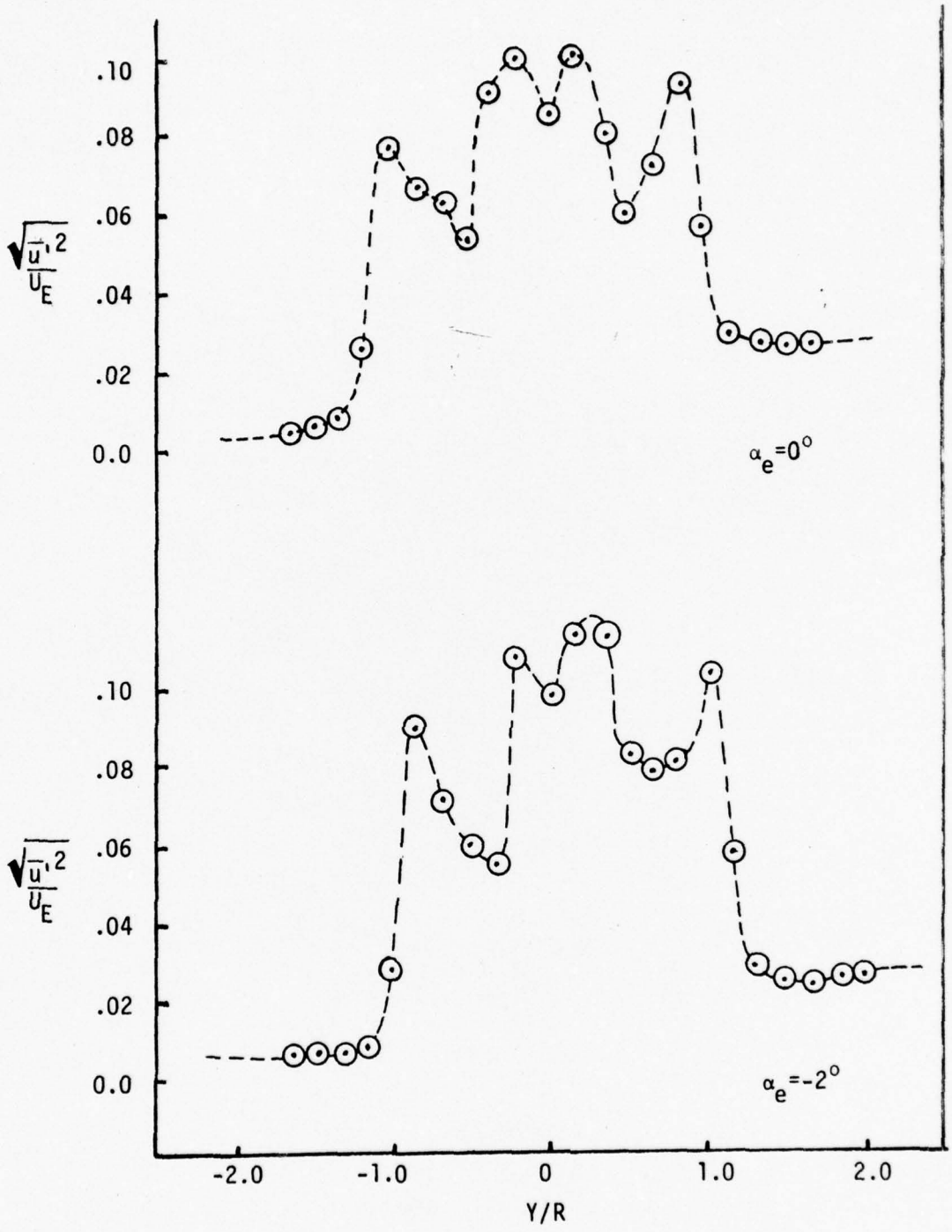

Fig. 28 AXIAL TURBULENCE INTENSITY VERTICAL PROFILE AT Z/D=2, X/R=0

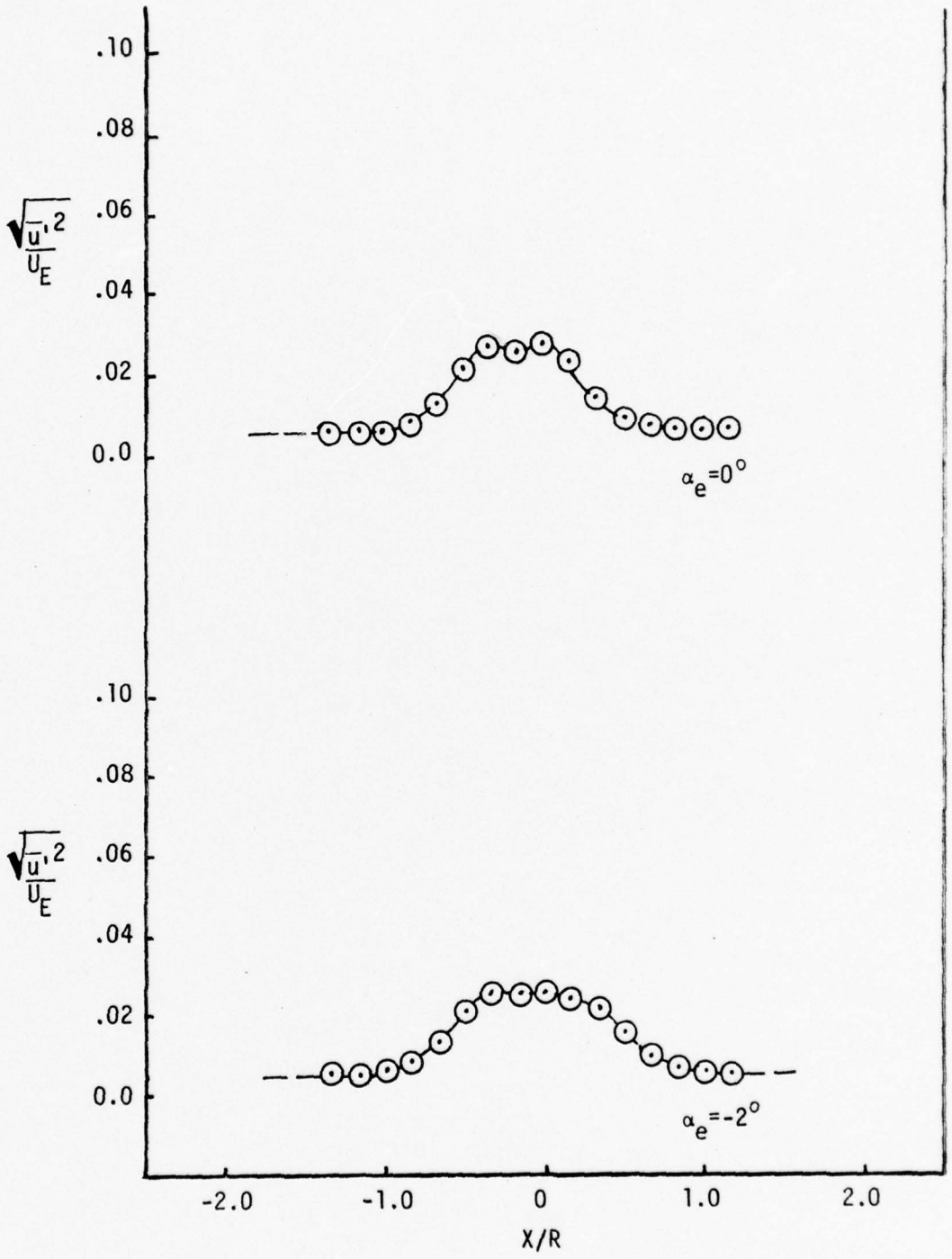

Fig. 29 AXIAL TURBULENCE INTENSITY IN SAIL WAKE AT Z/D=2, Y/R=1.67

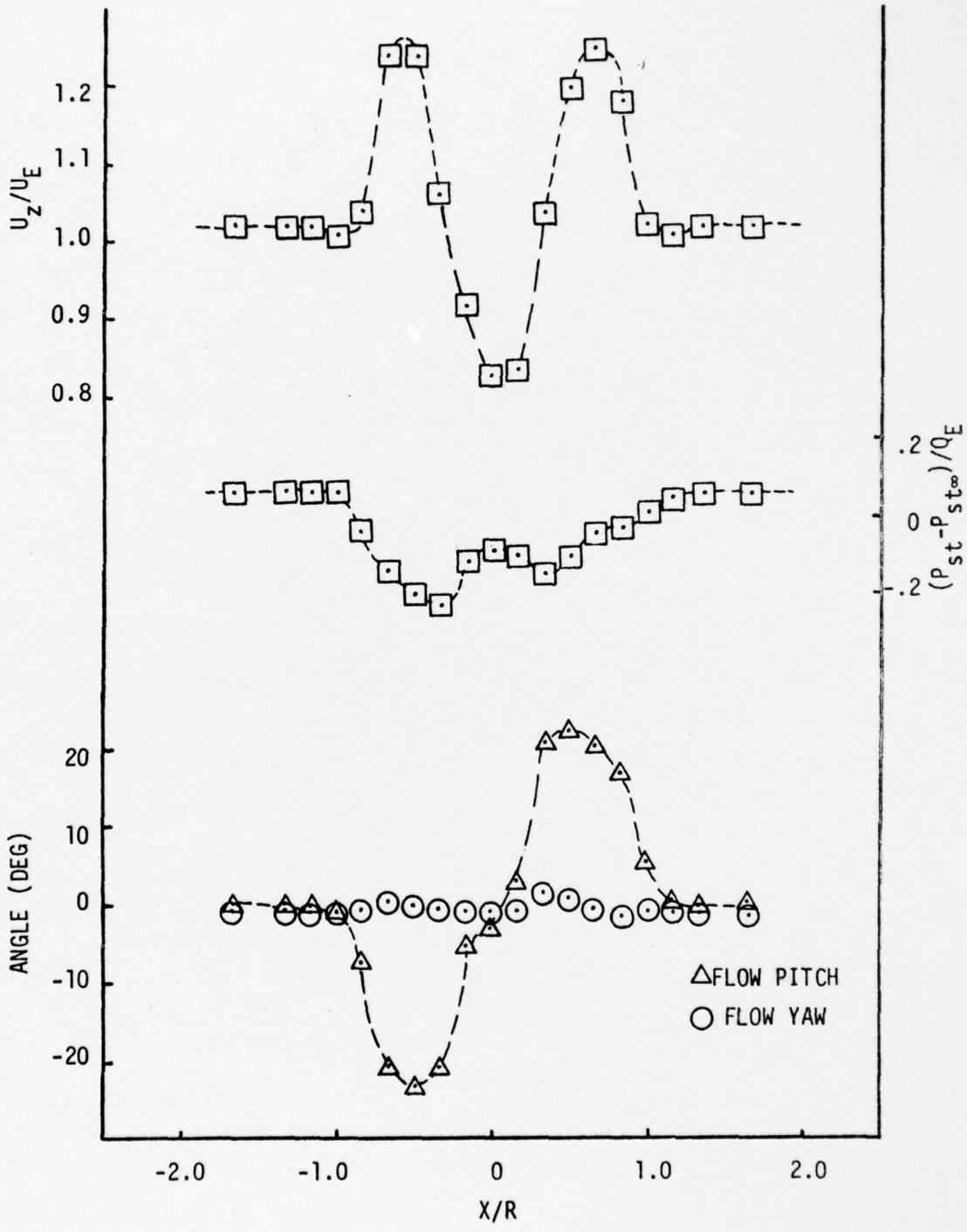

Fig. 30 MEAN AXIAL VELOCITY, FLOW ANGULARITY, AND STATIC PRESSURE HORIZONTAL PROFILE AT Z/D=2,Y/R=0, α_e=-2°

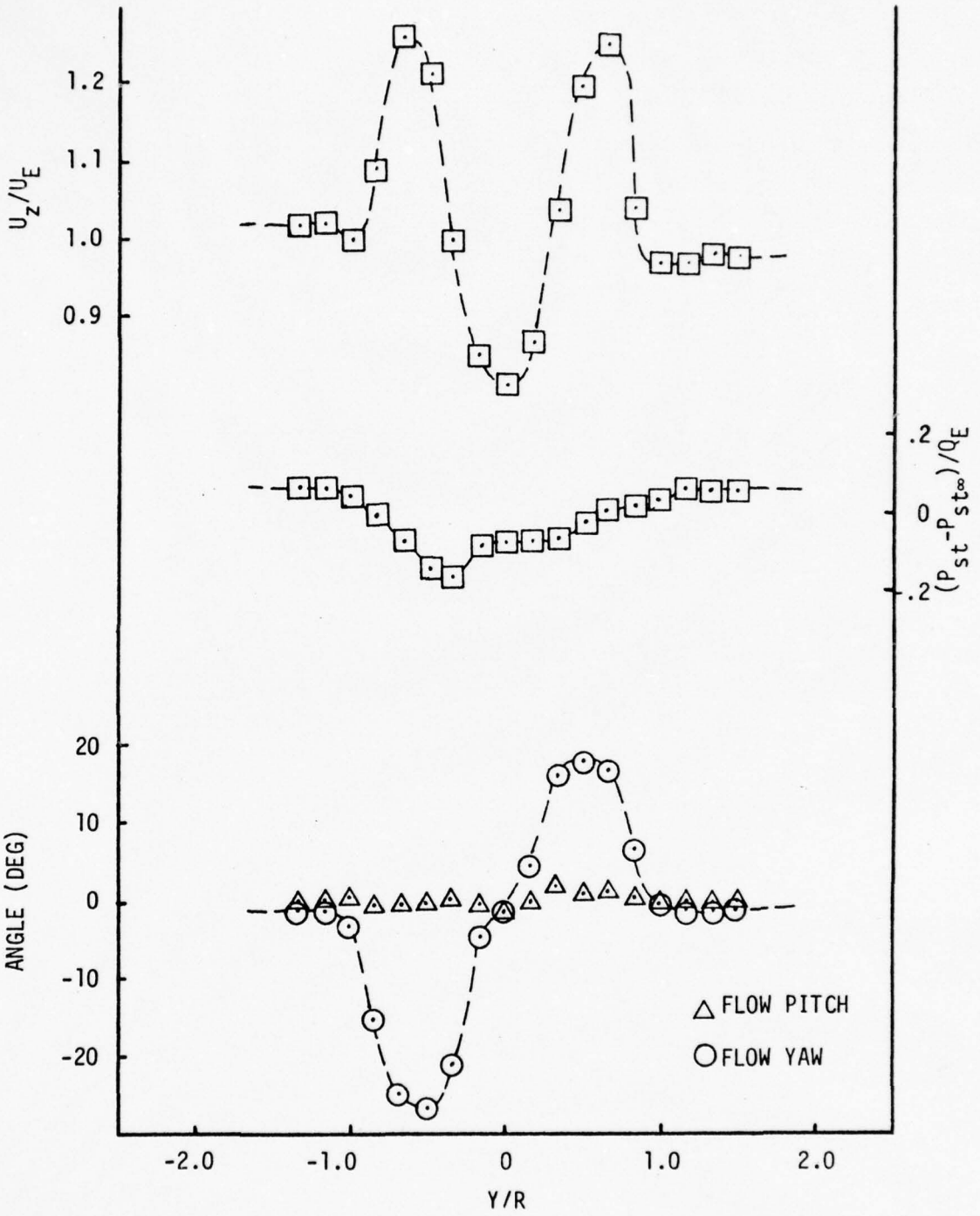

Fig. 31 MEAN AXIAL VELOCITY, FLOW ANGULARITY, AND STATIC PRESSURE VERTICAL PROFILE AT Z/D=2, X/R=0, α_e=-2°

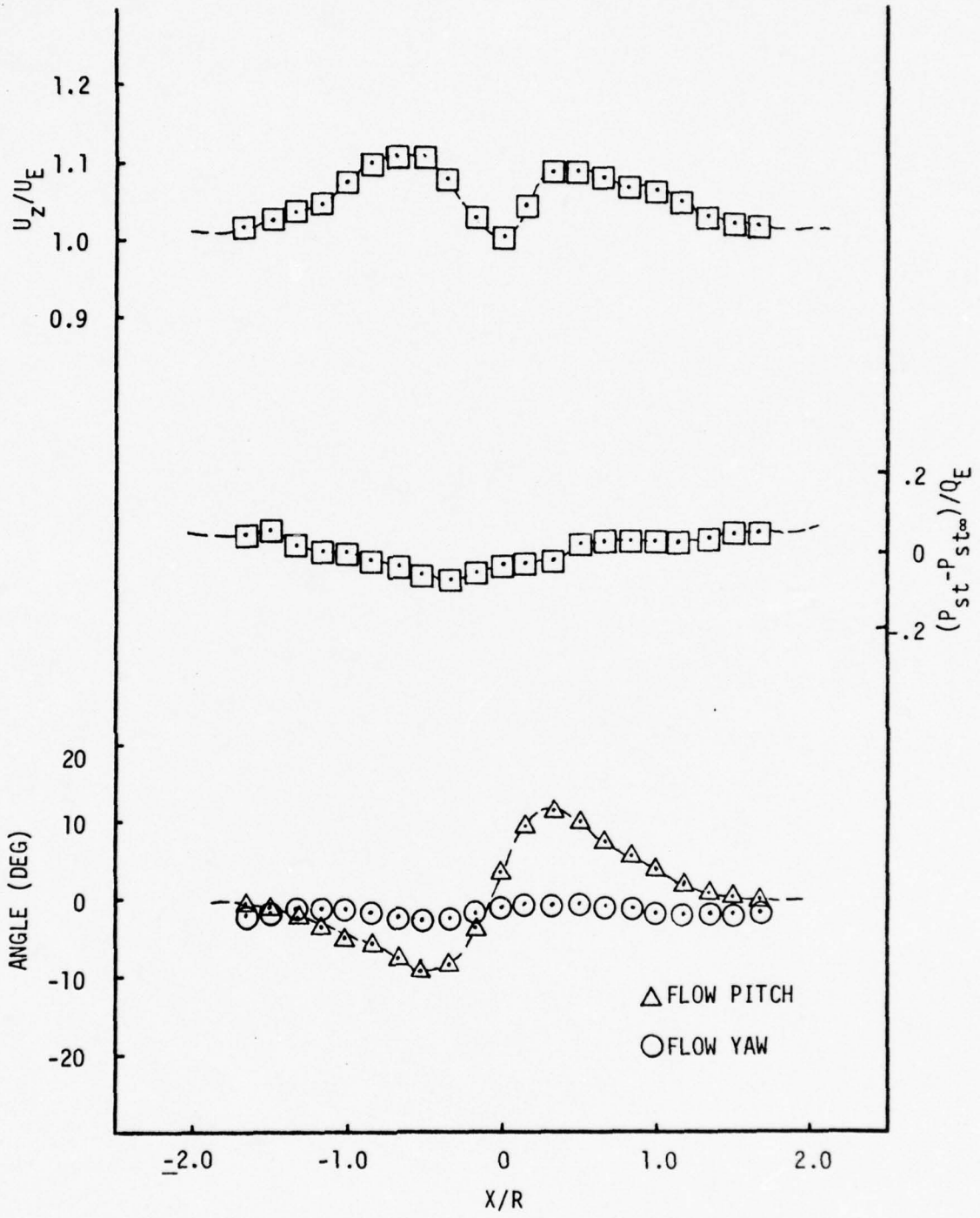

Fig. 32 MEAN AXIAL VELOCITY, FLOW ANGULARITY, AND STATIC PRESSURE HORIZONTAL PROFILE AT Z/D=10, Y/R=0, α_e=-2°

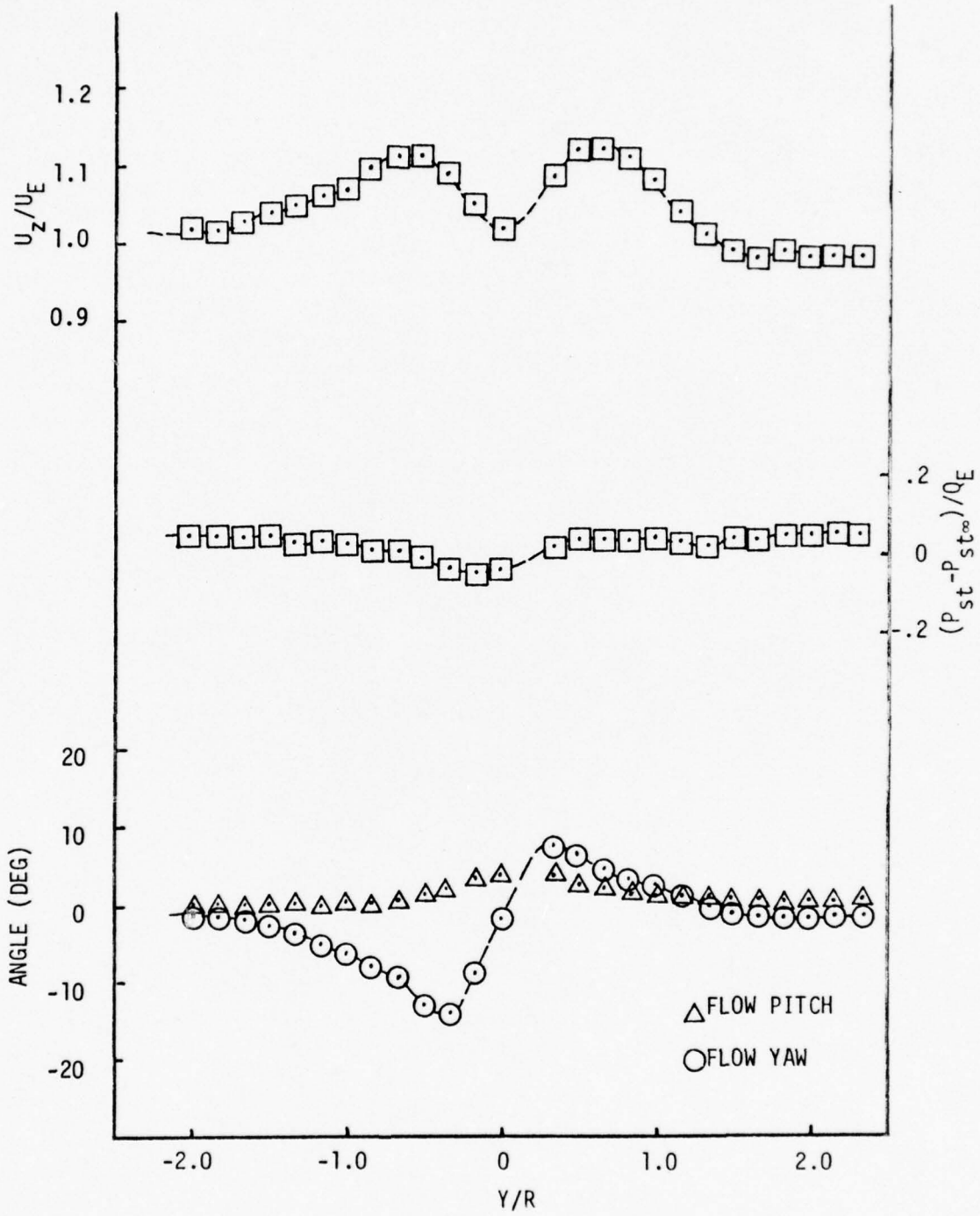

Fig. 33 MEAN AXIAL VELOCITY, FLOW ANGULARITY, AND STATIC PRESSURE VERTICAL PROFILE AT Z/D=10, X/R=0. α_e=-2°

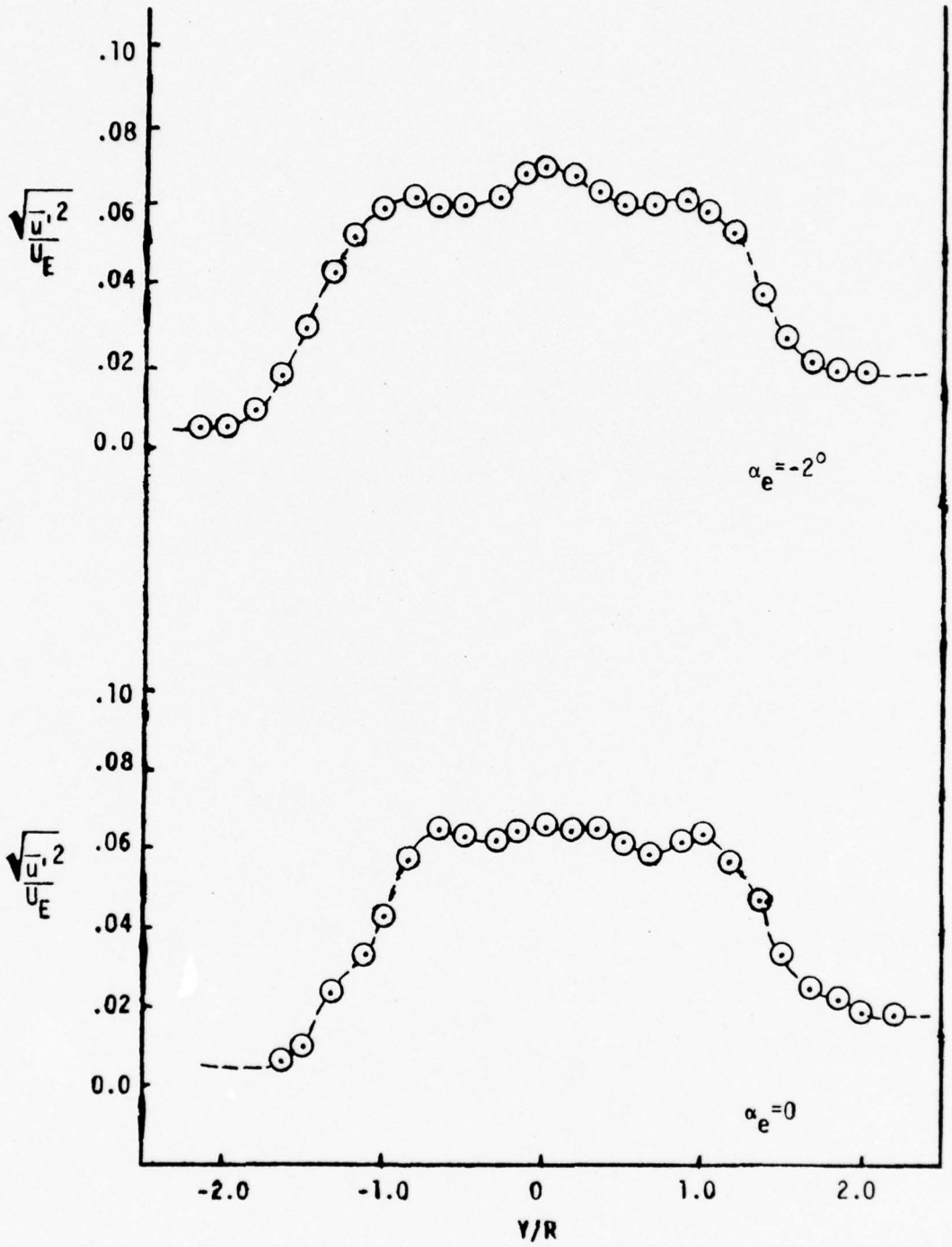

Fig. 34 AXIAL TURBULENCE INTENSITY VERTICAL PROFILE AT Z/D=10, X/R=0

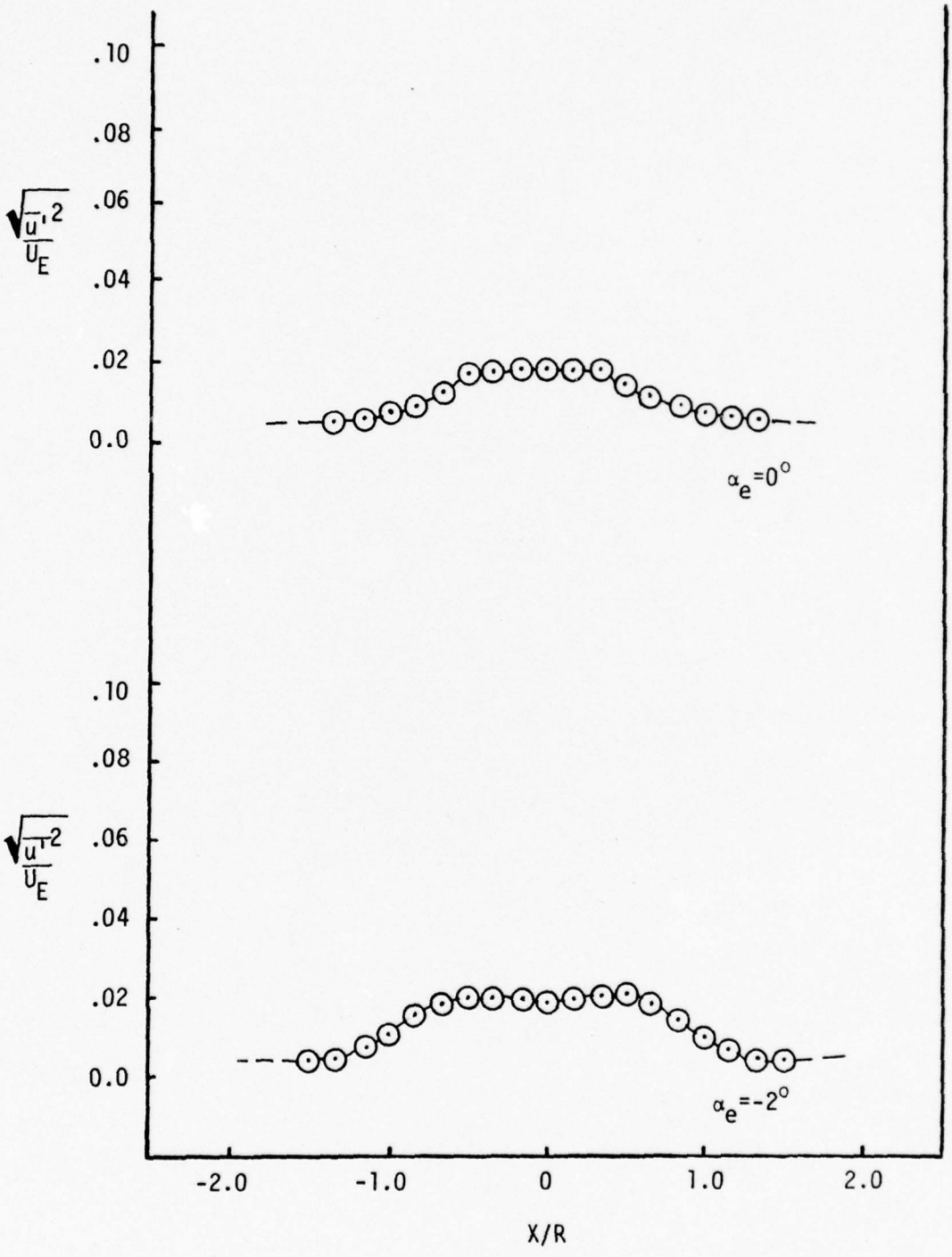

Fig. 35 AXIAL TURBULENCE INTENSITY IN SAIL WAKE AT Z/D=10, Y/R=1.67

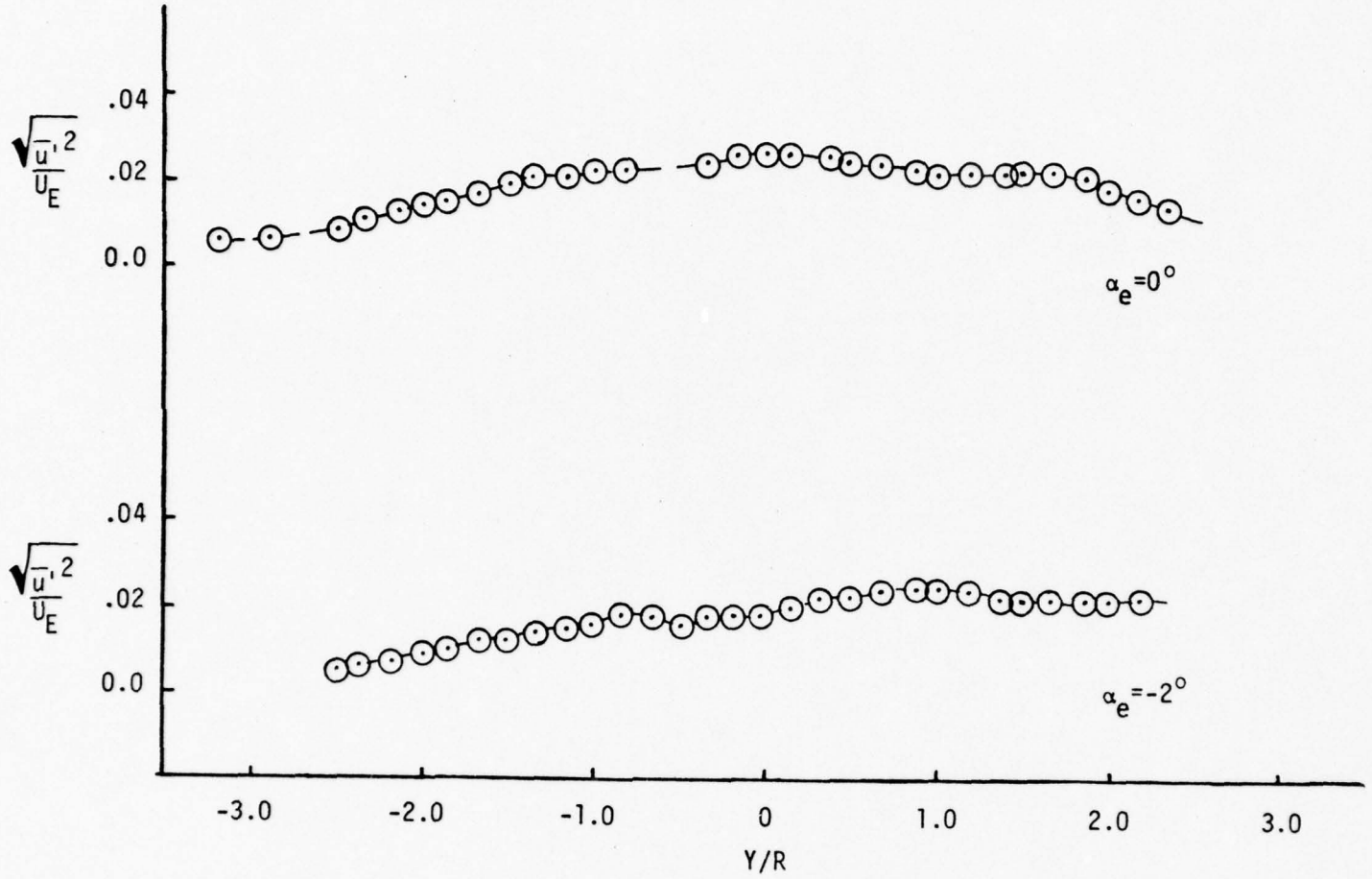

Fig. 36 AXIAL TURBULENCE INTENSITY VERTICAL PROFILE AT Z/D=40, X/R=0

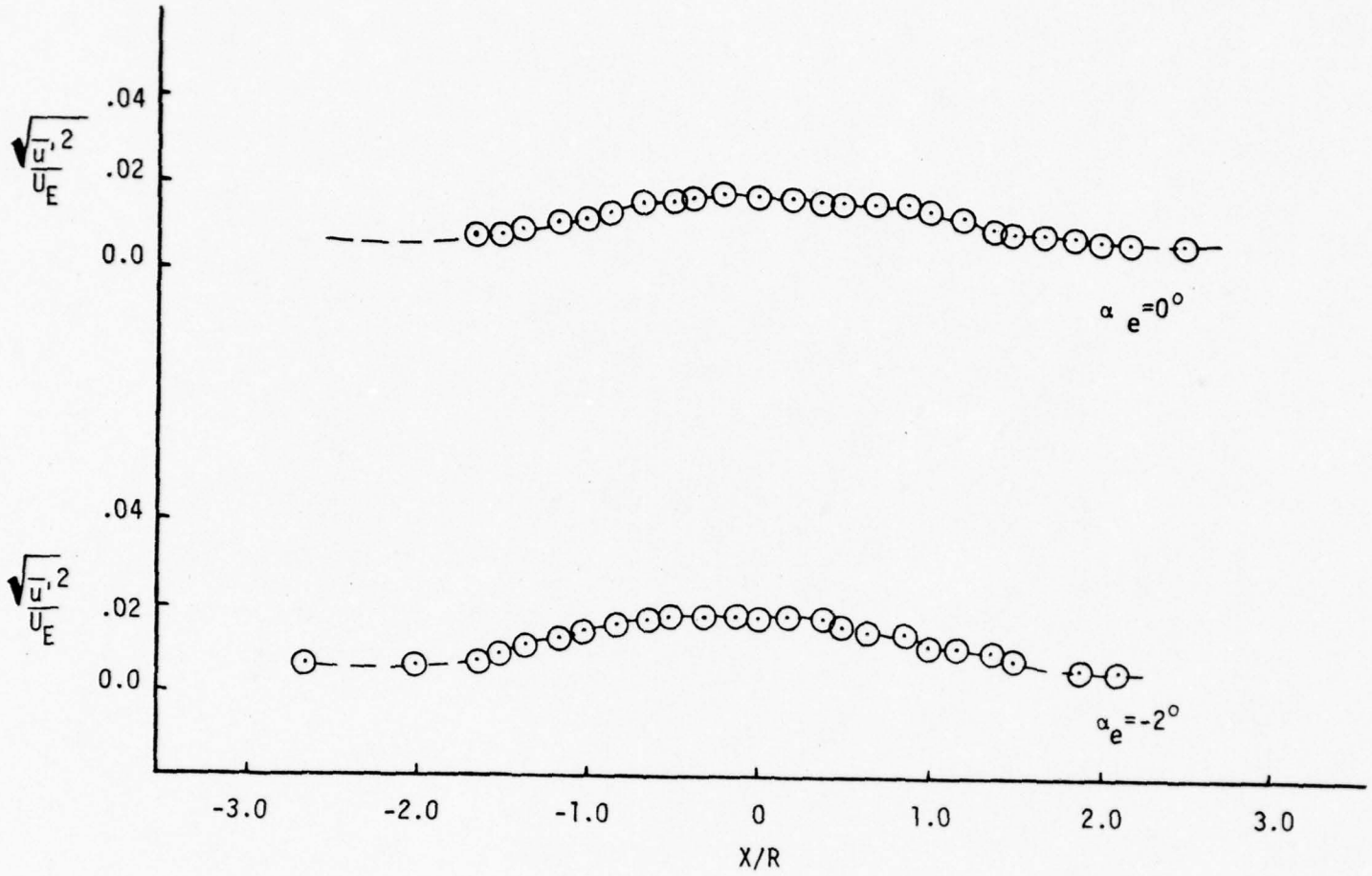

Fig. 37 AXIAL TURBULENCE INTENSITY IN SAIL WAKE AT Z/D=40, Y/R=2.33

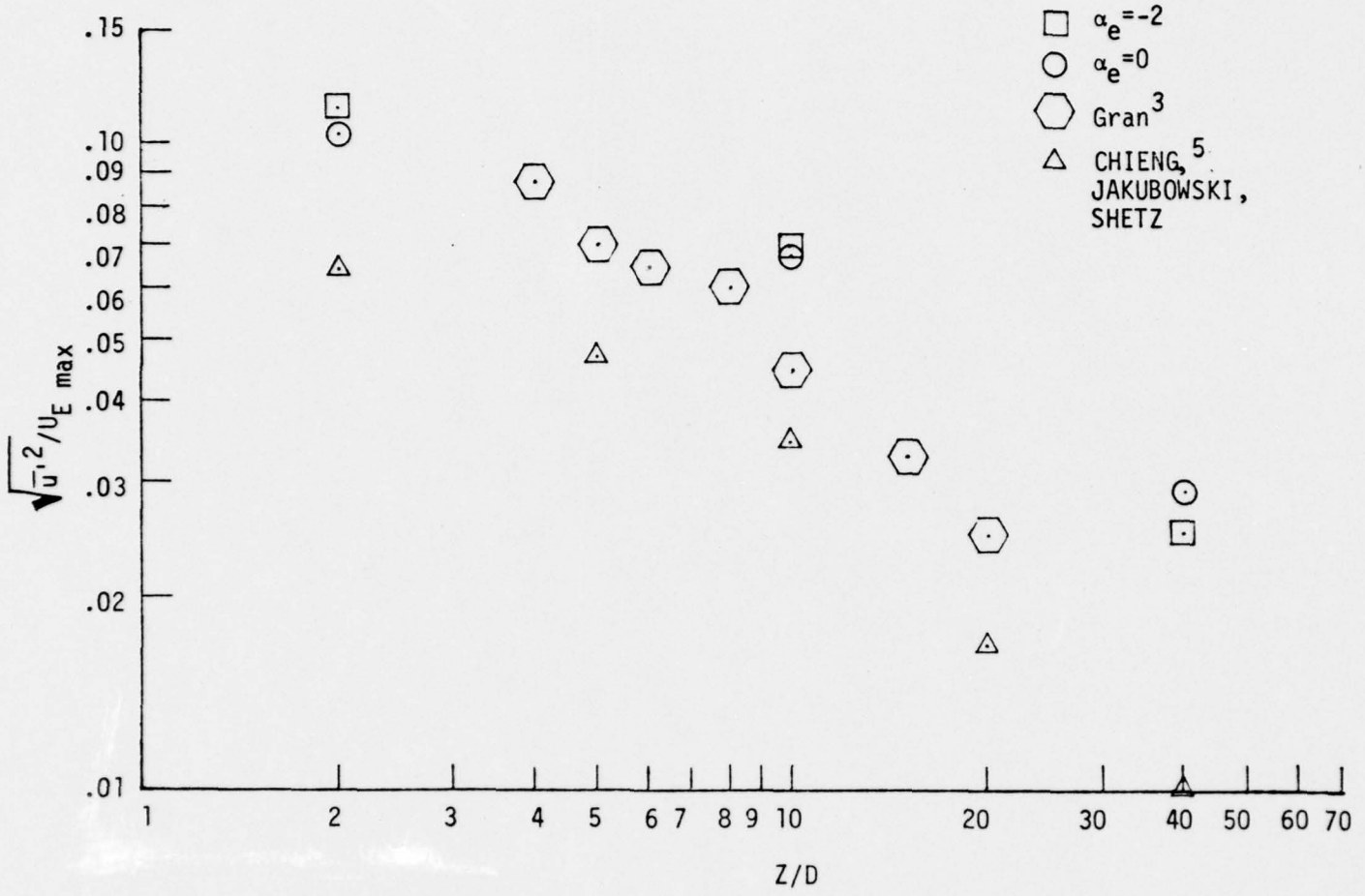

Fig. 38 MAXIMUM AXIAL TURBULENCE INTENSITY VS Z/D

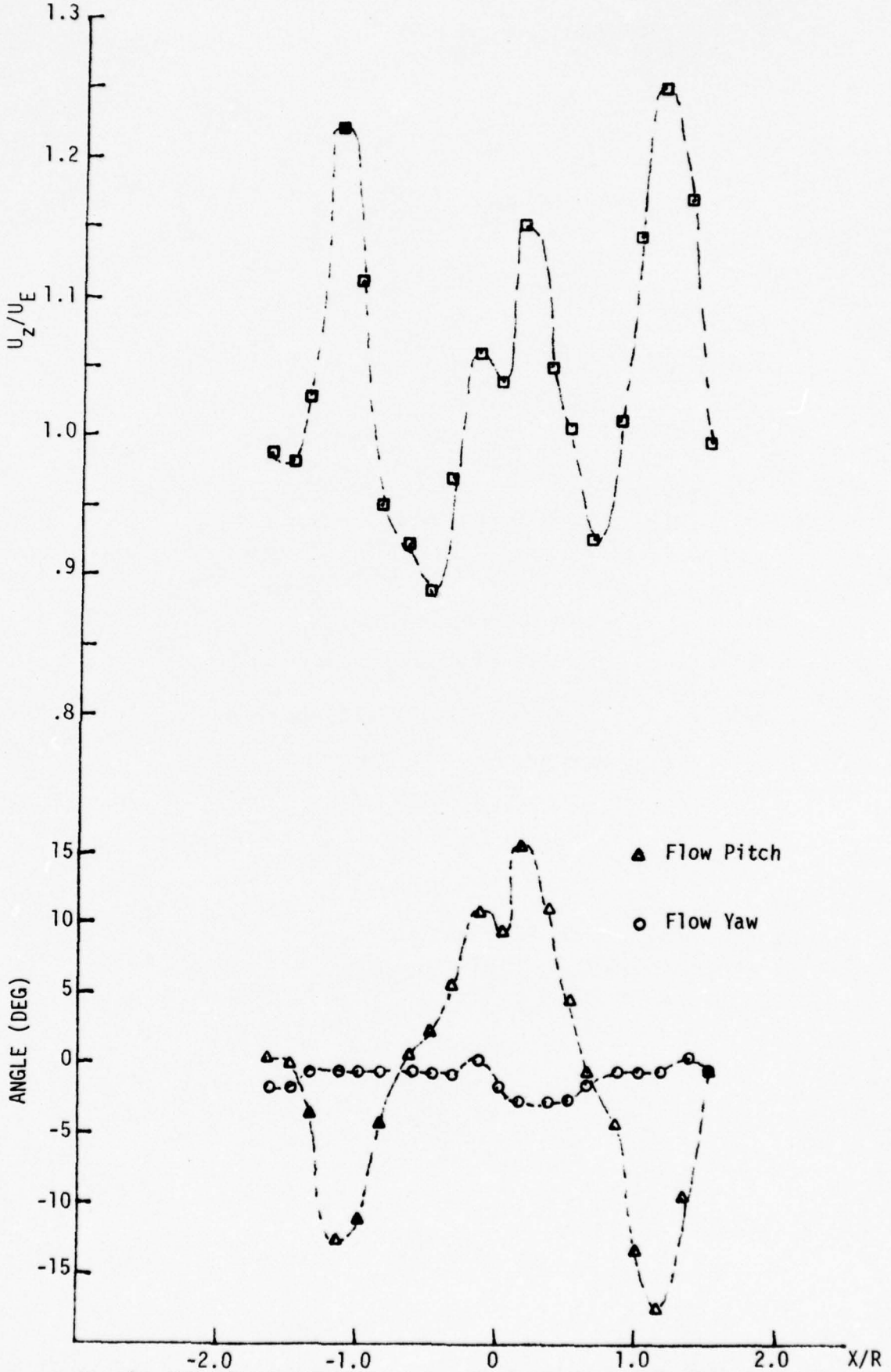

Fig. 39 MEAN AXIAL VELOCITY AND FLOW ANGULARITY, HORIZONTAL PROFILE AT Z/D=2, Y/R=0; DUAL PROPELLER MODEL

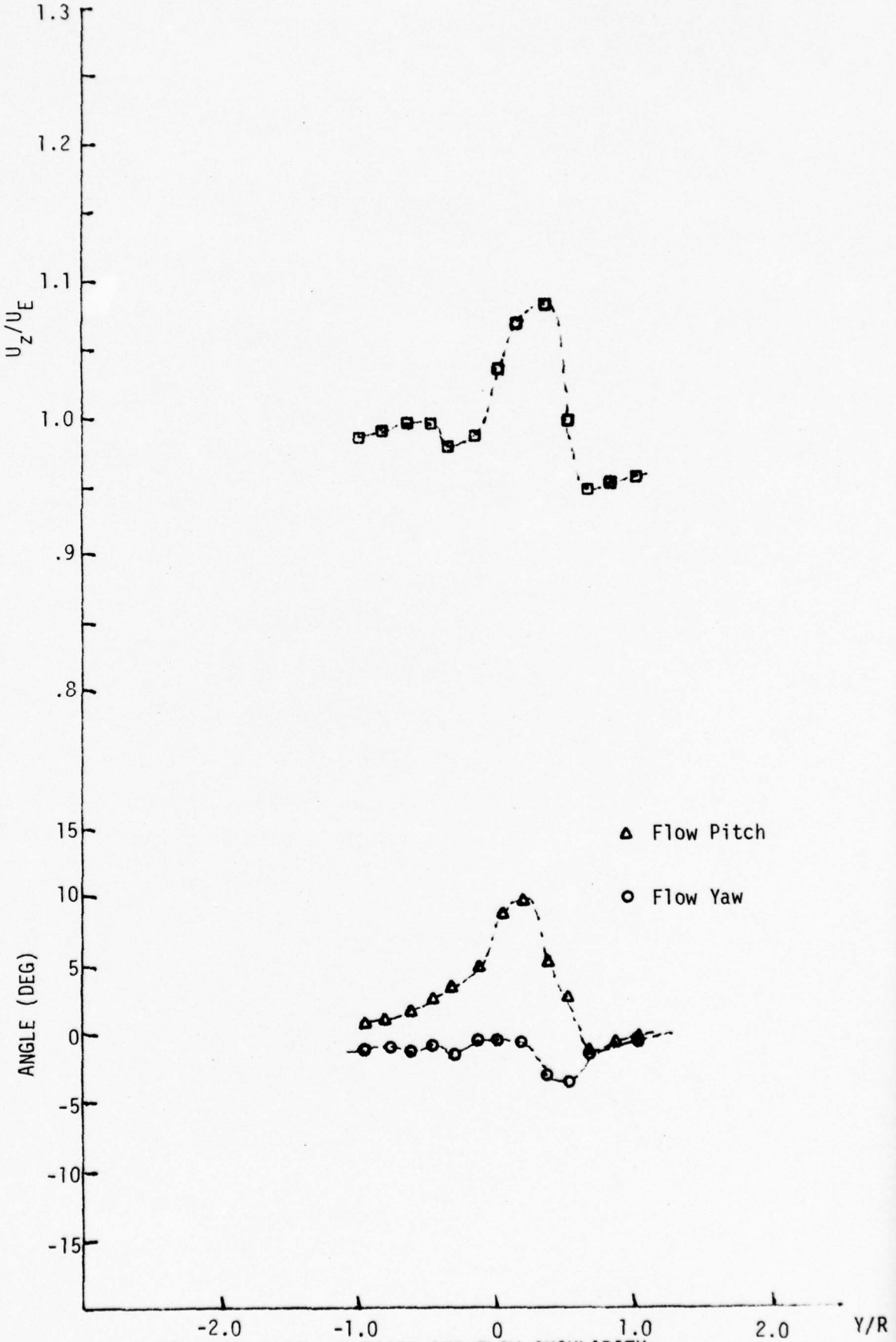

Fig. 40 MEAN AXIAL VELOCITY AND FLOW ANGULARITY; VERTICAL PROFILE AT Z/D=2, X/D=0 DUAL PROPELLER MODEL

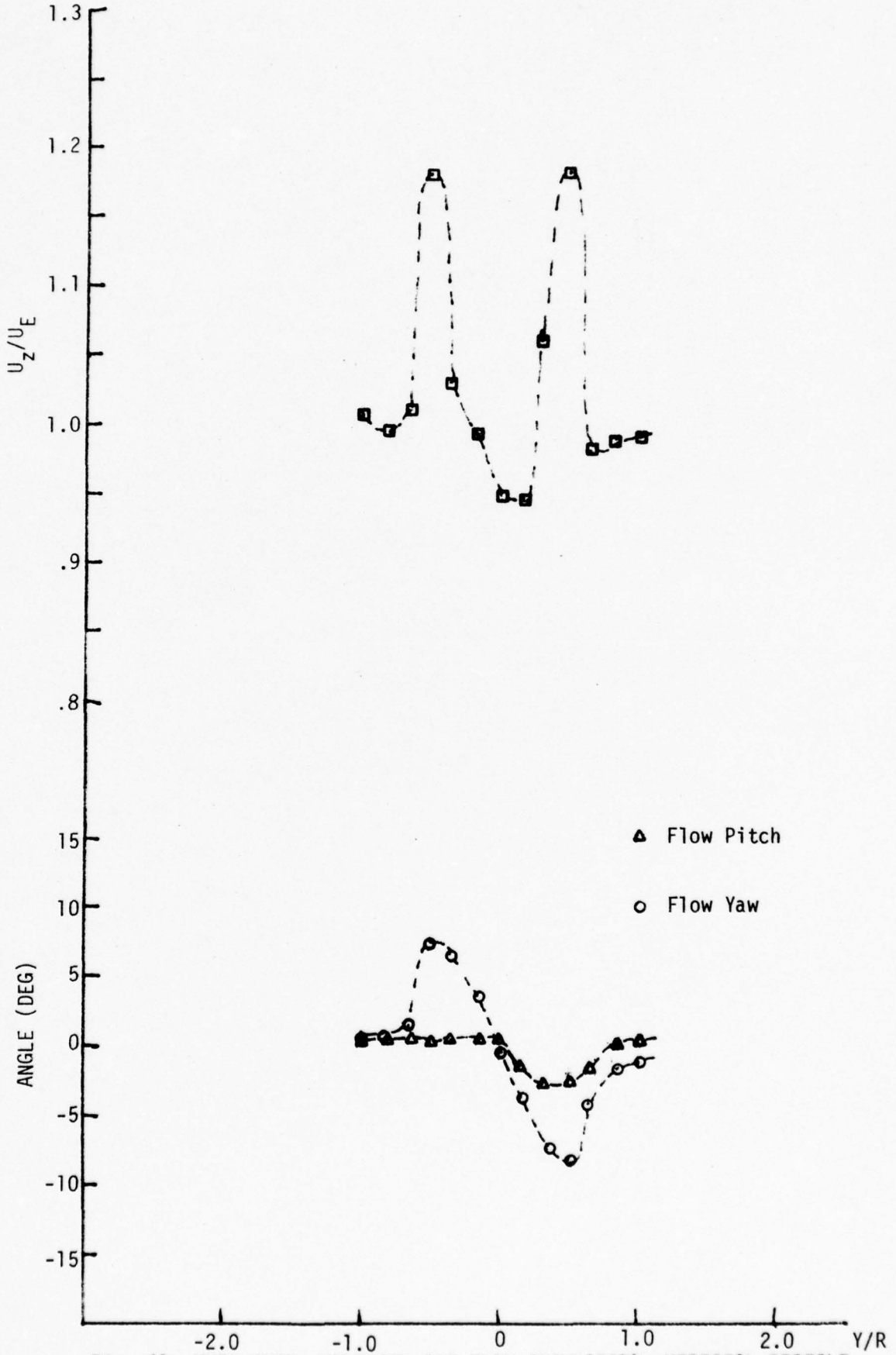

Fig. 41 MEAN AXIAL VELOCITY AND FLOW ANGULARITY, VERTICAL PROFILE AT Z/D=2, X/D=2; DUAL PROPELLER MODEL

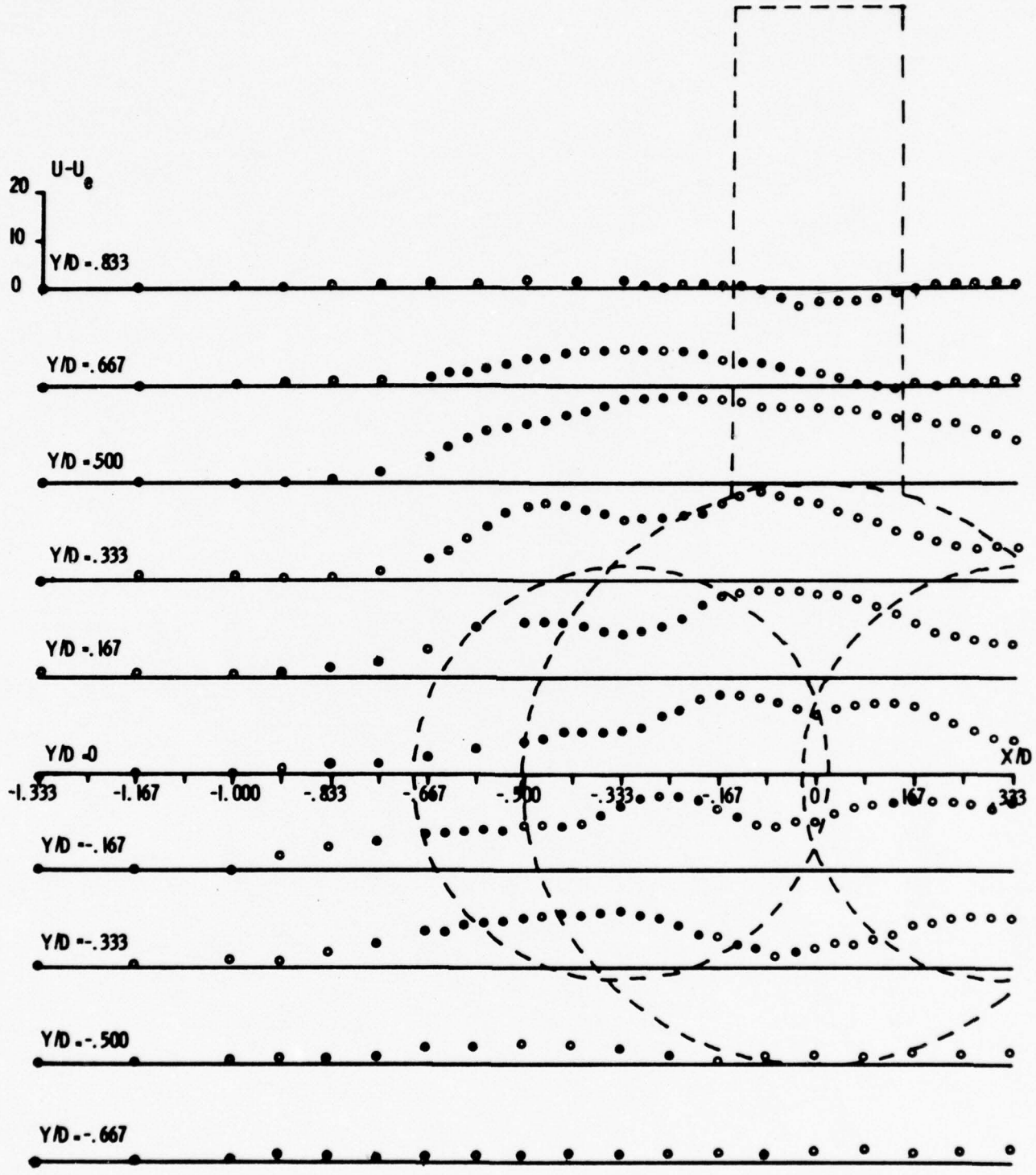

FIG. 42 AXIAL VELOCITY DISTRIBUTIONS FOR THE DUAL PROPELLER MODEL AT Z/D = 10

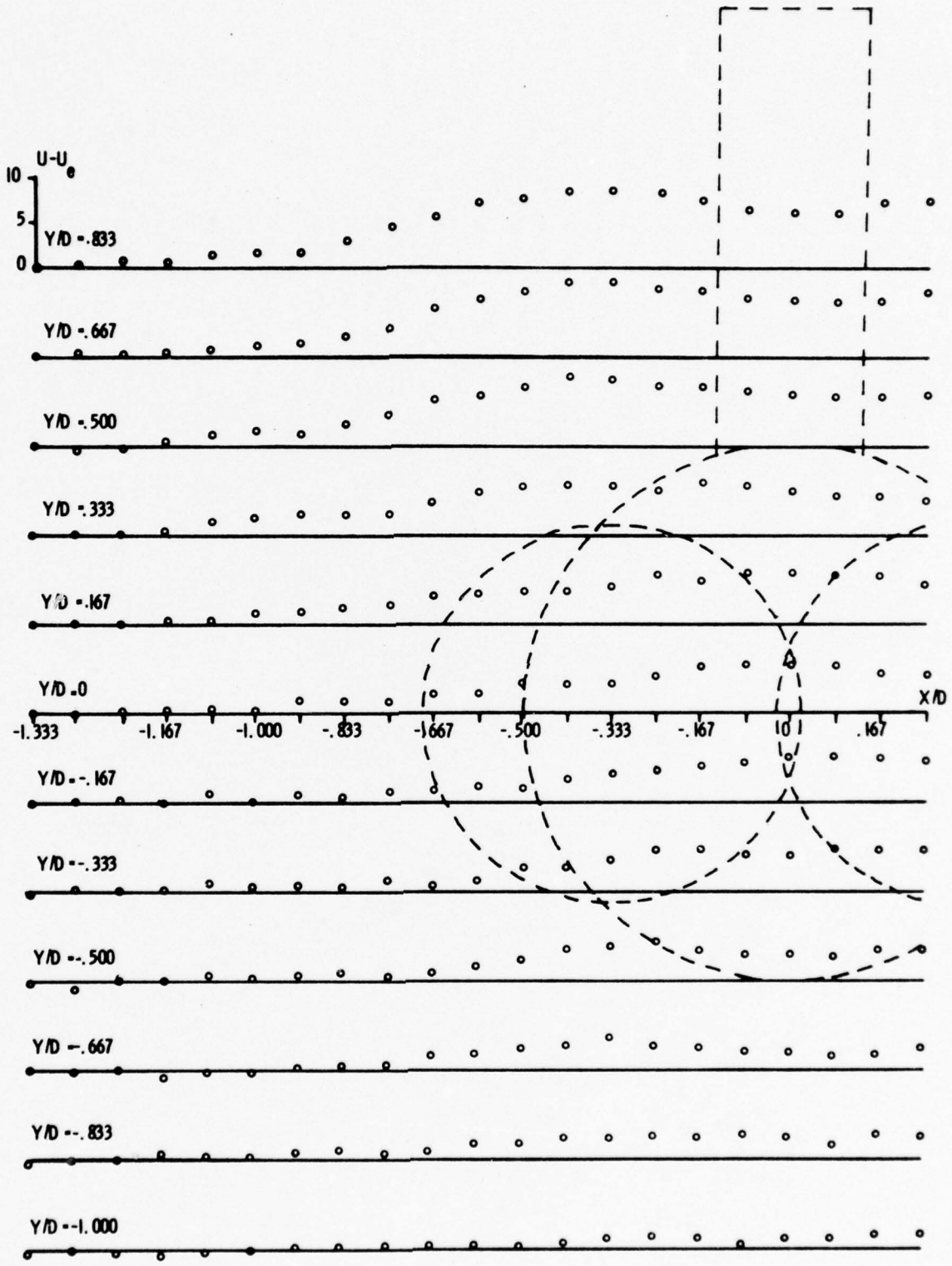

FIG. 43 AXIAL VELOCITY DISTRIBUTIONS FOR THE DUAL PROPELLER MODEL AT Z/D =40

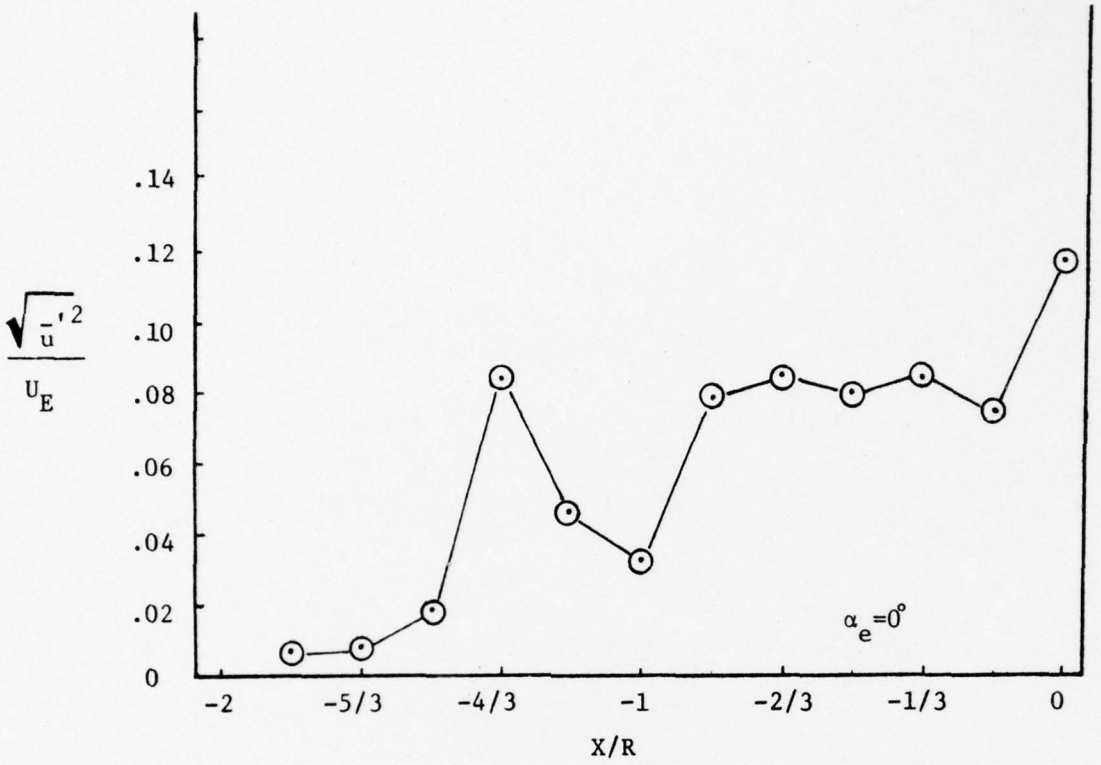

Fig. AXIAL TURBULENCE INTENSITY HORIZONTAL PROFILE AT Z/D= 2 , X/R=0

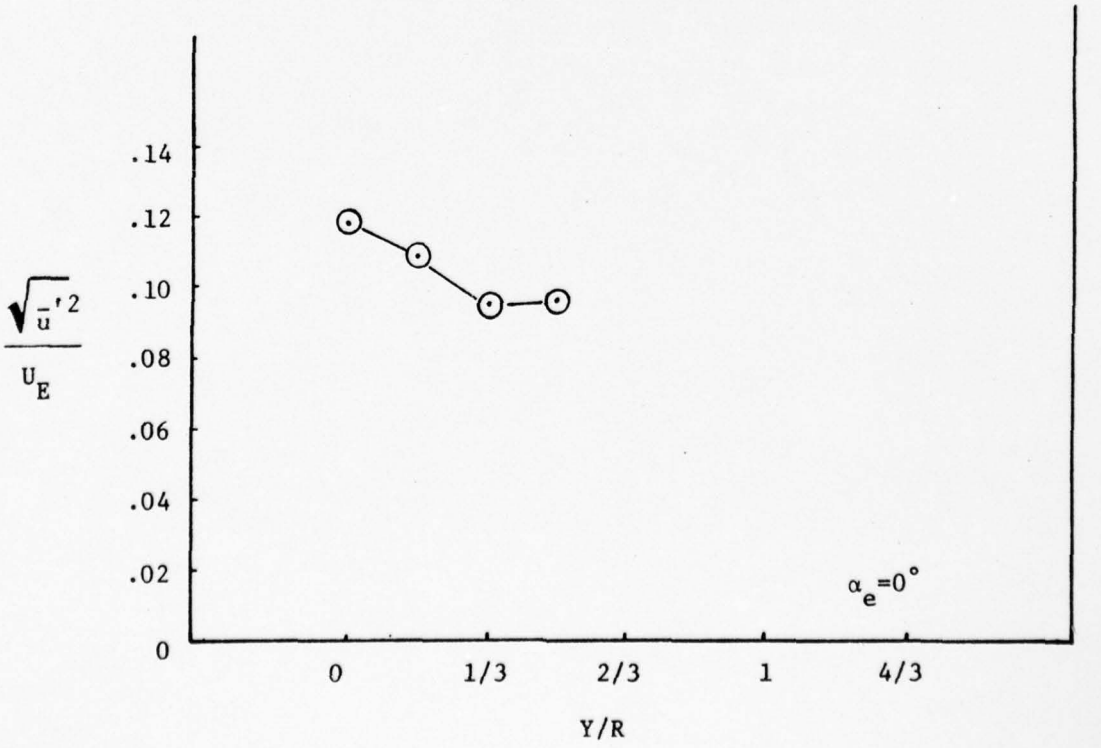

Fig.44 AXIAL TURBULENCE INTENSITY VERTICAL PROFILE AT Z/D= 2, X/R=0

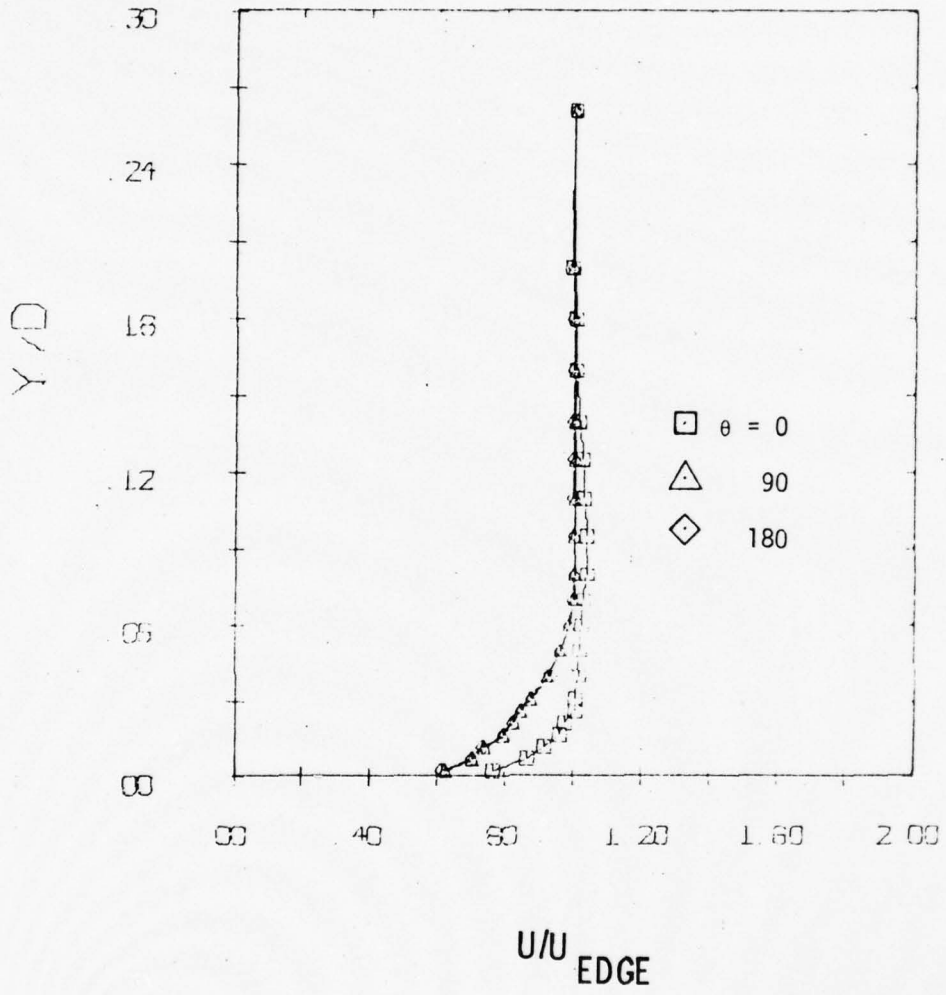

Figure 45 Boundary Layer Velocity Profiles for X/D = 6

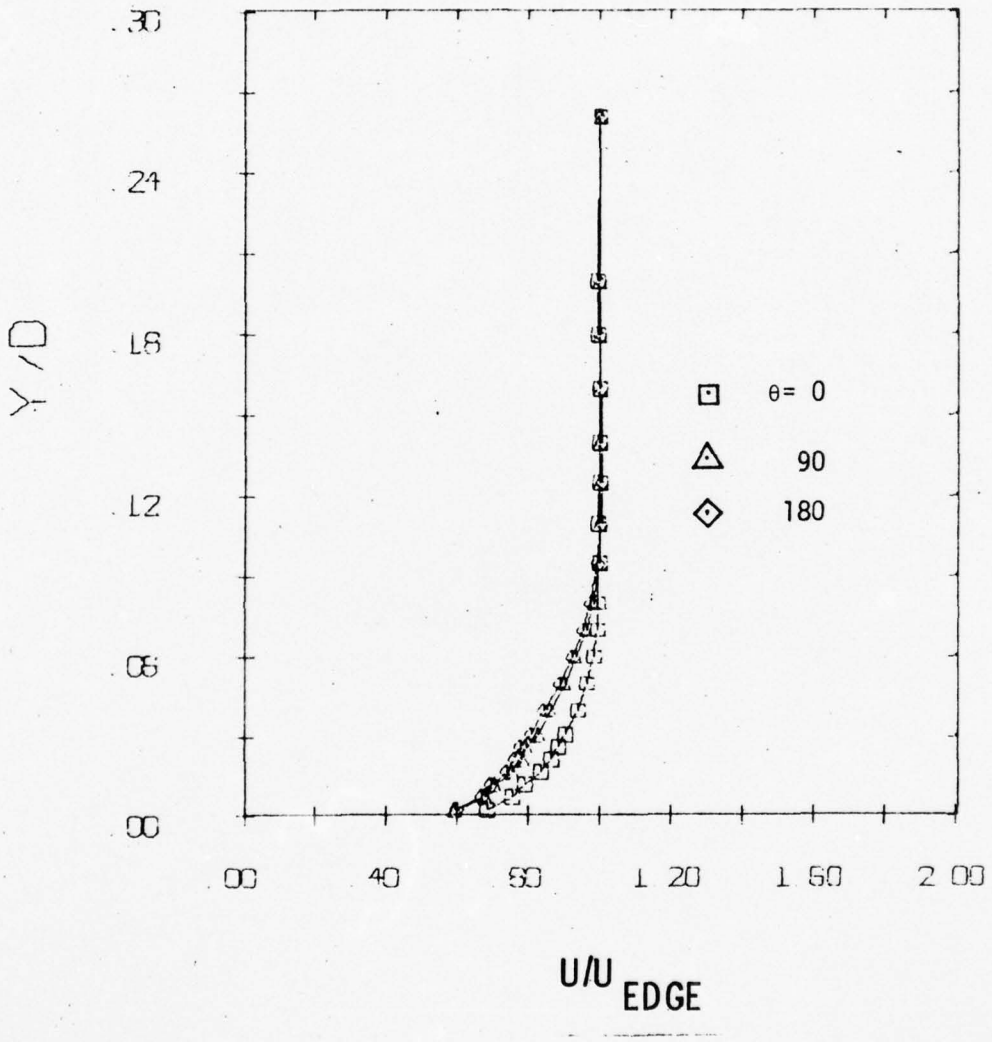

Figure 46 Boundary Layer Velocity Profiles for X/D = 8

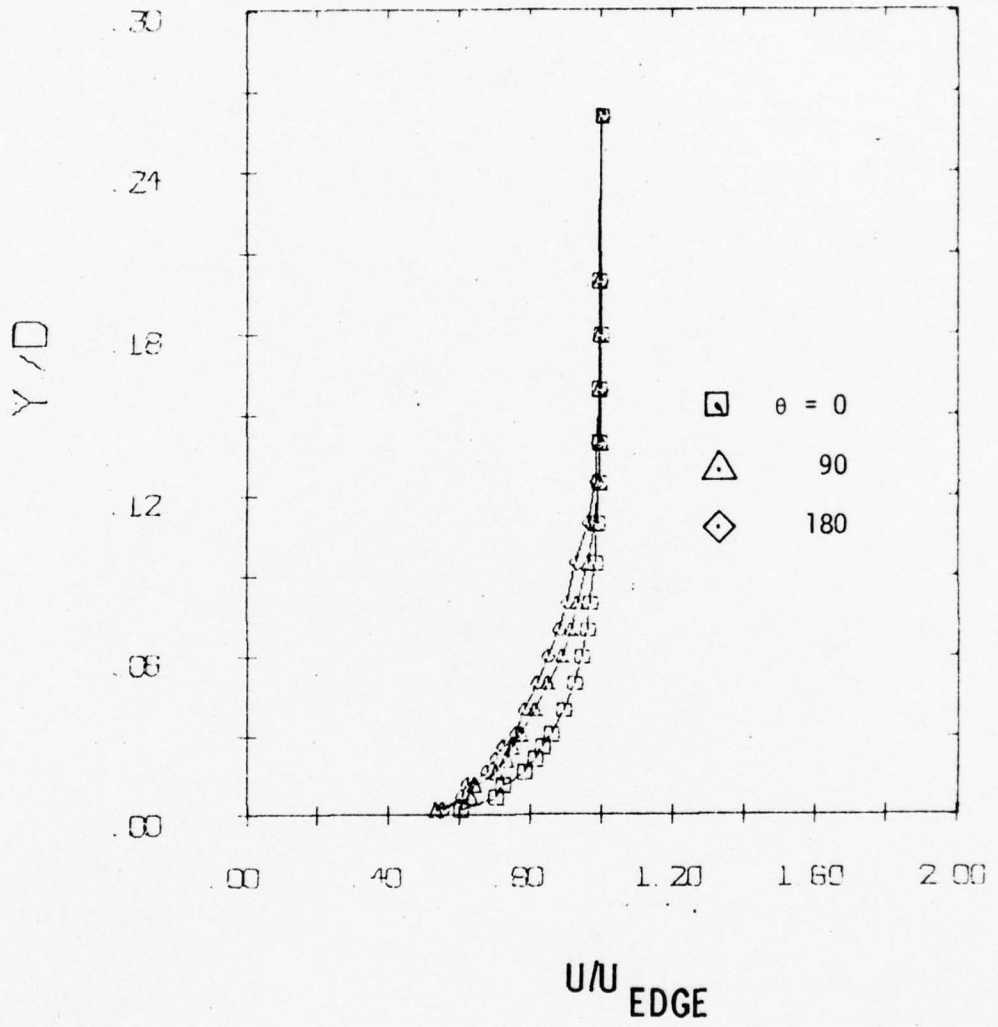

Figure 47 Boundary Layer Velocity Profiles for X/D = 10

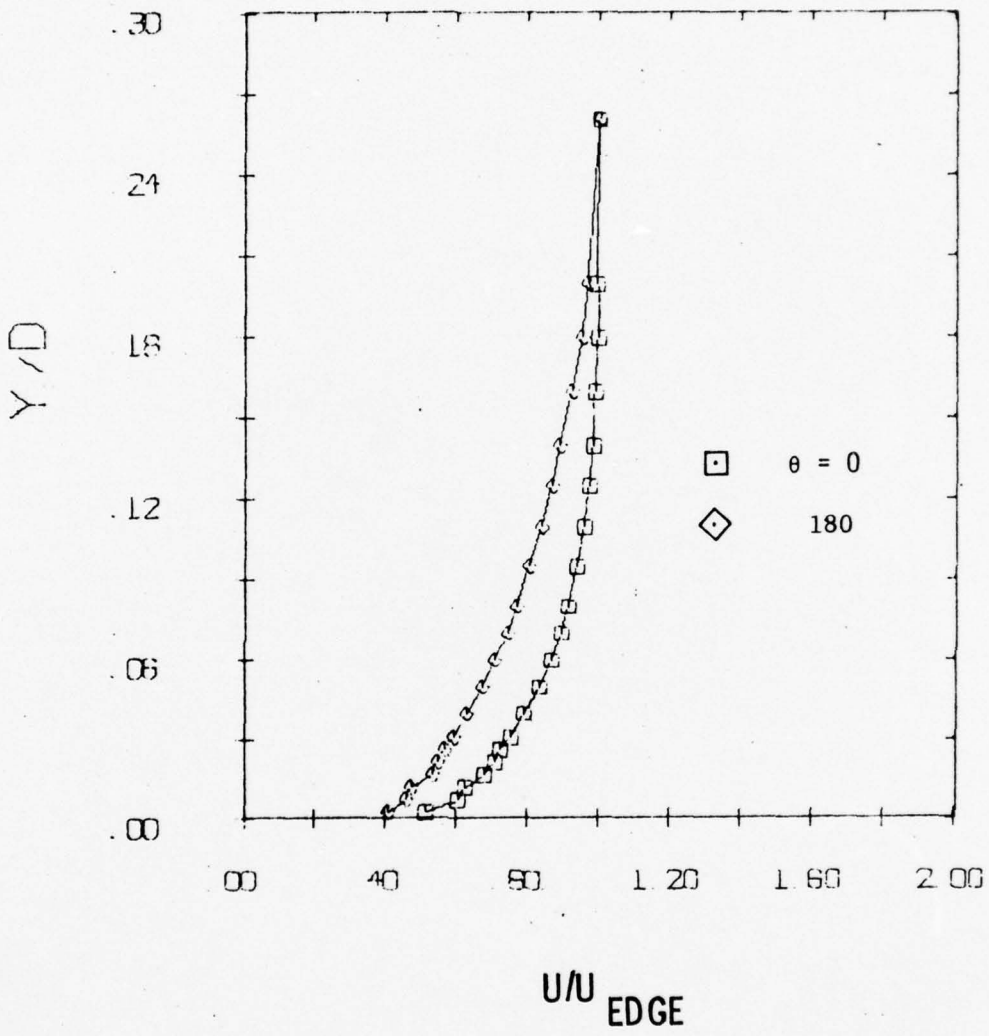

Figure 48 Boundary Layer Velocity Profiles for X/D = 11.17

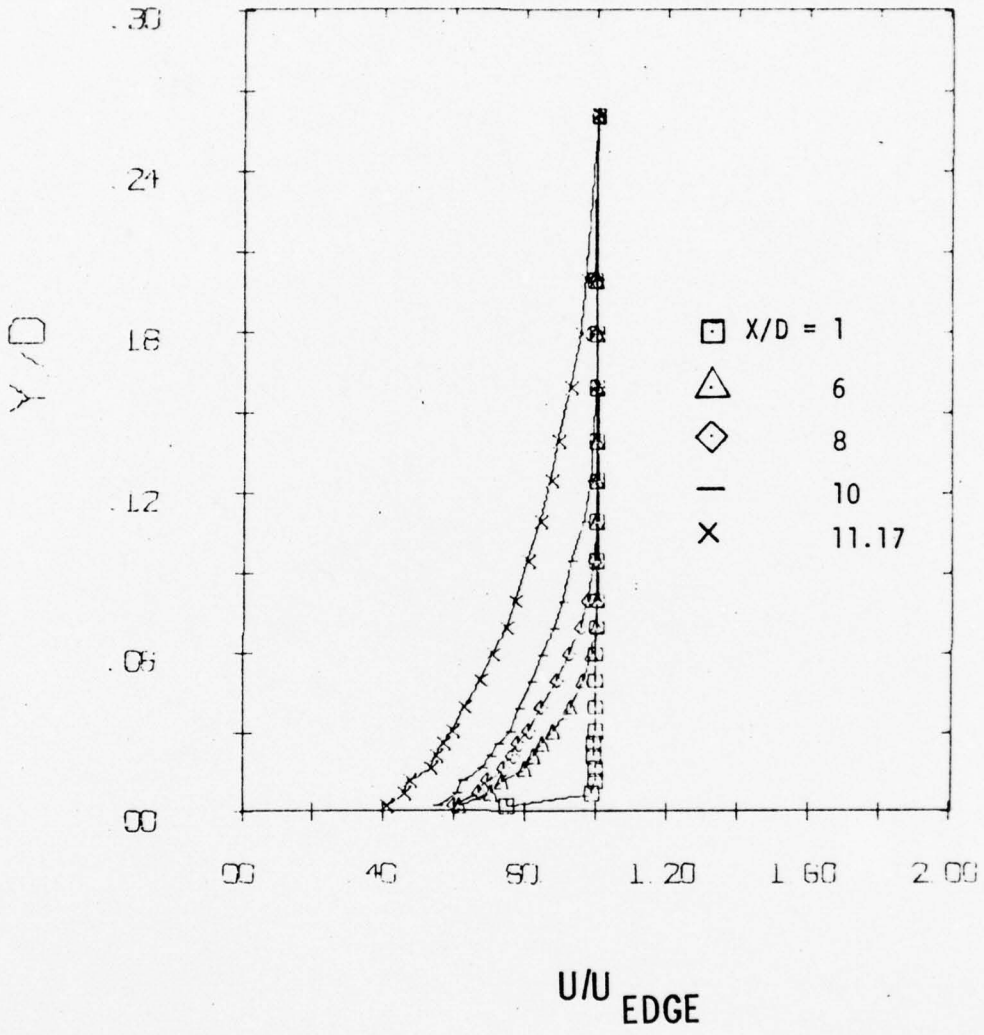

Figure 49 Boundary Layer Velocity Profiles for $\theta = 180^{o}$

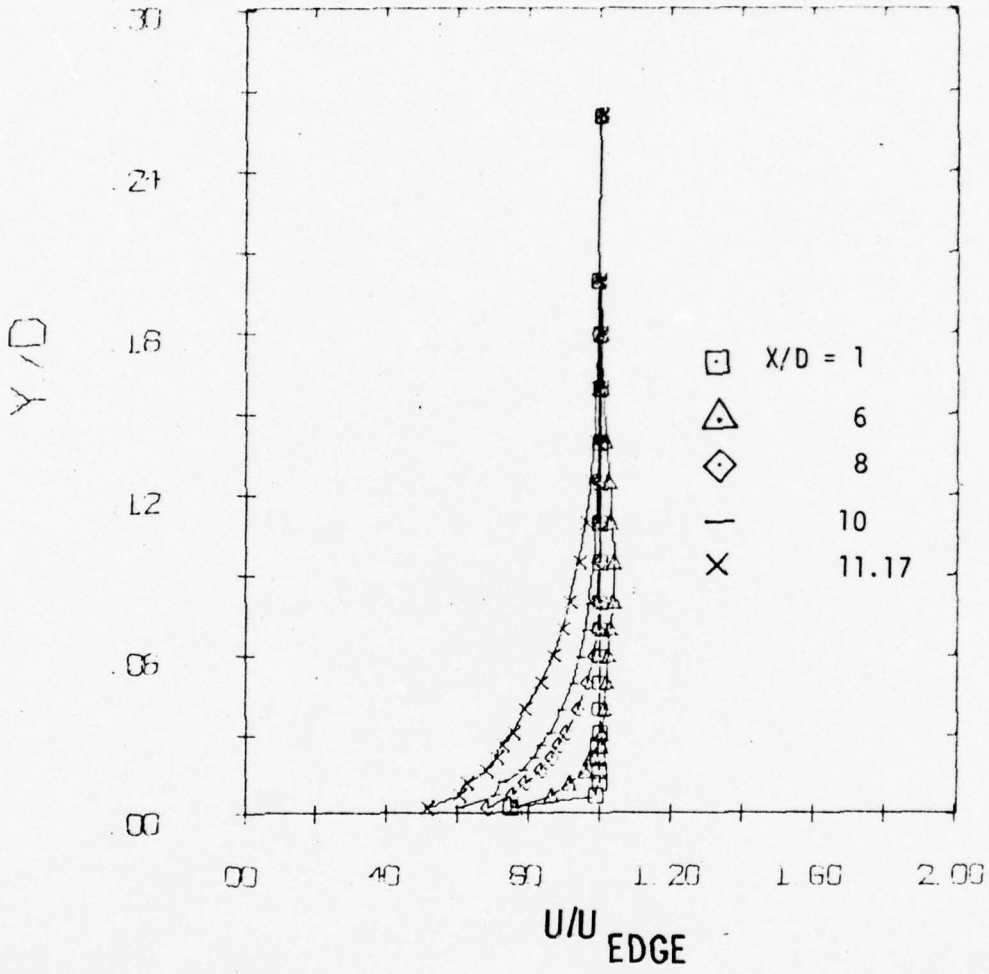

Figure 50 Boundary Layer Velocity Profiles for $\theta = 0^{o}$

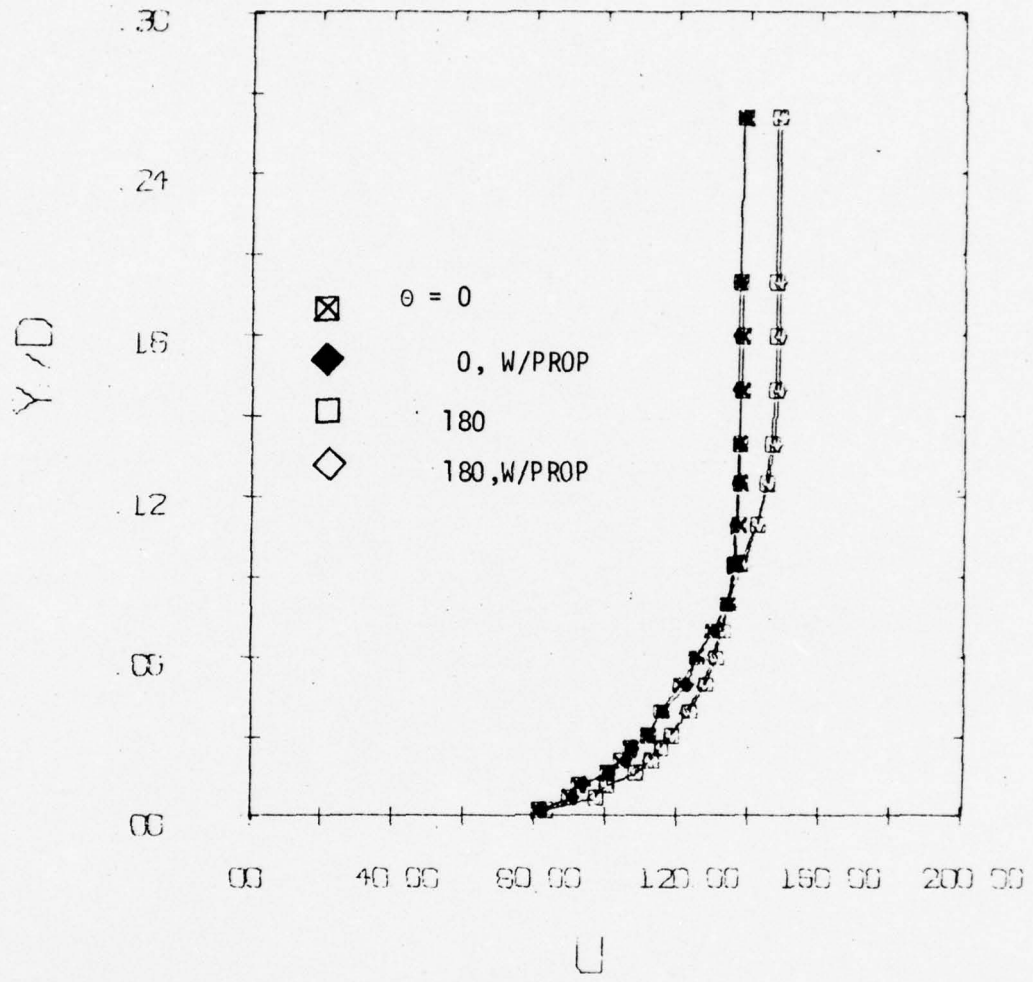

Figure 51 Boundary Layer Velocity Profiles for X/D = 10

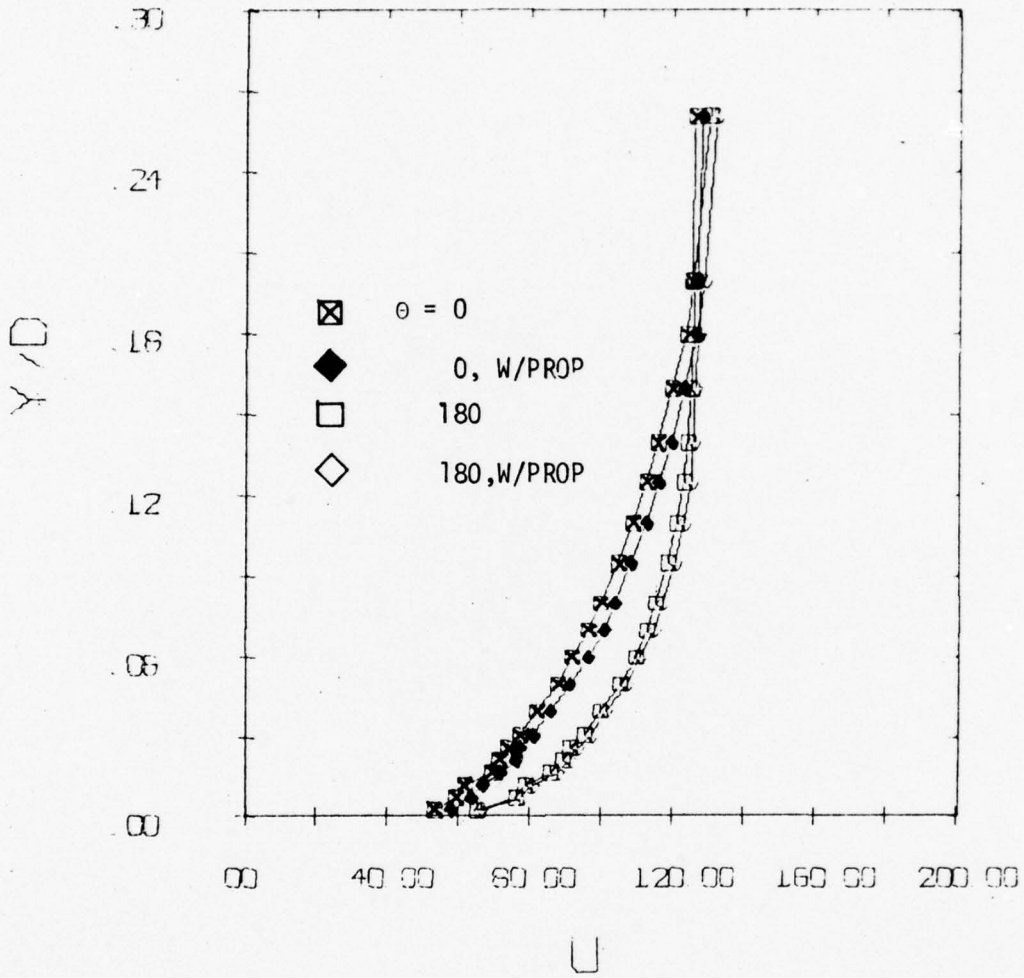

Figure 52 Boundary Layer Velocity Profiles for X/D = 11.17

APPENDIX A

TABULATED DATA FOR WAKE SURVEYS

WITH SINGLE PROPELLER MODEL

TABLE B-1

Profiles for Q = 5.0 in H_2O, Z/D = 2, $\alpha_e = 0°$

X/R	Y/R	Flow Pitch (DEG)	Flow Yaw (DEG)	U_z/U_E	V_{Total} (fps)	$P_{st}-P_{st\infty}$ (psf)	$\sqrt{\overline{u'^2}}/U_E$
1.33	0.0	.44	-.86	1.03	146.0	1.77	.006
1.00	0.0	.64	-.96	1.03	146.2	1.72	.027
.83	0.0	3.7	-.86	1.02	146.3	1.05	.074
.67	0.0	19.7	.04	1.18	178.1	-1.17	.073
.50	0.0	23.2	1.4	1.28	198.1	-1.97	.062
.33	0.0	23.4	2.8	1.20	186.2	-3.35	.053
.17	0.0	16.6	3.5	1.00	148.7	-4.03	.090
0.0	0.0	2.4	.74	.89	126.5	-2.37	.086
-.17	0.0	-1.4	.39	.90	128.8	-2.35	
-.33	0.0	-6.4	1.5	.95	135.9	-3.21	.087
-.50	0.0	-23.4	2.0	1.13	175.8	-5.75	.097
-.67	0.0	-23.6	1.6	1.27	197.5	-4.80	.061
-.83	0.0	-19.9	1.4	1.20	182.9	-3.12	.063
-1.0	0.0	-4.0	-.86	1.03	147.5	.1738	.088
-1.17	0.0	0.0	-.86	1.03	146.7	1.75	.055
-1.33	0.0	.25	-.86	1.03	146.9	1.99	.017
-.83	1.67	.25	-.86	1.02	146.1	1.95	.008
-.67	1.67	.25	-.86	1.02	146.1	1.95	.013
-.50	1.67	.25	-.86	1.02	145.5	1.93	.022
-.33	1.67	.39	-.96	1.00	142.6	2.01	.027
-.17	1.67	.25	-.86	.98	140.5	2.12	.026
0.0	1.67	.34	-.86	.98	140.6	2.13	.027
.17	1.67	.30	-.91	1.00	143.0	2.18	.023
.33	1.67	.25	-.86	1.02	145.9	2.17	.014
.50	1.67	.34	-.86	1.02	146.3	2.18	.009

TABLE B-1 (Continued)

X/R	Y/R	Flow Pitch (DEG)	Flow Yaw (DEG)	U_z/U_E	V_{Total} (fps)	$P_{st}-P_{st\infty}$ (psf)	$\sqrt{\overline{u'^2}}/U_E$
0.0	2.0	.49	-.91	1.00	142.0	2.0	.027
0.0	1.83	.44	-.91	1.00	142.0	1.95	.027
0.0	1.67	.54	-.91	.99	140.6	1.94	.027
0.0	1.50	.49	-.91	.99	140.5	1.98	.027
0.0	1.33	.49	-.91	.99	140.8	1.99	.027
0.0	1.17	.49	-.86	.99	140.8	2.01	.030
0.0	1.00	.64	-.61	1.00	142.2	1.35	.058
0.0	.83	1.63	2.6	1.02	146.0	1.20	.093
0.0	.67	4.4	14.9	1.20	178.5	.76	.073
0.0	.50	4.9	19.0	1.27	192.4	.03	.060
0.0	.33	6.3	18.7	1.18	179.7	-1.06	.080
0.0	.17	5.9	10.0	.97	141.6	-1.74	
0.0	0.0	2.4	.54	.88	125.7	-2.39	.085
0.0	-.17	2.2	-2.9	.88	125.9	-2.08	.100
0.0	-.33	5.1	-14.7	.97	144.7	-4.39	.091
0.0	-.50	4.4	-26.5	1.19	191.0	-5.6	.054
0.0	-.67	2.5	-25.4	1.28	203.0	-2.6	.063
0.0	-.83	1.4	-20.5	1.17	178.5	-0.75	.068
0.0	-1.0	1.0	-4.1	1.02	146.6	1.22	.077
0.0	-1.17	.30	-.86	1.03	147.2	1.75	.027
0.0	-1.33	.30	-.86	1.03	147.4	1.76	.009

TABLE B-2

Profiles for Q = 5.0 in H_2O, Z/D = 2, α_e = -2°

X/R	Y/R	Flow Pitch (DEG)	Flow Yaw (DEG)	U_z/U_E	V_{Total} (fps)	$P_{st}-P_{st\infty}$ (psf)	$\sqrt{\overline{u'^2}}/U_E$
1.67	0.0	.10	-.96	1.02	148.1	1.50	.006
1.33	0.0	-.25	-1.0	1.02	148.3	1.52	.007
1.17	0.0	.20	-1.1	1.01	147.4	1.34	.016
1.00	0.0	5.4	-1.0	1.02	149.7	.39	.048
.83	0.0	17.1	-1.2	1.18	179.5	-.93	.092
.67	0.0	20.5	-.26	1.25	193.6	-1.06	.088
.50	0.0	22.5	.99	1.20	189.7	-2.55	.069
.33	0.0	21.1	1.7	1.04	162.3	-3.76	.050
.17	0.0	3.2	-.56	.84	122.3	-2.61	.067
0.0	0.0	-2.2	-1.0	.83	121.9	-2.33	.098
-.17	0.0	-4.7	-.71	.92	134.6	-2.96	.083
-.33	0.0	-20.5	-.21	1.06	165.4	-6.01	.091
-.50	0.0	-23.3	.09	1.24	196.7	-5.30	.113
-.67	0.0	-20.5	.64	1.24	193.3	-3.66	.062
-.83	0.0	-7.0	-.76	1.04	153.4	-1.10	.063
-1.00	0.0	-1.0	-1.2	1.01	145.9	1.52	.088
-1.17	0.0	-.44	-1.1	1.02	147.0	1.62	.059
-1.33	0.0	-.34	-.86	1.02	146.9	1.71	.020
-1.67	0.0	-.34	-.86	1.02	146.9	1.71	.006
-.83	0.0	-.15	-.91	1.02	147.0	1.69	.009
-.67	1.67	0.0	-1.06	1.01	146.4	1.64	.014
-.50	1.67	.10	-.96	1.01	146.0	1.62	.021
-.33	1.67	.25	-1.1	1.00	144.4	1.59	.025
-.17	1.67	.30	-1.1	.99	142.4	1.56	.025
0.0	1.67	.39	-1.0	.98	141.8	1.59	.026

TABLE B-2 (Continued)

X/R	Y/R	Flow Pitch (DEG)	Flow Yaw (DEG)	U_z/U_E	V_{Total} (fps)	$P_{st}-P_{st\infty}$ (psf)	$\sqrt{\overline{u'^2}}/U_E$
.17	1.67	.39	-.91	.98	142.1	1.55	.025
.33	1.67	.39	-.86	.99	143.8	1.59	.021
.50	1.67	.25	-.91	1.00	145.3	1.53	.016
.67	1.67	.20	-.96	1.01	146.3	1.54	.011
.83	1.67	.15	-1.1	1.02	147.1	1.56	.008
0.0	1.50	.25	-.96	.98	141.7	1.56	.026
0.0	1.33	.25	-.76	.98	140.5	1.54	.030
0.0	1.17	.15	-.66	.97	139.4	1.54	.051
0.0	1.00	.15	-.11	.97	139.4	0.85	.103
0.0	.83	.74	6.4	1.04	151.0	0.56	.081
0.0	.67	1.5	16.7	1.25	188.8	0.22	.078
0.0	.50	1.3	18.1	1.20	182.1	-.94	.083
0.0	.33	2.5	16.5	1.04	157.0	-1.88	.113
0.0	.17	.20	4.9	.87	125.7	-1.94	.113
0.0	0.0	-1.0	-1.1	.82	118.1	-1.99	.098
0.0	-.17	-.54	-4.4	.85	123.6	-2.22	.109
0.0	-.33	.30	-21.2	1.00	155.3	-4.18	.056
0.0	-.50	-.05	-26.8	1.21	196.7	-3.69	.060
0.0	-.67	-.25	-24.7	1.26	200.5	-1.97	.071
0.0	-.83	-.34	-14.9	1.09	162.8	-.23	.090
0.0	-1.00	.54	-3.0	1.00	145.2	1.18	.029
0.0	-1.17	.49	-1.1	1.02	147.4	1.61	.008
0.0	-1.33	.30	-.96	1.02	147.7	1.67	.008

S Symmetric profiles

TABLE B-3

Profiles for Q = 5.0 in H_2O, Z/D = 10, α_e = 0°

X/R	Y/R	Flow Pitch (DEG)	Flow Yaw (DEG)	U_z/U_E	V_{Total} (fps)	$P_{st}-P_{st\infty}$ (psf)	$\sqrt{\overline{u'^2}}/U_E$
0.0	0.0	.94	-8.8	1.04	151.7	-.90	.065
0.0	.17	1.2	-3.1	.99	144.4	-.91	.066
0.0	.33	1.6	3.2	1.01	147.0	-.77	.064
0.0	.50	1.4	8.5	1.06	156.0	-.14	.061
0.0	.67	1.3	9.6	1.11	162.9	.41	.058
0.0	.83	1.0	7.8	1.12	165.3	.63	.061
0.0	1.00	.94	5.6	1.10	161.5	.76	.063
0.0	1.17	.59	3.9	1.07	156.7	.82	.058
0.0	1.33	.34	2.1	1.03	151.6	.92	.046
0.0	1.50	.30	.54	1.00	147.2	1.02	.034
0.0	1.67	.25	-.01	.99	141.8	.58	.025
0.0	1.83	.25	-.61	.98	141.0	1.09	.022
0.0	2.00	.25	-.66	.98	141.0	1.06	.019
0.0	2.17	.25	-.76	.98	141.0	1.11	.018
0.0	-.17	.89	-12.6	1.10	161.7	-.58	.065
0.0	-.33	.44	-11.1	1.11	163.6	-.21	.061
0.0	-.50	.25	-7.6	1.10	160.2	.29	.063
0.0	-.67	.25	-5.9	1.07	155.0	.53	.064
0.0	-.83	.30	-4.3	1.04	150.9	.77	.057
0.0	-1.00	.30	-2.6	1.03	148.5	.92	.044
0.0	-1.17	.30	-1.5	1.02	147.4	1.12	.033
0.0	-1.33	.25	-.91	1.02	147.1	1.17	.020
0.0	-1.50	.15	-.81	1.01	147.1	1.16	.012
-.33	0.0	-10.2	-2.4	1.08	158.8	-2.43	.062
-.17	0.0	-5.5	-3.3	1.03	150.2	-2.11	.065

TABLE B-3 (Continued)

X/R	Y/R	Flow Pitch (DEG)	Flow Yaw (DEG)	U_z/U_E	V_{Total} (fps)	$P_{st}-P_{st\infty}$ (psf)	$\sqrt{\overline{u'^2}}/U_E$
0.0	0.0	1.2	-3.7	1.00	144.7	-.98	.066
.17	0.0	8.0	-3.4	1.03	151.1	-.55	.065
.33	0.0	11.1	-2.8	1.08	159.6	-.54	.061
.50	0.0	9.5	-2.3	1.10	161.3	.23	.062
.67	0.0	7.3	-2.0	1.10	161.1	.28	.064
.83	0.0	5.4	-1.8	1.09	158.9	.29	.065
1.00	0.0	4.0	-1.7	1.07	155.7	.38	.061
1.17	0.0	2.5	-1.5	1.05	151.8	.30	.047
1.33	0.0	.94	-1.2	1.03	148.9	.84	.032
1.50	0.0	.25	-.91	1.01	146.7	.98	.018
1.67	0.0	.15	-.91	1.01	146.0	.95	.006
0.0	0.0	3.0	-2.4	1.01	144.8	-1.08	.067
-.33	0.0	-9.4	-1.7	1.08	156.9	-2.42	.062
-.50	0.0	-10.6	-1.3	1.11	162.6	-2.08	.059
-.67	0.0	-8.0	-.86	1.12	161.8	-1.17	.060
-.83	0.0	-6.2	-.86	1.10	159.6	-.68	.061
-1.00	0.0	-4.5	-.56	1.08	156.3	-.13	.054
-1.17	0.0	-3.0	-.56	1.07	153.2	.15	.054
-1.33	0.0	-1.5	-.61	1.05	150.8	.40	.042
-1.50	0.0	-.54	-.81	1.03	148.3	1.25	.027
-1.67	0.0	.10	-.86	1.02	146.7	1.31	.011
-1.83	0.0	.25	-.86	1.02	146.2	1.43	
-2.00	0.0	.25	-.96	1.01	145.7	1.46	
-1.00	2.00	.15	-1.1	1.02	145.8	1.35	.007
-.83	2.00	.25	-1.1	1.01	145.7	1.34	.009
-.67	2.00	.30	-1.1	1.01	144.8	1.31	.013
-.50	2.00	.34	-1.1	1.01	145.6	1.34	.017

TABLE B-3 (Continued)

X/R	Y/R	Flow Pitch (DEG)	Flow Yaw (DEG)	U_z/U_E	V_{Total} (fps)	$P_{st}-P_{st\infty}$ (psf)	$\sqrt{\overline{u'^2}}/U_E$
-.33	2.00	.44	-1.1	.99	142.7	1.24	.018
-.17	2.00	.44	-1.1	.99	142.0	1.22	.018
0.0	2.00	.44	-1.1	.99	142.0	1.22	.018
.17	2.00	.44	-1.1	.99	142.6	1.24	.018
.33	2.00	.44	-1.1	1.00	143.9	1.28	.017
.50	2.00	.44	-1.1	1.01	144.7	1.31	.015
.67	2.00	.44	-1.1	1.01	145.4	1.34	.012
.83	2.00	.44	-1.1	1.02	145.8	1.35	.009
1.00	2.00	.39	-1.3	1.02	146.2	1.20	.007

S Symmetric profiles

TABLE B-4

Profiles for Q = 5.0 in H_2O, Z/D = 10, α_e = -2°

X/R	Y/R	Flow Pitch (DEG)	Flow Yaw (DEG)	U_z/U_E	V_{Total} (fps)	$P_{st}-P_{st\infty}$ (psf)	$\sqrt{\overline{u'^2}}/U_E$
-1.67	0.0	-.44	-1.2	1.02	150.0	1.40	.016
-1.50	0.0	-.89	-1.1	1.03	150.9	1.40	.076
-1.33	0.0	-1.9	-.96	1.04	153.0	.58	.039
-1.17	0.0	-2.8	-.96	1.05	155.2	.37	.047
-1.00	0.0	-4.1	-1.0	1.08	158.9	.05	.054
-.83	0.0	-5.1	-1.6	1.10	162.4	-.23	.058
-.67	0.0	-7.0	-1.9	1.11	165.5	-.73	.060
-.50	0.0	-8.6	-2.1	1.11	165.7	-1.42	.063
-.33	0.0	-8.0	-2.2	1.08	161.1	-1.74	.066
-.17	0.0	-3.0	-1.8	1.03	152.1	-1.34	.067
0.0	0.0	3.7	-1.1	1.01	149.6	-.81	.069
.17	0.0	9.7	-.36	1.05	157.0	-.34	.071
.33	0.0	11.8	-.36	1.09	164.2	-.25	.066
.50	0.0	9.9	-.61	1.09	164.3	.54	.063
.67	0.0	7.7	-.86	1.08	161.2	.77	.063
.83	0.0	5.9	-1.2	1.07	159.3	.74	.061
1.00	0.0	4.0	-1.5	1.06	158.0	.71	.056
1.17	0.0	2.2	-1.6	1.05	155.5	.69	.044
1.33	0.0	.64	-1.5	1.03	152.6	1.14	.029
1.50	0.0	.20	-1.5	1.02	151.0	1.20	.015
1.67	0.0	.10	-1.4	1.02	150.7	1.24	.008
0.0	.33	4.0	7.5	1.09	163.0	.64	.063
0.0	.50	3.0	6.5	1.12	166.9	1.04	.060
0.0	.67	2.5	4.7	1.12	166.2	1.08	.060
0.0	.83	2.2	3.4	1.11	157.8	1.03	.061

TABLE B-4 (Continued)

X/R	Y/R	Flow Pitch (DEG)	Flow Yaw (DEG)	U_z/U_E	V_{Total} (fps)	$P_{st}-P_{st\infty}$ (psf)	$\sqrt{\overline{u'^2}}/U_E$
0.0	1.0	1.7	2.0	1.08	153.9	1.12	.059
0.0	0.0	4.1	-1.6	1.02	146.3	-.92	.069
0.0	-.17	3.4	-8.7	1.05	152.1	-.95	.068
0.0	-.33	2.3	-13.9	1.09	160.3	-.76	.063
0.0	-.50	1.4	-12.7	1.11	162.2	-.09	.060
0.0	-.67	.84	-9.2	1.11	160.9	.29	.060
0.0	-.83	.64	-7.5	1.10	158.3	.60	.062
0.0	-1.0	.49	-6.1	1.07	154.2	.80	.059
0.0	-1.17	.34	-4.7	1.06	151.5	1.01	.053
0.0	-1.33	.30	-3.3	1.05	149.9	1.14	.042
0.0	-1.50	.25	-2.2	1.04	148.5	1.26	.030
0.0	-1.67	.25	-1.6	1.03	146.9	1.38	.017
0.0	-1.83	.30	-1.2	1.02	146.0	1.39	.008
0.0	-2.0	.25	-1.2	1.02	146.0	1.42	.006
0.0	1.17	1.3	1.0	1.04	149.1	.39	.053
0.0	1.33	.94	-.16	1.01	144.7	.42	.038
0.0	1.50	.64	-1.1	.99	142.3	1.01	.028
0.0	1.67	.64	-1.5	.98	141.1	.99	.021
0.0	1.83	.59	-1.6	.99	142.7	1.49	.019
0.0	2.00	.59	-1.7	.98	142.3	1.46	.019
0.0	2.17	.54	-1.7	.98	142.3	1.46	.019
0.0	2.33	.49	-1.7	.98	142.3	1.46	.019
-1.67	2.00	0.0	-1.6	1.02	148.4	1.67	.005
-1.33	2.00	0.0	-1.6	1.02	148.3	1.62	.006
-1.17	2.00	0.0	-1.6	1.02	148.0	1.58	.008
-1.00	2.00	.10	-1.6	1.02	148.1	1.60	.012
-.83	2.00	.25	-1.5	1.01	147.6	1.59	.016

TABLE B-4 (Continued)

X/R	Y/R	Flow Pitch (DEG)	Flow Yaw (DEG)	U_z/U_E	V_{Total} (fps)	$P_{st}-P_{st\infty}$ (psf)	$\sqrt{\overline{u'^2}}/U_E$
-.67	2.00	.34	-1.5	1.01	146.5	1.52	.019
-.50	2.00	.34	-1.6	1.00	145.2	1.50	.021
-.33	2.00	.44	-1.6	.99	143.8	1.47	.020
-.17	2.00	.59	-1.7	.99	143.7	1.48	.020
0.0	2.00	.64	-1.7	.98	142.7	1.40	.019
.17	2.00	.59	-1.7	.98	143.0	1.41	.020
.33	2.00	.49	-1.8	.99	143.8	1.40	.021
.50	2.00	.44	-1.9	.99	144.7	1.38	.021
.67	2.00	.39	-1.9	1.00	146.1	1.40	.019
.83	2.00	.30	-2.0	1.01	147.2	1.35	.015
1.0	2.00	.25	-2.0	1.02	148.3	1.38	.010
1.17	2.00	.25	-2.0	1.02	148.6	1.37	.007
1.33	2.00	.30	-1.9	1.02	148.7	1.31	.005

TABLE B-5

Profiles for Z/D = 40, $\alpha_e = 0^o$

X/R	Y/R	Flow Pitch (DEG)	Flow Yaw (DEG)	U_z/U_E	V_{Total} (fps)	$P_{st}-P_{st\infty}$ (psf)	$\sqrt{\overline{u'^2}}/U_E$
.33	0.0	.64	-.25	1.04		1.44	
.67	0.0	.69	0.0	1.03		1.42	.0232
1.00	0.0	.54	-.65	1.02		1.27	.0217
1.33	0.0	.54	-.25	1.01		1.22	.0200
1.67	0.0	.49	-.15	1.01		1.19	.0167
2.00	0.0	.39	-.10	1.00		1.09	.0143
2.33	0.0	.34	.05	1.00		1.09	.0113
2.67	0.0	.25	0.0	1.00		1.07	.0075
0.0	0.0			1.08			.0268
0.0	-.17			1.08			.0267
0.0	-.33			1.07			.0250
0.0	-.83			1.06			.0232
0.0	-1.00			1.06			.0225
0.0	-1.17			1.05			.0217
0.0	-1.33			1.05			.0208
0.0	-1.50			1.05			.0200
0.0	-1.67			1.04			.0175
0.0	-1.83			1.04			.0158
0.0	-2.00			1.04			.0153
0.0	-2.17			1.04			.0134
0.0	-2.33			1.03			.0117
0.0	-2.50			1.03			.0095
0.0	-2.83			1.03			.0073
0.0	-3.17			1.03			.0063
0.0	.17			1.05			.0275

TABLE B-5 (Continued)

X/R	Y/R	Flow Pitch (DEG)	Flow Yaw (DEG)	U_z/U_E	V_{Total} (fps)	$P_{st}-P_{st\infty}$ (psf)	$\sqrt{\overline{u'^2}}/U_E$
0.0	.33			1.05			.0267
0.0	.50			1.05			.0258
0.0	.67			1.04			.0242
0.0	.83			1.04			.0233
0.0	1.00			1.04			.0225
0.0	1.17			1.03			.0225
0.0	1.33			1.03			.0225
0.0	1.50			1.02			.0225
0.0	1.67			1.02			.0225
0.0	1.83			1.01			.0208
0.0	2.00			1.00			.0183
0.0	2.17			1.00			.0167
0.0	2.33			1.00			.0157
.17	0.0			1.04			.0258
0.0	2.33			1.00			.0157
.17	2.33			1.00			.0158
.33	2.33			1.00			.0153
.50	2.33			1.00			.0153
.67	2.33			1.00			.0150
.83	2.33			1.00			.0143
1.00	2.33			1.00			.0135
1.17	2.33			1.01			.0125
1.33	2.33			1.01			.0112
1.50	2.33			1.01			.0098
1.67	2.33			1.01			.0087
1.83	2.33			1.01			.0077

TABLE B-5 (Continued)

X/R	Y/R	Flow Pitch (DEG)	Flow Yaw (DEG)	U_z/U_E	V_{Total} (fps)	$P_{st}-P_{st\infty}$ (psf)	$\sqrt{\overline{u'^2}}/U_E$
2.00	2.33			1.01			.0065
2.17	2.33			1.01			.0060
2.50	2.33			1.01			.0057

TABLE B-6

Profiles for Z/D = 40, $\alpha_e = -2^0$

X/R	Y/R	Flow Pitch (DEG)	Flow Yaw (DEG)	U_z/U_E	V_{Total} (fps)	$P_{st}-P_{st\infty}$ (psf)	$\sqrt{\overline{u'^2}}/U_E$
3.0	0.0			.99			.0063
2.67	0.0			.99			.0090
2.33	0.0			.99			.0093
2.00	0.0			.99			.0130
1.67	0.0			.99			.0165
1.33	0.0			1.00			.0183
1.00	0.0			1.00			.0200
.67	0.0			1.00			.0200
.33	0.0			1.00			.0200
0.0	0.0			1.00			.0200
0.0	-.17			1.06			.0192
0.0	-.33			1.05			.0192
0.0	-.67			1.03			.0183
0.0	-1.00			1.02			.0167
0.0	-1.33			1.02			.0143
0.0	-1.67			1.01			.0122
0.0	-2.33			1.00			.0063
0.0	-2.67			1.00			.0057
0.0	-3.00						
0.0	.33			1.02			.0225
0.0	.67			1.02			.0250
0.0	1.0			1.02			.0258
0.0	1.33			1.02			.0233
0.0	1.67			1.01			.0225
0.0	2.00			1.00			.0232

TABLE B-6 (Continued)

X/R	Y/R	Flow Pitch (DEG)	Flow Yaw (DEG)	U_z/U_E	V_{Total} (fps)	$P_{st}-P_{st\infty}$ (psf)	$\sqrt{\overline{u'^2}}/U_E$
.33	2.33			.98			.0160
.67	2.33			.98			.0140
1.00	2.33			.98			.0117
1.33	2.33			.99			.0088
1.67	2.33			.99			.0075
2.00	2.33			.99			.0063
2.33	2.33			.99			.0057
2.67	2.33						
3.00	2.33						